# Studies on $CO_2$ sorption behavior and structural flexibilities of various metal-organic frameworks

Sung-min Hyun

Division of Chemistry

Graduate school of UNIST

# Studies on $CO_2$ sorption behavior and structural flexibilities of various metal-organic frameworks

A thesis

submitted to the Graduate School of UNIST

in partial fulfillment of the

requirements for the degree of

Master of Science

Sung-min Hyun

Month/Day/2014

Approved by

_____

Major Advisor

Hoi Ri Moon

# Studies on $CO_2$ sorption behavior and structural flexibilities of various metal-organic frameworks

Sung-min Hyun

This certifies that the thesis of Sung-min Hyun is approved.

Month/Day/2014

Thesis Supervisor: Hoi Ri Moon

Myoung Soo Lah

Wonyoung Choe

**Abstract**

A metal-organic framework (MOF), {[($NiL_{propyl}$)$_2$(BPTC)]·4DMF·2$H_2O$} (**1-as**) ([$NiL_{propyl}$]($ClO_4$)$_2$ = [Ni($C_{14}H_{34}N_6$)]($ClO_4$)$_2$, $H_4$BPTC = 2,2',5,5'–biphenyltetracarboxylic acid, and DMF = *N*,*N*-dimethylformamide) was synthesized via self-assembly of [$NiL_{propyl}$]($ClO_4$)$_2$ and $H_4$BPTC in DMF/$H_2O$ mixture solution. Single crystal X-ray diffraction data revealed that **1-as** has a three-dimensional (3D) structure with accessible pore occupied by guest molecules. Due to its flexibility, the structure of **1-as** was changed into **1** with shrunk and closed pores upon elimination of guest molecules. Gas sorption experiments with $N_2$ and $H_2$ confirmed that **1** has a closed pore structure as evidenced by those small adsorption amounts. However, $CO_2$ isotherm at 195 K appeared in two-step adsorption with significantly large uptake amount, indicating that $CO_2$ gas triggered a structural transformation of **1** into open and expanded porous structure. Interestingly, the structural transition of **1** upon $CO_2$ uptake at 195 K was occurred in two distinct steps, gate-opening and breathing, independently and it was confirmed by *in-situ* X-ray powder diffraction (XRPD) experiment and gas sorption isotherms. Gate-opening happened through rotation of Ni (II) macrocycles with breaking and reconstruction of hydrogen bonds between secondary amines on macrocycles and carboxylates. This brought about the abrupt increase in $CO_2$ adsorption without significant changes on XRPD patterns. On the other hand, breathing resulted from the rotation of single bonds in $BPTC^{4-}$ ligands with gradual increase of $CO_2$ adsorption amount and with drastic changes on XRPD patterns.

In addition, two 2D MOFs, {[($NiL_{allyl}$)$_2$(BuTC)]·2DEF·2$H_2O$} (**2-as**) and {[($NiL_{allyl}$)$_2$(BuTC)]·3$H_2O$} (**3-as**), ([$NiL_{allyl}$]($ClO_4$)$_2$ = [Ni($C_{14}H_{30}N_6$)]($ClO_4$)$_2$, $H_4$BuTC = 1,2,3,4–butanetetracarboxylic acid, DEF = *N*,*N*-diethylformamide) were obtained from the reaction between [$NiL_{allyl}$]($ClO_4$)$_2$ and $H_4$BuTC in DEF/$H_2O$ and MeCN/$H_2O$, respectively (MeCN = acetonitrile). It was revealed by single crystal X-ray diffraction and XRPD results that **2-as** and **3-as** have 2D layered structures, the layers were stacked infinitely with intercalated guest molecules in between the layers. Since the same building blocks were used to construct both MOFs, the structure of each layer was identical. However, layer packing and the layer-layer distances were different for each MOF depending on the size and the nature of guest molecules. Interestingly, these guest molecules could be easily liberated from the host due to the instability of DEF guest molecules intercalated in **2-as**, resulting in dried compound **2**, whose XRPD pattern was same as **3-as** with slightly different relative intensities. On the other hand, dried compounds of **3-as** (**3**) had the same XRPD pattern of **3-as**. The similar but non-identical XRPD patterns suggested that the dried structure **2** had the same interlayer distance and the same intra-layer structure as **3-as** and **3**, whereas its layer stacking manner remained the same as that of **2-as**. This subtle structural difference of **2** and **3** caused the difference in the reversibility of structural transformation and in $CO_2$ uptake behaviors at 195 K.

Lastly, {[($NiL_{amine}$)$_2$($BPDC$)$_2$]·6$H_2O$} (**4-as**) and {[($NiL_{propyl}$)$_2$($BPDC$)$_2$]·5$H_2O$} (**5-as**) were synthesized via self-assembly of $H_2BPDC$ with [$NiL_{amine}$]($ClO_4$)$_2$ in DEF/MeCN/$H_2O$ mixture solution and with [$NiL_{propyl}$]($ClO_4$)$_2$ in MeCN/$H_2O$ mixture solution, respectively ([$NiL_{amine}$]($ClO_4$)$_2$ = [Ni($C_{12}H_{32}N_8$)]($ClO_4$)$_2$, 4,4-biphenyldicarboxylic acid). Single crystal X-ray diffraction and XRPD results revealed that **2-as** and **3-as** have identical structure. The infinite coordination between $BPDC^{2-}$ and Ni (II) macrocycles yielded the 1D chains and they are extended in three different directions to construct a double network of threefold braids. The three-directional packing generates honeycomb-like 1D channels occupied by pendant groups with different terminal functional groups of Ni (II) macrocycles and the guest water molecules. After removing guest water molecules, the activated compounds **4** and **5** were obtained, respectively. Due to difference in functional groups, which are exposed to pore surface, both structures showed different $CO_2$ sorption behavior. The framework **4** indicated chemisorption behaviors but **5** only showed physisorption characteristics. It was confirmed through gas sorption isotherms and TGA cycling.

# Contents

**List of figures**

**List of tables**

**Nomenclatures**

| | |
|---|---|
| **MOF** | Metal-organic framework |
| **SBU** | Secondary building unit |
| **XRPD** | X-ray powder diffraction |
| **IR** | Infrared |
| **TGA** | Thermogravimetric analysis |
| **EA** | Elemental analysis |
| **BET** | Brunauer-Emmett-Teller |
| **SEM** | Scanning electron microscope |
| **$P_2O_5$** | Phosphorus pentoxide |
| **DMF** | *N*,*N*-dimethylformamide |
| **DEF** | *N*,*N*-diethylformamide |
| **MeCN** | Acetonitrile |
| **EthOH** | Ethanol |
| **$H_4$BPTC** | 2,2',5,5'–biphenyltetracarboxylic acid |
| **$H_4$BuTC** | 1,2,3,4–butanetetracarboxylic acid |
| **$H_2$BPDC** | 4,4-biphenyldicarboxylic acid |

## I. Introduction

Metal-organic frameworks (MOFs) are well-ordered crystalline solids, constructed by the reaction between metal building blocks and coordinating organic linkers. They have attracted much attention in various fields such as gas storage,[1-2] catalysis,[3] molecular separation,[4] and sensing.[5] The widespread interest in MOFs arises from a wide range of choice of both metal building block and organic linker, which provide two important features for construction of MOFs: (1) determining the geometric structures of MOFs (2) adding the flexibility or functionality of the framework. Because the structure of MOF is the decisive factor in their functionalities, various researches have been made in development of new MOF architectures via adopting a wide range of metals and ligands.

Recently, flexible, or soft and dynamic MOFs have attracted much attention because they have shown and dynamic structural transformation upon external stimuli, such as light,[6-7] temperature,[8] and amount of and kinds of guest molecules.[9-10] These gives distinctive properties which are not appeared on rigid MOFs, such as gate-opening phenomenon through guest-host interaction, stepwise guest uptake and selective gas adsorption.[8-11] These flexibility of MOFs result from the change of interlayer distance in two-dimensional (2D) layered structure,[9] interpenetrated structure,[12] or rotation of bonds in frameworks.[13]

In addition, the research field gaining large interests in MOFs is the capture of $CO_2$ gas due to their excellent potentials for large capacity, such as 60.8 wt% at 298 K and 50 bar in MOF-177, 56.9 wt% at 304 K and 50 bar in MIL-101(Cr), and 42.8 wt% at 313 K and 40 bar Cu-BTTri.[14-16] Furthermore, a high structural tunability and a relatively easy functionalization give several strategies for increasing selectivity of $CO_2$ over other gases like $N_2$. One of the strategies relies on enhancing the interaction between frameworks and $CO_2$ gas molecules through functionalization with amine groups.[17] The other method utilizes physical properties of $CO_2$ to improve selectivity without increasing affinity of MOFs for $CO_2$. The kinetic diameter of $CO_2$ is 3.30 Å, which is smaller than others except $H_2$ ($O_2$, 3.46 Å; $N_2$, 3.64 Å; $H_2$, 2.89 Å), and it has higher quadrupole moment ($1.4 \times 10^{-39}$ C $m^2$) and polarizability (2.51 $Å^3$), which makes $CO_2$ to interact with MOFs better. Therefore, the separation of $CO_2$ from other gas can be achieved through effectively controlling the pore size. Another way is incorporating flexible frameworks whose structures have the "open-pore" structure only for $CO_2$ through selective structural transformation, or "gate-opening" process, otherwise keeps pore closed.

## I.1. Flexible metal-organic frameworks

MOFs are classified in the three categories, 1st, 2nd, and 3rd generation.[14] 1st generation MOFs possess their porosity only with guest molecules, collapsing irreversibly on guest removal. 2nd generation has rigid and robust structure during activation, showing permanent porosity. In addition, flexible and dynamic MOF is the 3rd generation of MOF, responding to external stimuli. Based on the researches on 1st generation MOFs, studies of 2nd generation frameworks have been actively done on their structure, and various properties, and have attracted much attention due to their vast potential for applications like previously mentioned. Since the properties of MOFs for practical applications are greatly influenced by their structures,[6,11] many researchers have devoted to the design of new architectures for MOFs.

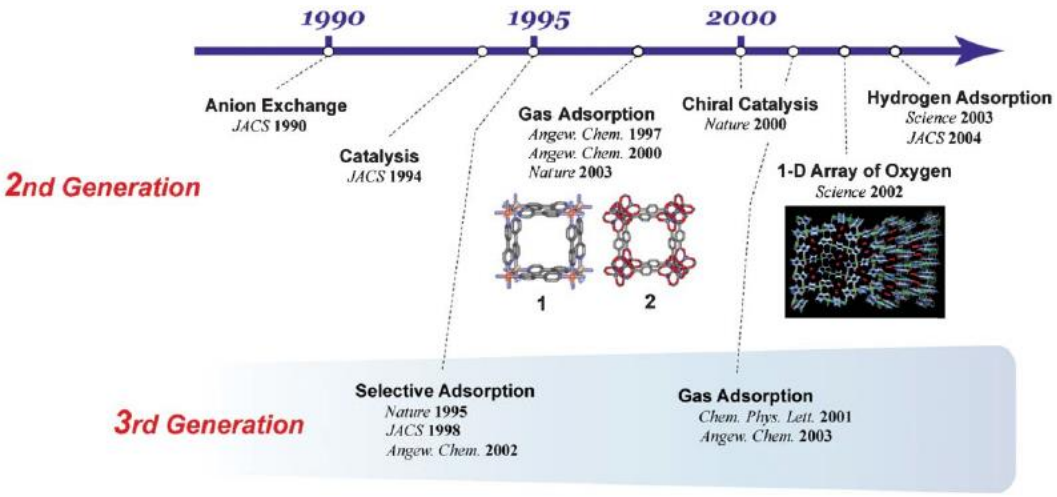


**Figure 1.1.** Historical views of developments of MOFs.

For the 3rd generation of MOFs, soft or flexible MOFs have been researched for discovering their distinctive properties represented through structural change upon various external stimuli. For example, $[Zn_2(adb)_2(dabco)]$ (adb = 9,10-anthracene dibenzoate, dabco = 1,4-diazabicyclo[2,2,2] octane) showed translation from kinetic phase to thermodynamic phase as guest molecules were removed.[15] $[Zn_2(bdc)_2(dabco)]$ containing functional guest molecules caused closing and opening the pore upon desolvation and resolvation or upon the light-induced conformation change of guest.[6, 11]

Such many types of MOFs suggested many kinds of structural changes, and those transformations of MOFs could result from (i) the bond breakage/reconstruction, (ii) the rotation or reorientation of bonds and (iii) mechanical displacement of frameworks, such as sliding of 2D layers or interpenetrated 3D frameworks.[12, 16] The first cases are not common in flexible MOFs because it is too

harsh conditions that MOFs endure such chemical changes. Thus, second and third types of structural changes have been usually observed for flexible MOFs. Among them, two types of behaviors caused by rotation or reorientation of bonds, "breathing" and "gate-opening", are widely known and have been researched intensively since Ferey's group and Kitagawa's groups emphasized the importance of each phenomenon. Apart from those defined structural dynamics, there are many MOFs possessing flexible behaviors, such as sliding of interpenetrated 3D structures,[12, 16-17] expanding and shrinkage of 2D layers or 3D pillared layers,[9,18] and etc. The most representative examples for breathing MOFs are MIL-53 series and MIL-88 series, which have been studied for finding the cause of flexibility since 2002 by Ferey's group.[19] MOFs having gate-opening properties have been researched for developing various structures which can possess gate-opening phenomenon, and for studying kinetics of structural transformation since 2003.[14,20]

However, studies have usually not focused on finding guest-interactive sites due to the thermal disorders of guest molecules although its importance. In addition, the structural understandings are still insufficient for various types of flexible MOFs. Thus, the research for distinctive structural dynamics to find the guest-host interaction, factors giving flexibility and distinctive properties are required to design flexible MOFs with various functional groups.

### I.1.1. Breathing

Breathing phenomenon is a stimulus-generated-reversible transformation between two states corresponding to expansion and contraction, respectively.[19] They showed the expansion and contraction through movement of atoms in several Å with retaining the same or similar topologies upon external stimuli. The most famous example for breathing MOFs are several kinds of MIL series, developed and studied by Ferey's group. The first MOF possessing breathing properties, MIL-53 (Cr), showed the structural changes upon temperature change and upon hydration and dehydration.[21-22] After that, many studies about breathing MOFs including MIL-53 series have been done, and therefore various breathing MOFs were built by researchers. However, many researchers have usually focused only on the first and final state of frameworks and the distinctive properties, which they showed, without figuring out the cause of changes. Thus, various structural factors to have or to affect breathing behavior, such as kinds of metals, secondary building units (SBUs), and topology, were figured out by Ferey's group in 2009 through a wide range of researches.[19] Afterward, other groups developed and studied breathing MOFs and found additional causes or factors that make possible to control the breathing behavior, such as functional groups of ligands,[23] and rotation and bending of bonds.[10]

Breathing of MOFs usually comes from the distortion of coordination environment of metal building blocks. Therefore, it is obvious that MOFs should possess two sites with different properties, rigid one for retaining the whole connectivity and weak one for leading to flexible behaviors. That weak point of coordination bonds act as "knee cap" site giving breathing motion. MIL-53 (Cr), the most famous breathing MOFs, has a "knee cap" position at coordination between carboxylate groups and metal ions either. MIL-53 (Cr) is famous for breathing various external stimuli, for example, temperature changes, hydration/dehydration, and $CO_2$ adsorption/desorption.[21-22]

The structure of as-synthesized MIL-53 (Cr) (MIL-53 (Cr) AS) is 3D framework built with 1D metal SBUs of $Cr^{3+}$ octahedra bridged by one $bdc^{2-}$ and one $OH^-$. $bdc^{2-}$ connects each metal SBU forming orthorhombic structure with *Pnam* space group in $4^4$ net topology. MIL-53 (Cr) AS possesses 1D channel along the *c*-axis and free $H_2bdc$ molecules are filling the 1D channel as guest molecules. To activate MIL-53 (Cr) AS, the calcination of free $H_2bdc$ was performed via heating MIL-53 (Cr) AS at 300 $^oC$ and it generated slightly expanded structure, MIL-53 (Cr) HT. Upon the cooling MIL-53 (Cr) HT, the hydration was simultaneously occurred in the air condition and interestingly the uptake of water caused the contraction of cell, instead of expanding, and the crystal system was changed to monoclinic, *C*2/*c* space group. The structural transition was attributed to hydrogen bond formation between OH- on $Cr^{3+}$ SBUs and water molecules, and the framework didn't uptake additional guest molecules.

The similar structural change was observed when the activated sample, MIL-53 (Cr) HT, adsorbed 2 bar of $CO_2$ gas at 298 K.[21] The cell was shrunk by weak quadrupole interaction between $OH^-$ groups and $CO_2$ gas molecules either, resulting in MIL-53 (Cr) LP. However, unlike adsorption of water MIL-53 (Cr) LP adsorbed additional $CO_2$ molecules leading to the structure of MIL-53 (Cr) HP via breathing upon gas uptake. In addition, the structural transition during $CO_2$ uptake gave rise to inflection point on the gas sorption isotherms at about 6 bar.

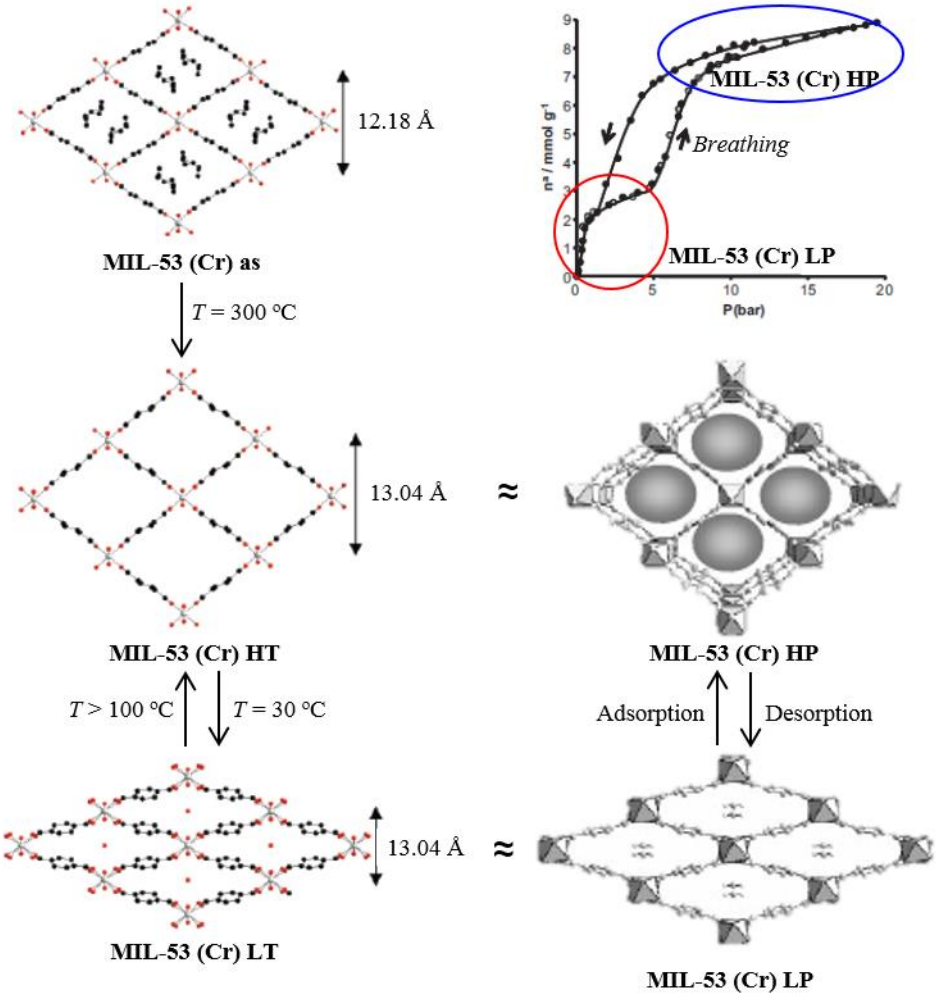


**Figure 1.2.** Schematic representation of structural transformation of MIL-53 (Cr).

As previously stated, the origin of breathing behaviors of MIL-53 (Cr) is on the coordination bonds between $Cr^{3+}$ and oxygen atoms of carboxylate groups. Due to less directional geometry of $Cr^{3+}$ octahedra and the free rotation of C-C bonds between the carboxylate and phenyl ring of $bdc^{2-}$, the distortion of bonds during structural changes get less resistance and therefore large breathing can occurred for MIL-53 (Cr).

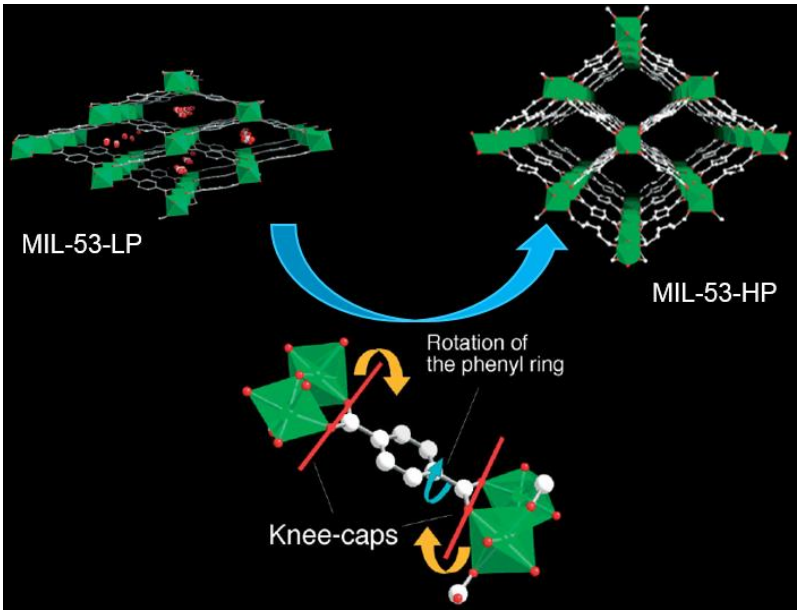


**Figure 1.3.** The origin of structural transformation of MIL-53 upon $CO_2$ uptake.

In addition to possession of weak point on the framework, the existence of free space for atomic displacement during structure transformation affects to the flexible behaviors of structure, either.[19, 23] To change the free space, the modification of functional groups on organic groups is the appropriate method, and it was researched in 2012 by Fischer's group.[23] They functionalized $bdc^{2-}$ with various types of flexible substituents were used to synthesize breathing MOFs, $[Zn_2(fu\text{-}bdc)_2(dabco)]$ ($(fu\text{-}bdc)^{2-}$ = terephtalate with functional groups), via solvothermal method.

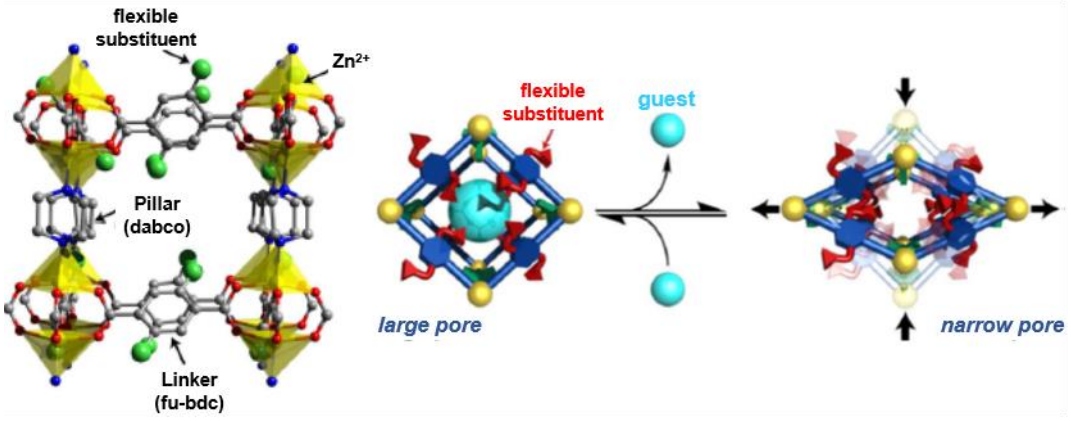


**Figure 1.4.** Schematic view of structure of $[Zn_2(fu\text{-}bdc)_2(dabco)]$ and its structural transition.

The reaction with $Zn^{2+}$ precursors and $(fu\text{-}bdc)^{2-}$ generated the 2D layer of zinc paddle wheels linked by $fu\text{-}bdc^{2-}$ ligands, and the layers are connected by dabco pillars on the axial positions of paddle wheel, yielding isoreticular 3D structures, $[Zn_2(fu\text{-}bdc)_2(dabco)]$. The distortion of paddle wheel caused the breathing effect upon guest inclusion and exclusion like Figure 1.4, and these breathing behaviors varied according to functional groups. The diverse types of organic linkers used for synthesis are represented in Figure 1.5 (a).

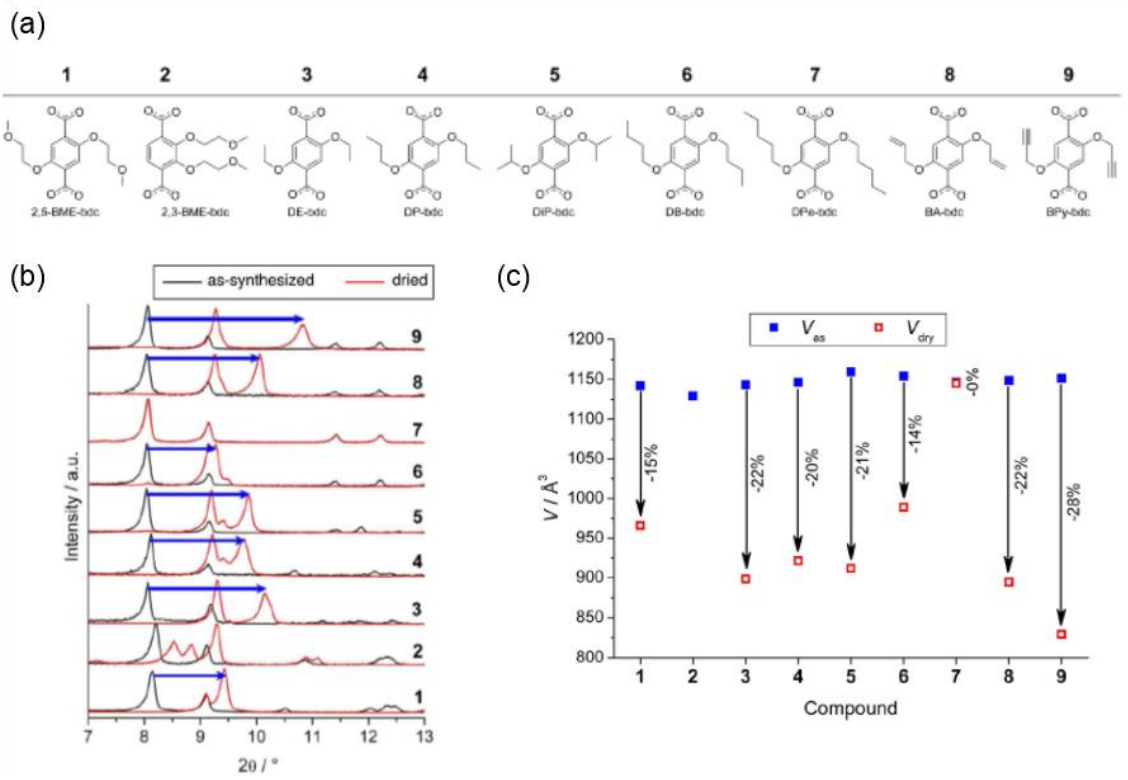


**Figure 1.5.** Library of fu-bdc used in preparation of $[Zn_2(fu\text{-}bdc)_2(dabco)]$, Changes in (b) XRPD patterns and (c) the specific volume ($V$, $V=V_{cell}/Z$) of $[Zn_2(fu\text{-}bdc)_2(dabco)]$ during activation.

The impact of functional groups were observed by measuring XRPD patterns and by comparing the specific volume before and after desolvation. (Figure 1.5) Comparing $[Zn_2(fu\text{-}bdc)_2(dabco)]$ with fu-bdc of 3, 6, and 7, or as the length of chain became longer, the amount of contraction in $V$ became smaller. This is because bulky functional groups prohibit the deformation of pore structure due to lack of the free space for atomic movement. In addition, the degree of flexibility of functional groups was reduced either, resulting in the increase of specific volume change ($fu\text{-}bdc^{2-}$ : 4, 5, 8, and 9). Moreover, the position of functional groups played an important role for controlling the breathing behaviors due to change of void space, comparing $[Zn_2(fu\text{-}bdc)_2(dabco)]$ with 1 and 2 of $fu\text{-}bdc^{2-}$.

Furthermore, Long's group showed anther examples for the effect of functional groups to breathing behavior, and the new type of ligand causing structural change in 2010.[10] They designed the breathing MOF by developing azolate based of bridging ligand, 1,4-benzenedi(1H-1,2,3-triazole) ($H_2$BDTri), that can give flexible points to the framework. The solvothermal synthesis of copper ions and $H_2$BDTri in DMF or DEF solvent resulted in flexible MOFs whose formula is Cu(BDTri)L (L=DMF or DEF). Both Cu(BDTri)(DMF) and Cu(BDTri)(DEF) are crystallized into orthorhombic system with *Imma* space group. $Cu^{2+}$, possessing octahedral geometry, is coordinated with four nitrogen atoms from four different $BDTri^{2-}$ and forms 1D metal secondary building unit, bridged by $BDTri^{2-}$ ligand. Then, the framework has the 1D channels along the *b*-axis directions. In addition, remaining coordination sites of $Cu^{2+}$ are occupied by oxygens from two guest molecules exposed to the 1D channel, DMF and DEF, respectively. Those coordinated guest molecules act not only as pillar sustaining the 1D channel during structure transition but as the functional groups for modifying their gas sorption properties. The whole structures are same for both DMF and DEF pillar except that the cell volume of Cu(BDTri)(DEF) is smaller than Cu(BDTri)(DMF).

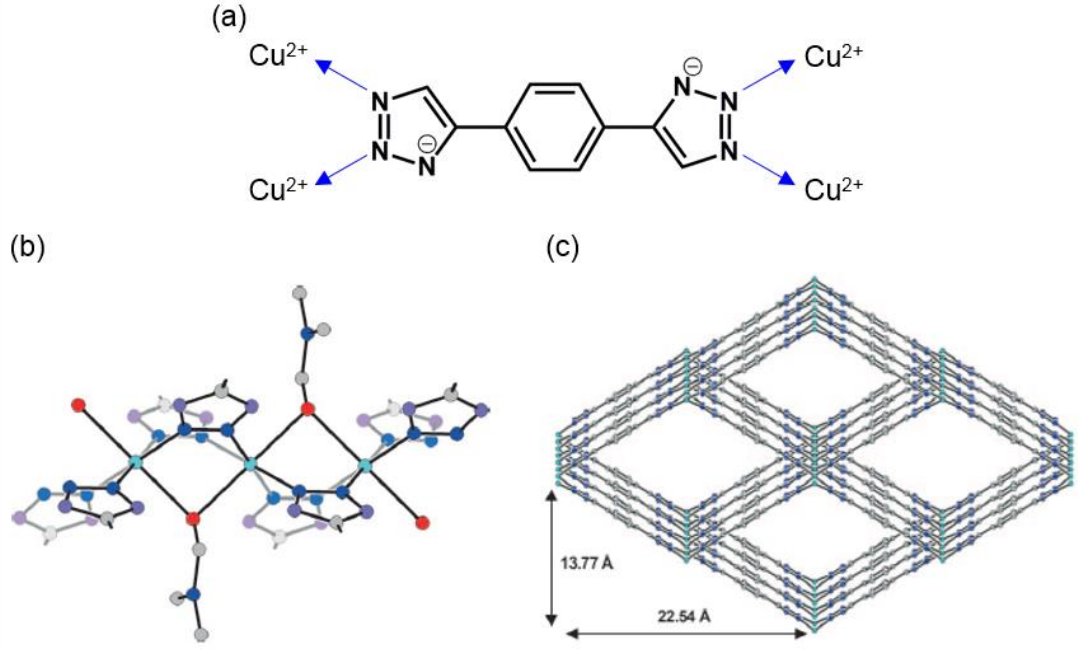


**Figure 1.6.** Structure of Cu(BDTri)(DMF) (a) Azolate based ligand, $H_2$BDTri. (b) Coordination environment around $Cu^{2+}$ (Cu, light blue; O, red; N, blue; C, gray; purple spheres represent N or C of triazolate ring) (c) View on the crystals structure of Cu(BDTri)(DMF), coordinated guest molecules were omitted for clarity).

When crystals Cu(BDTri)(DMF) were exposed to ambient atmosphere, the structure started to contract with losing guest molecules in the channel. During the structural change, the whole connectivity and crystal system were kept in same, but the cell volume was decreased about 28% from 2186.5(2) to 1567.1(4) $Å^3$ retaining permanent porosities. The cause of breathing for Cu(BDTri)(DMF) was different from other breathing MOFs like MIL series and it was very unusual. The bending of $sp^2$ carbons of azolate ring gave rise to the contraction of framework with increasing the angle α and β in Figure 1.7, which were almost 0° originally, became 8.491(2)° and 20.2(2)°, respectively.

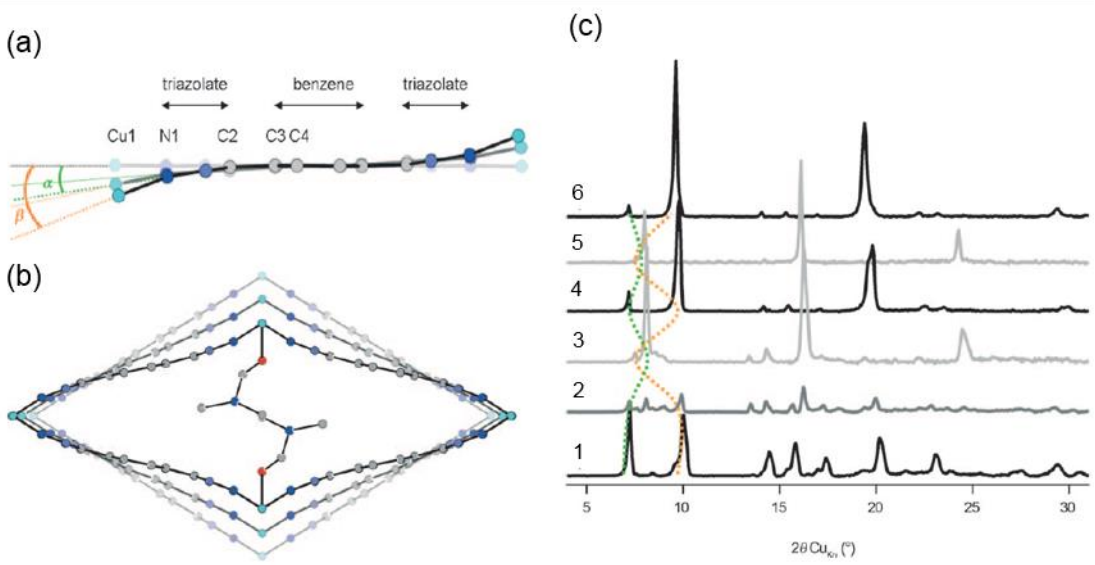


**Figure 1.7.** Structure transformation upon guest uptake and release. (a) An edge-on view of $BDTri^{2-}$ (b) View of the structural transition upon desolvation of Cu(BDTri)(DMF) (Cu, light blue; O, red; N, dark blue; C, gray; blue spheres represent N or C of triazolate ring).

To test the reversibility of structural transformation, they measured XRPD patterns of Cu(BDTri)(DMF) with adding water or methanol and exposing it to the air again to activated structure (Figure 1.7 (c)). Then, it showed reversible change with adsorbing and releasing guests just like human inhaling/exhaling the air. Moreover, the breathing occurred during the gas uptake for $N_2$ and $O_2$ thus stepwise adsorption isotherms were obtained but the degree of breathing was different relying on the kinds of gas molecules. Comparing the amount of gas after 2$^{nd}$ step, the volume of framework containing $O_2$ (17.8 mL) was much larger than $N_2$ (0.357 mL). It was possible that $O_2$ can interact with framework better and promote the larger change of framework because $O_2$ has the larger molecular weight than $N_2$ and the paramagnetism. Thus, high selectivity of $O_2$ over $N_2$ (9.4:1) with large capacity was obtained and it can be enhanced by changing the functional groups of pillar.

Additionally, changing the pillar from DMF to DEF, that is pore was exposed with different functional groups, only $O_2$ isotherm indicated the stepwise adsorption because the bulky ethyl chains interact harder with $N_2$ and the smaller pore prohibit the enough uptake of $N_2$ for structural change. Therefore, the selectivity of $O_2$ over $N_2$ increased to 13.5:1, still with large uptake of $O_2$.

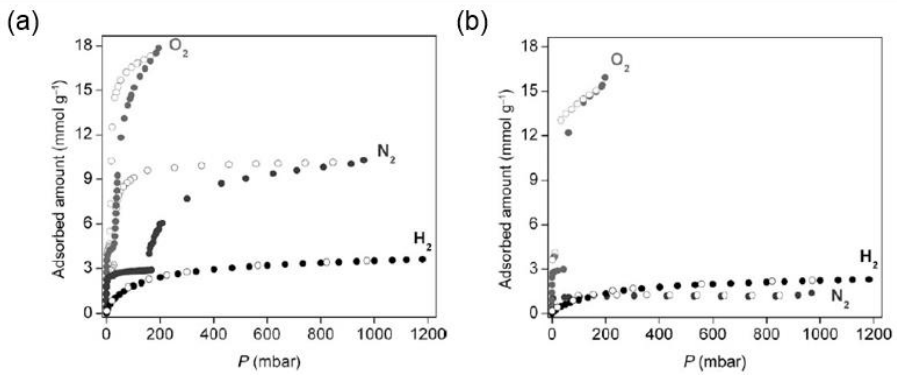


**Figure 1.8.** Gas adsorption isotherms of (a) Cu(BDTri)(DMF) and (b) Cu(BDTri)(DEF).

Apart from the structural studies for breathing MOFs, other researches for finding their potential applications were done. Kitagawa's group studied the jungle-gym type of MOF, $[Zn_2(bdc)_2(dabco)]$, via incorporating photo-responsive or luminescent guest into the pore of the MOF for controlling the adsorption properties or sensing the gas molecules, respectively.[6, 11] The structure of $[Zn_2(bdc)_2(dabco)]$ was formed with 2D square grid of zinc paddle wheel connected by $bdc^{2-}$ and dabco pillars on the axial sites of zinc clusters. When it was activated, the deformation occurred on zinc paddle wheels, resulting contraction of the cell volume. To add photo-responsive properties to breathing behaviors of $[Zn_2(bdc)_2(dabco)]$, the *trans*-azobenzene (AB) molecules, which perform *cis*/*trans* isomerization upon UV irradiation, were included in their pore, resulting in the MOF-guest composite, $[Zn_2(bdc)_2(dabco)]\supset$AB.[6] The inclusion of *trans*-AB into $[Zn_2(bdc)_2(dabco)]$ caused the contraction of cell, same as the activation, due to the conformation of AB. In addition, the composite didn't adsorb $N_2$ because AB occupied the void space of frameworks. However, when the irradiation of UV light was applied to the framework, AB changed its geometry to *cis* form, resulting in the expansion of cell to as-synthesized structure, and therefore $N_2$ can be adsorbed resulting in co-adsorption state. For the reverse transformation, heating $[Zn_2(bdc)_2(dabco)]\supset$AB generated the contracted framework containing *trans*-AB. Thus, the adsorption properties of $[Zn_2(bdc)_2(dabco)]\supset$ AB could be controlled in reversible ways via irradiation and heating.

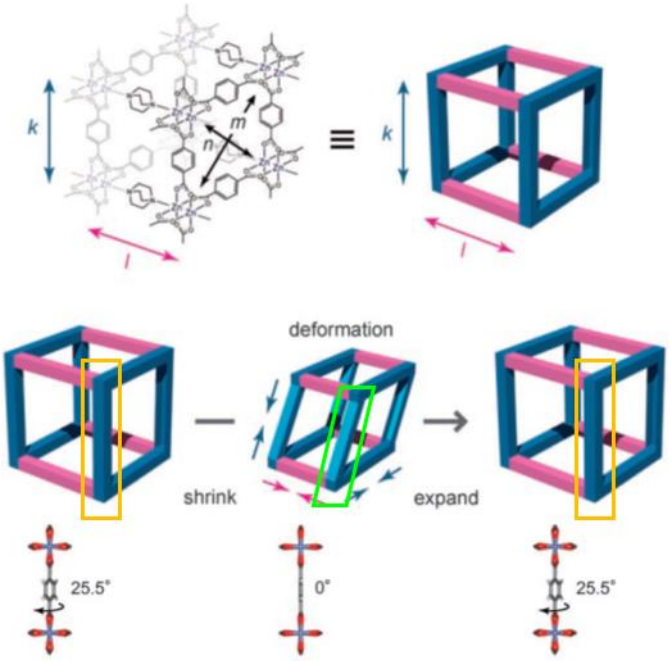


**Figure 1.9.** Schematic image of structure of $[Zn_2(bdc)_2(dabco)]$ and the structural cause of breathing behavior of framework.

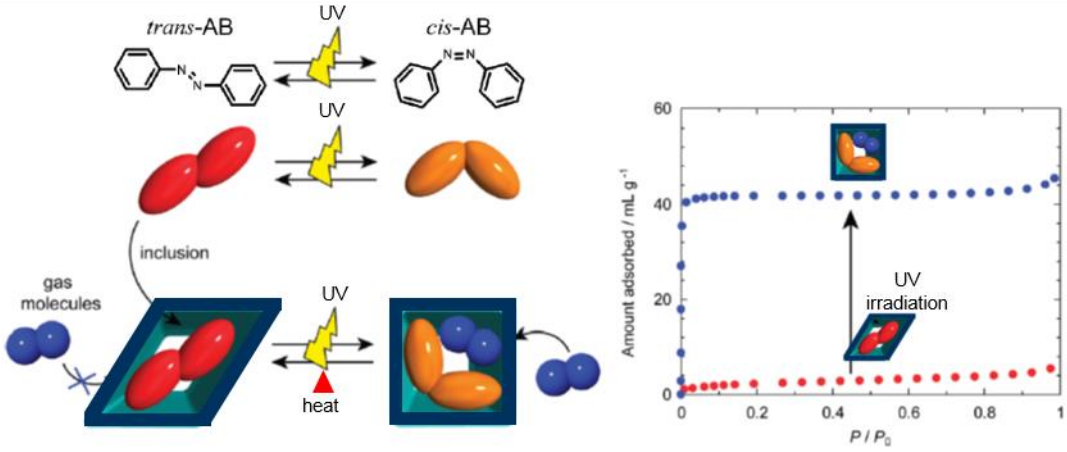


**Figure. 1.10.** Schematic representation of light-responsive and guest-induced breathing of $[Zn_2(bdc)_2(dabco)]\supset$AB and the change in its gas sorption behavior ($N_2$, at 77K) before and after irradiating UV light.

Similarly, if the guest molecules that can read out the structural transformation were occupied into the pore the breathing MOF could be used as a sensor for a specific gas, for example $CO_2$. Distyrylbenezene (DSB) having the conformation-dependent-fluorescence property was incorporated to generate a $CO_2$-sensor-MOF.[11] When $[Zn_2(bdc)_2(dabco)]$ possessed DSB molecules in their pore

([$Zn_2(bdc)_2(dabco)$]⊃DSB), it emitted a weak green fluorescence due to twisted conformation of DSB. Additionally, its structure had contracted structure just like activated [$Zn_2(bdc)_2(dabco)$], and therefore its pore volume was small enough to remain almost no space for additional guest uptake after inclusion of DSB molecules. Thus, [$Zn_2(bdc)_2(dabco)$]⊃DSB didn't adsorb $N_2$ and $O_2$, which indicated non-porous nature. However, it selectively adsorbed $CO_2$ in stepwise manner, which means that the structure transformed into microporous framework at the point B on Figure 1.11.

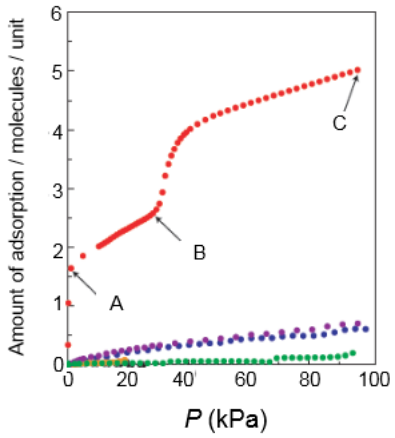


**Figure 1.11.** Gas sorption isotherms of [$Zn_2(bdc)_2(dabco)$]⊃DSB. ($CO_2$ at 195 K, red; $N_2$ at 195 K, blue; $O_2$ at 195 K, purple; $N_2$ at 77 K, green; $O_2$ at 77 K, orange; Ar at 77 K, black)

During the $CO_2$ adsorption, the structure of [$Zn_2(bdc)_2(dabco)$]⊃DSB was expanded and resulted in same framework as the as-synthesized [$Zn_2(bdc)_2(dabco)$]. Simultaneously, DSB molecules changed their conformation to planar and excited state for the increasing $CO_2$ pressure, bringing about the change of emission to a clear blue fluorescence. Furthermore, the weak green fluorescence was recovered after desorbing $CO_2$ molecules, indicating the reversibility of sensing mechanism. Thus, the breathing MOF, [$Zn_2(bdc)_2(dabco)$]⊃DSB, can be used to detect the $CO_2$ uptake through selective breathing upon $CO_2$ gas adsorption.

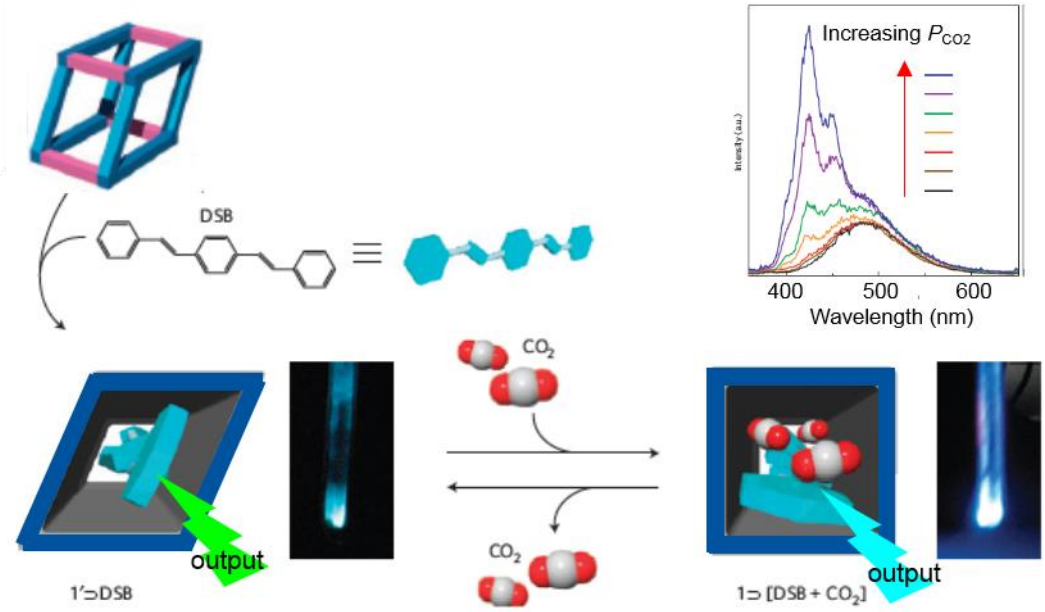


**Figure 1.12.** Schematic representation of sensing of $CO_2$ via structural change in breathing manner with the reporter molecules (DSB).

### I.1.2. Gate-opening

Gate-opening behavior is an abrupt structural transition from nonporous to porous structure upon guest uptake.[20, 24] That is, the external stimuli leading to transformation is fixed to guest uptake, and therefore the variable for gate-opening and closing is partial pressure of guest molecule. In addition, such MOFs having gate-opening property are possible to undergo various types of structural changes, such as breathing,[6, 11, 13] expansion of 3D-pillared layer structure,[9] and movement of interpenetrated structures.[17, 20] For example, the structural transition of jungle-gym-type MOF with AB or DSB, $[Zn_2(bdc)_2(dabco)]\supset$AB or $[Zn_2(bdc)_2(dabco)]\supset$DSB, which were previously mentioned, showed gate-opening properties via breathing.[6, 11] Except for these two MOFs, various flexible MOFs possess gate-opening properties via breathing.[6, 11] That's because all types of transformation could make pore close and re-open. Thus, finding the common structural causes is very hard and therefore the researches were done to find the structural moieties that can show the gate-opening phenomenon or to understand the gate-opening phenomenon itself, for example the kinetics or the mechanism of gate-opening.

Gate-opening phenomenon was discovered in 1D packing structure of Cu and bipyridine complex by Li in 2001,[25] but Kitagawa's group became aware of the importance of that, and therefore have

researched on various causes for MOFs to show gate-opening behaviors. At first, Kitagawa's group classified the cause of gate-openings in three categories, (i) chemical moieties (ii) physical moieties and (iii) rotational moieties.[13] Among them, the MOFs possessing chemical moieties for gate-opening are very rare due to its harsh conditions for structural transformation. Therefore, second and third factors have been usually researched with various MOFs. The common examples of gate-opening MOFs having physical moiety for gate-opening are occurred by subnetwork displacement, such as interpenetrated 3D frameworks or interdigitated 2D layer structure. They are usually non-porous because the void space of one frame was taken up by another one, but have potential to make free space through displacement, such as the gliding of 2D layers or swelling.[17]

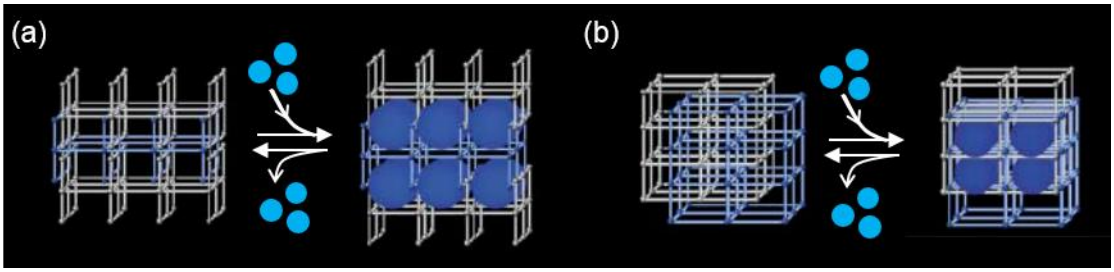


**Figure 1.13.** Gate-opening behavior of interdigitated and interpenetrated structures.

Despite the different types of structural changes of gate-opening, all have showed common properties of sudden uptake of specific guest molecules at a specific pressure. Thus, the kinetic of gate-opening process was studied by measuring gas sorption isotherms with one-point adsorption volumetric measurement method.[20] To study the kinetics of gate-opening MOFs, they synthesized an interdigitated 2D layered framework, {[Cd(bpndc)(bpy)](DMF)($H_2O$)}, with $Cd^{2+}$, benzophenone-4,4'-dicarboxylate ($bpndc^{2-}$), and 4.4'-bipyridyl (bpy). The coordination bonds between $Cd^{2+}$ and $bpndc^{2-}$ form 1D double chains, which are connected by bpy linkers generating 2D layers. Those 2D layers are stacked in interdigitated manner and crystallized into *C*2/*c* space group with guest-containing cavities connected through small window. When {[Cd(bpndc)(bpy)](DMF)($H_2O$)} was activated, the layers were glided and tilted like Figure 1.14 (c) to (d), and the cell volume per Z volume decreased by 14%. As a result, the space group was changed to $P2_1/a$ and the interlayer interactions were formed causing the void space to be isolated by losing the connection on window. Thus, the activated framework, [Cd(bpndc)(bpy)], was non-porous and therefore it didn't adsorb gas molecules, such as $N_2$, $O_2$, and Ar before reaching a certain pressure, a gate opening pressure $P_{go}$.

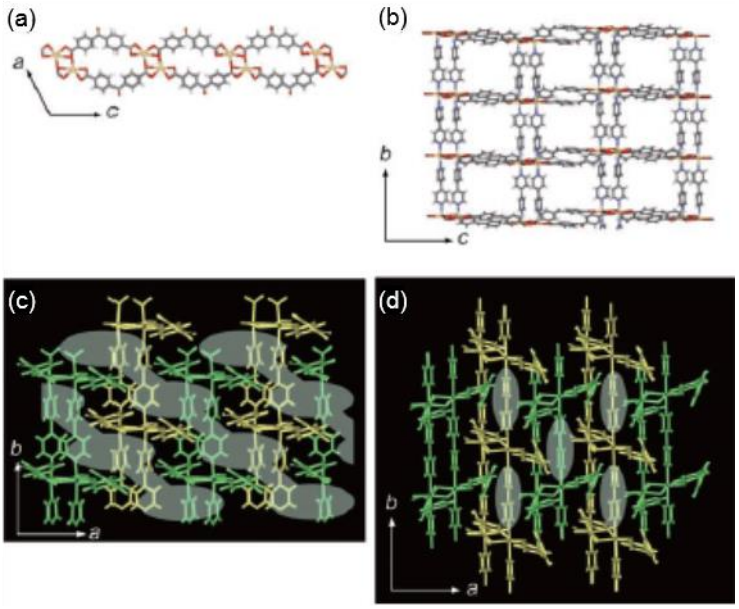


**Figure 1.14.** Structure of {[Cd(bpndc)(bpy)](DMF)($H_2O$)} and {[Cd(bpndc)(bpy)]}. (a) 1D double chain (b) 2D layer (c) Interdigitated 2D layers of {[Cd(bpndc)(bpy)](DMF)($H_2O$)} and (d) Interdigiatated 2D layers of [Cd(bpndc)(bpy)]. (gray shadow : cavities of each structure)

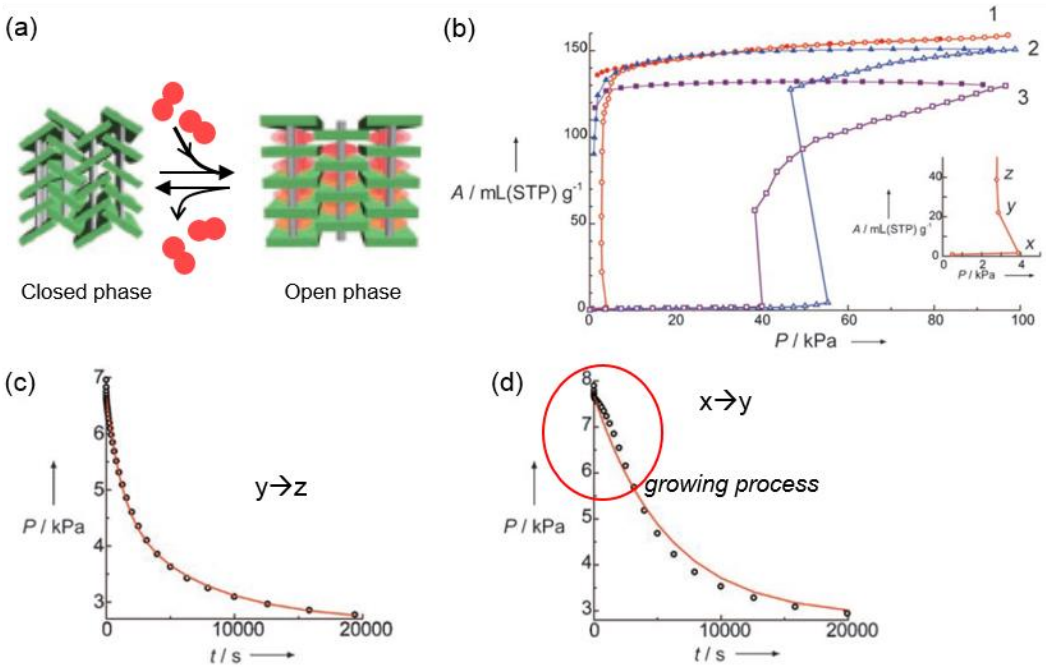


**Figure 1.15.** Properties of {[Cd(bpndc)(bpy)]} during the gas uptake (a) Scheme of gate-opening process. (b) Gas sorption isotherms (1, $O_2$; 2, $N_2$; 3, Ar), and (c) and (d) Comparison of calculated profiles of double exponential (DE) model and the experimental profiles.

Kitagawa's group focused on why the adsorption occurred only after a certain pressure, and therefore they studied on kinetics of gate-opening process. The one-point adsorption measurement before and after $P_{go}$ gave different results, thus they built a hypothesis that there is an intermediate phase for growing cell. (Figure 1.16) The hypothesis suggested that the adsorption of gas is occurred by the diffusion process with double exponential (DE) model (Eq. 1) and the gas molecules are not adsorbed before the gate-opening. Thus, the adsorption process occurred in two steps near or after the gate-pressure, and it is called gate-opening (GO) model (Eq. 2). This was proved by the fitting the experimental isotherms into the calculated isotherms of both DE model (Figure 1.15 (c) and (d)) and GO model (Figure 1.16).

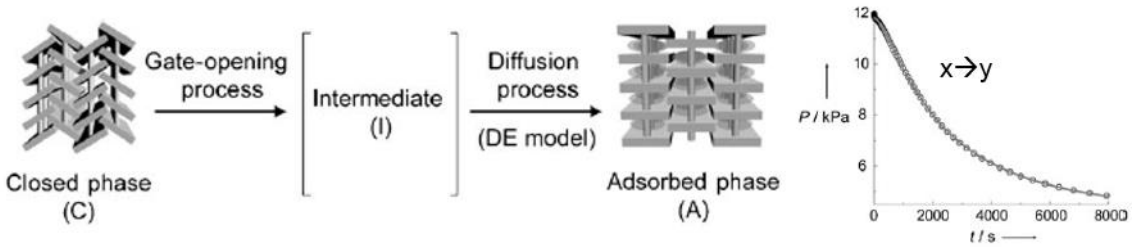


**Figure 1.16.** Gate-opening model

$$P = 0.5\{e^{-k_{d1}t} + e^{-k_{d2}t}\}(P_i - P_e) + P_e \quad \text{(Eq. 1)}$$

$$P = 0.5\left\{\frac{k_{go}e^{-k_{d1}t} - k_{d1}e^{-k_{go}t}}{(k_{go} - k_{d1})} + \frac{k_{go}e^{-k_{d2}t} - k_{d2}e^{-k_{go}t}}{(k_{go} - k_{d2})}\right\}(P_i - P_e) + P_e \quad \text{(Eq. 2)}$$

In addition to finding the gate-opening kinetic model, this research revealed that the dependency of gate-opening process on the boiling point of guest molecules due to the increased intermolecular interaction. In addition, the gate-opening process becomes slower as the temperature increases. Actually, the temperature-dependency of adsorption can be explained by adsorption kinetics, the rate at which the gas molecules strike the solid surface would be reduced upon temperature increase.[26]

Aside from the flexible MOFs possessing gate-opening properties by physical moieties, the rotational moieties give milder structural transition because less of distortion on bonding geometry. However, the rotational moieties should change the void space of framework from non-porous to porous reversibly upon their conformation change in order to show the gate-opening process. Thus, the choice of functional groups on rotational groups are very important for designing the gate-opening MOFs. To satisfy both conditions for free rotation and changes of void space, the rotational and linear ligand with bulky functional groups is a good candidates for synthesis of gate-opening MOFs. Therefore, Kitagawa's group researched a pillared layered MOF with rotatable pillars with flexible pendant groups.[13] Additionally, they added the hydroxyl groups at the end of the flexible side chains

to give the locking/unlocking actions triggered via interactions between pillar-pillar and pillar-guest. They utilized $Cd(NO_3)_2$ and 2,3-pyrazinedicarboxylic acid ($H_2pzdc$), and $Cd^{2+}$ are coordinated by one nitrogen atom and four oxygens from three different $pzdc^{2-}$, forming 2D layers in the *ab* plane. Those layers are pillared by 2,5-bis(2-hydroxyethoxy)-1,4-bis(4-pyridyl)benzene (**L**), generating 3D structure of $\{[Cd_2(pzdc)_2\mathbf{L}(H_2O)_2]\cdot 5(H_2O)(EthOH)\}$ like Figure 1.17. This MOF possesses interconnected 1D channels in *a*- and *b*- axis directions, containing water and ethanol as guest molecules.

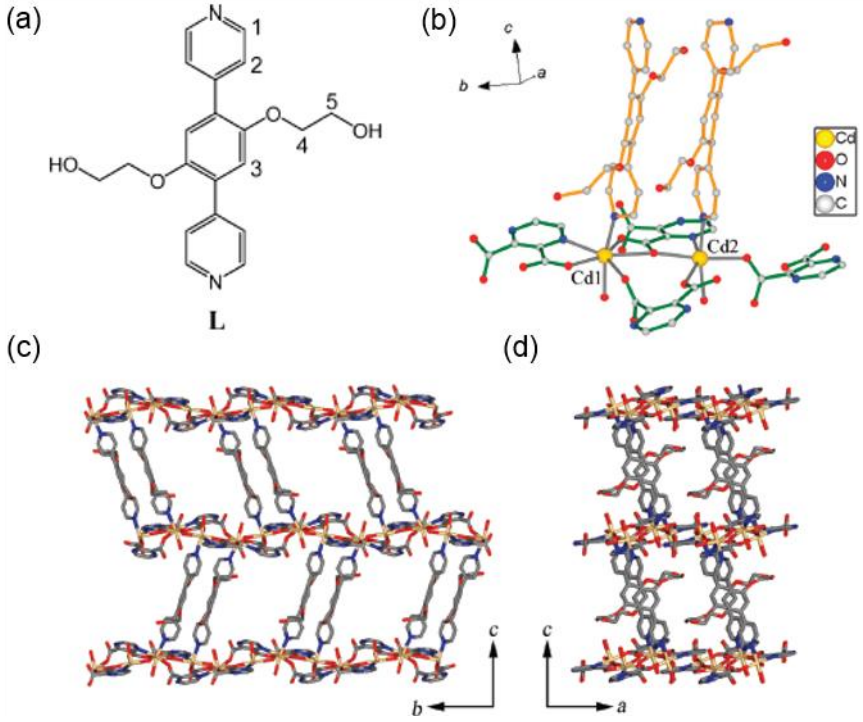


**Figure 1.17.** Structure of $\{[Cd_2(pzdc)_2\mathbf{L}(H_2O)_2]\cdot 5(H_2O)(EthOH)\}$ (a) The rotatable linker (b) View on atomic connectivity (c) View on *bc* plane and (d) View on *ac* plane.

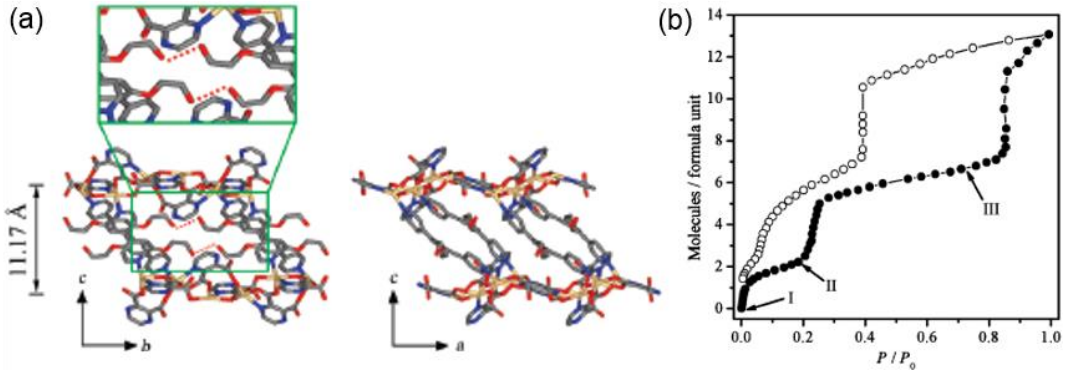


**Figure 1.18.** (a) Structure of $[Cd_2(pzdc)_2\mathbf{L}]$ (b) Water vapor sorption isotherms of $[Cd_2(pzdc)_2\mathbf{L}]$.

After removing the guest molecules, the structure would be distorted like following. The pillars were tilted with reduction in *c*-axis direction and rotated, and those changes caused the coordination around $Cd^{2+}$ would be distorted. In addition, the pillars were stabilized through hydrogen bonding with hydroxyl groups of each other, resulting in the closed pore like Figure 1.18. The void space of structure changed from 35% to 2% of the cell volume during evacuation of guest molecules. The framework, $[Cd_2(pzdc)_2\mathbf{L}]$ showed the gate-opening behavior upon the uptake of water vapor in a three-step adsorption isotherm and a two-step desorption profile. It suggested that the adsorption of water molecules brought about the structural transformation in two-step mechanism like Figure 1.19. At first, hydrogen bonds between hydroxyl groups on the functional chains were broken. Then, the pillars were rotated and the cell was breathed with completely recovering the open structure. But the water molecules couldn't be desorbed completely due to the strong coordination between water and $Cd^{2+}$ thus after desorption the partially dried structure were obtained.

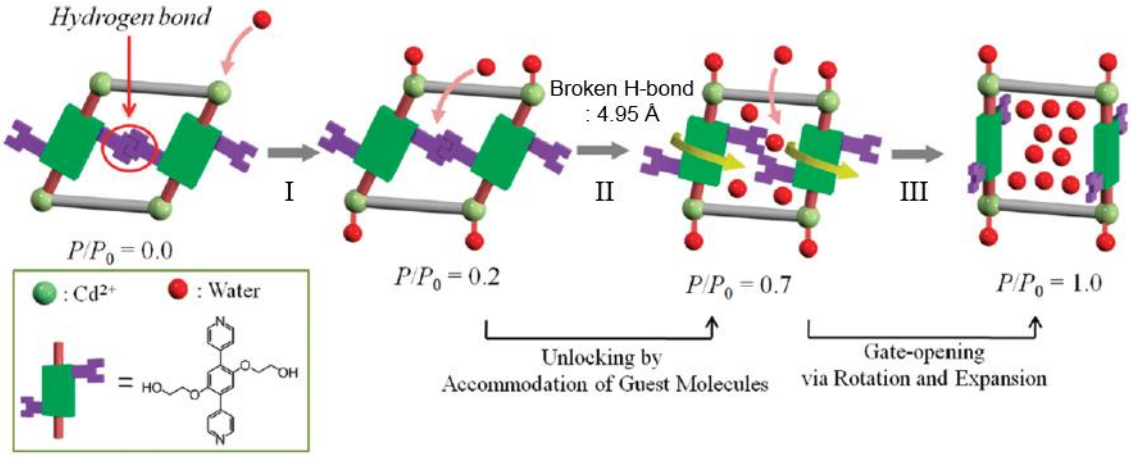


**Figure 1.19.** Schematic representation of gate-opening of $[Cd_2(pzdc)_2\mathbf{L}]$ upon water vapor adsorption.

## I.2. Amine-functionalized metal-organic frameworks

The annual average temperature of the world has been continuously increasing. The global warming is one of serious problems of the world because it affects human life causing problems in various ways, such as chage of food, abnormal weather, and increase in energy consumption.[27] The main cause of global worming is attributed to the contantly increasing concentration of carbon dioxide in the air, which has already reached 390 ppm after 19th century.[1,28] Thus, the government of whole world are trying to decrease the amount of $CO_2$ emission and the concentration of $CO_2$ in the air. However, with human activities increasing more and more, required energy consumption keeps

increasing. As a result, the increase rate of $CO_2$ level is accelerated, temperature keeps rising, and increases energy consumption again. To stop this vicious cycle, we urgently need the development of $CO_2$ adsorbents.

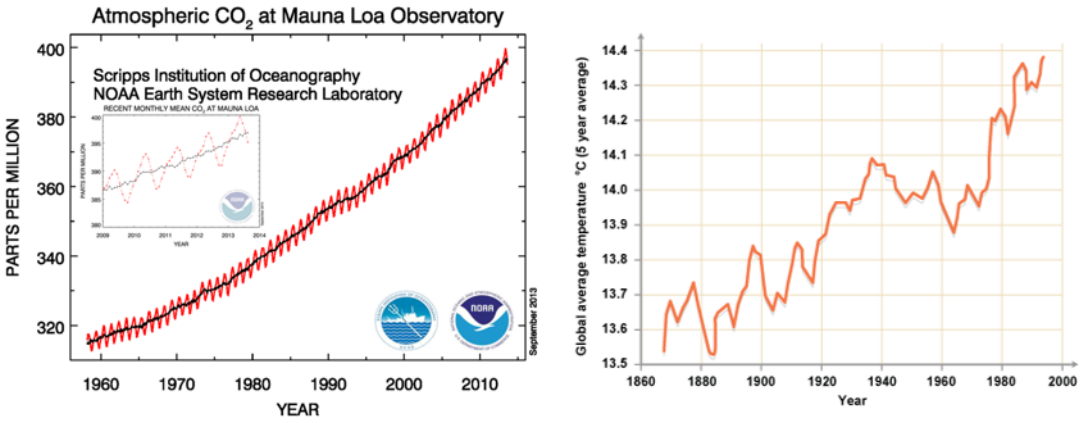


**Figure 1.20.** Trend graph in the level of atmospheric $CO_2$ and in annual average temperature.[28]

The adsorbents are largely classified into two groups: solution adsorbents, and solid adsorbents. The currently used materials in industruies are amine solution, which have lots of problems. The main problem of utilizing amine solution is that solution can be lossed and degraded with generating toxic by-products during process. Additionally, the regeneration energy is too high because they adsorbs $CO_2$ gas molecules through chemically reacting with them, and their large heat capacity makes it hard to reach regeneration temperature, which requires high cost. Therefore, many researchers have focused on the solid adsorbents whose heat capacity is definitely smaller than solution.[1] The solid adsorbents are classified as physisorbents and chemisorbents. Chemisorbents are metal oxide compounds whose basic sites interact with $CO_2$ molecules in the acidic nature.[29] On the other hand, physisorbents are mostly porous solids, sudh as zeolites, activated carbons, and MOFs. However, there is a problem of weak interaction between adsorbents and $CO_2$ gas molecules. Therefore, most of researchers have tried to improve the interaction between $CO_2$ and adsorbents, and it makes MOFs popular in this field.

MOFs are well-ordered coordination polymers that are constructed by assembly of metal building blocks and organic linkers. Because there is a wide range of choice of metal building blocks and organic linkers, we can easily fabricate the structure of MOFs, such as the pore size and the dimension of pore, and can decorate the pore surface with various functional groups. This have attracted many interests in various fields, especially for gas storage.[2, 30] In addition, amines are very famous for selective adsorption of $CO_2$ via chemical bond formation between C of $CO_2$ and N of amines, resulting in carbamates or carbamic acids.[1, 31] Thus, industries have generally used alkylamine

solutions for separate $CO_2$ from flue gas. However, problems of too high regeneration energy and of toxic by-products urge to develop the solid adsorbents. Amine-functionalized MOFs was devised from the conventional $CO_2$ sequestration method, the reaction between amine and $CO_2$, and many MOFs as $CO_2$ adsorbents were studied such as MOF-177, MIL-101, and mmen-CuBTTri (mmen = *N*,*N*-dimethylethylenediamine). [14-16, 32]

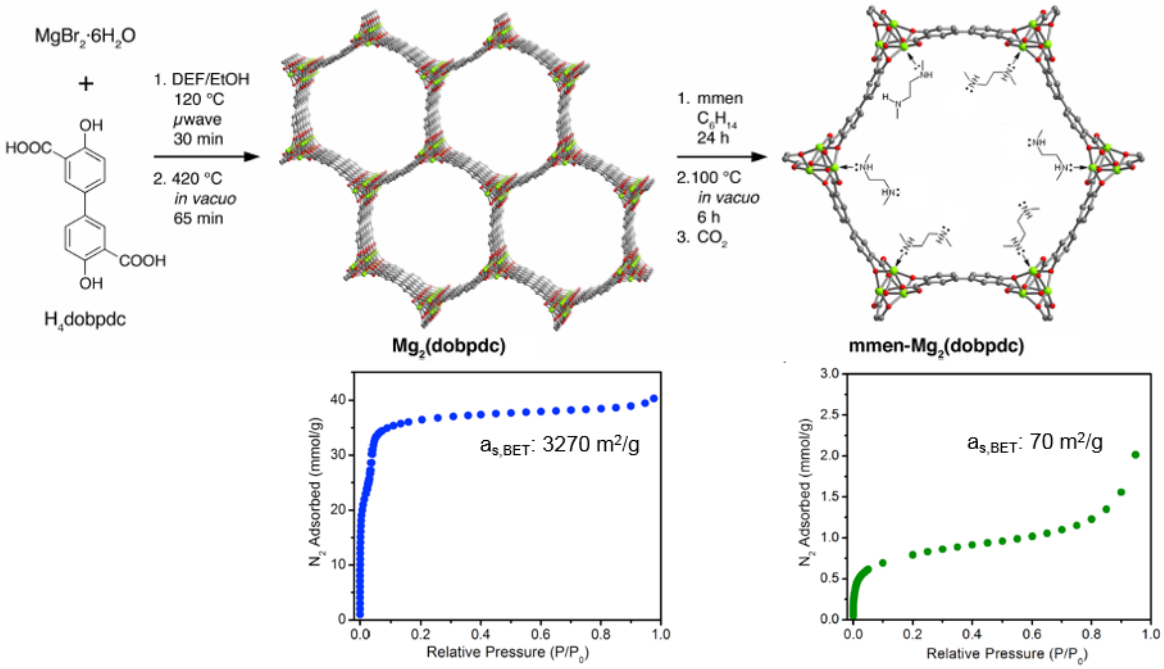


**Figure 1.21.** Schematic representation of functionalization of $Mg_2$(dobpdc).

Among various researches, mmen-$Mg_2$(dobpdc), which was developed and studied by Long's group at 2012, showed a substantial adsorption capacity and a good selectivity of $CO_2$ over $N_2$ at low $CO_2$ partial pressure.[30] As the expanded version of MOF-74, $Mg_2$(dobpdc) possesses same space group, trigonal system with $P3_221$ space group as MOF-74 through coordination between $Mg^{2+}$ and $dobpdc^{2-}$. $Mg^{2+}$ has a distorted octahedral geometry with crystallographically independent three types of oxygen donors from carboxylate and hydroxyl groups of $dobpdc^{2-}$. On the equatorial plane of $Mg^{2+}$, two bridging carboxylates are coordinated in *trans* positions and one hydroxyl oxygen and one non-bridging carboxylic oxygen occupy other sites. Addtionally, a hydroxyl group and one oxygen from DEF are coordinated on the axial sites of $Mg^{2+}$. To functionalize $Mg_2$(dobpdc) with alkylamine groups, metal-coordinated DEF molecules were removed at 420 °C under vacuum condition for 65 min resulting in the open metal sites on the pore surface. The open metal sites were used for grafting the diamine-functional groups via immersion of activated crystals in the hexane and mmen solution, producing mmen-$Mg_2$(dobpdc). 80% of open metal sites were occupied by mmen and the remaining

sites were coordinated by water. After grafting alkylamine groups on the pore, the structure and the crystallinity were intact but the pore size and the BET surface area were considerably reduced from 3270 $m^2/g$ to 70 $m^2/g$ because mmen took up the pore. Although the large reduction of the surface area and pore size, the adsorption capacity of mmen-$Mg_2$(dobpdc) for $CO_2$ at 25 °C was not significantly decreased from that of $Mg_2$(dobpdc). At the $CO_2$ level in the air, 0.39 mbar of $CO_2$ partial pressure, mmen-$Mg_2$(dobpdc) adsorb 2.0 mmol/g (8.1 wt) of $CO_2$, which is 15 times higher than $Mg_2$(dobpdc). Moreover, mmen-$Mg_2$(dobpdc) showed that the $CO_2$ uptake reached 3.13 mmol/g (12.1 wt%) at 0.15 bar and 3.86 mmol/g (14.5 wt%) at 1 bar. Considering the increased density of mmen- $Mg_2$(dobpdc) due to mmen functionalization, it showed comparable capacity to $Mg_2$(dobpdc) (Table 1.1).

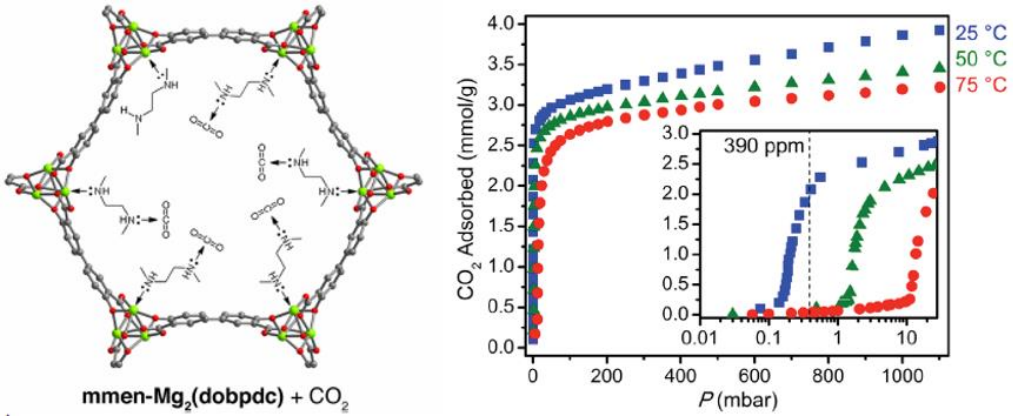


**Figure 1.22.** $CO_2$ adsorption of mmen-$Mg_2$(dobpdc).

**Table 1.1.** Volumetric capacity of $Mg_2$(dobpdc) and mmen-$Mg_2$(dobpdc).

| | Density ($g/cm^3$) | $CO_2$ capacity ($mmol/cm^3$) | |
|---|---|---|---|
| | | 0.15 bar | 1 bar |
| $Mg_2$(dobpdc) | 0.58 | 2.8 | 3.7 |
| mmen-$Mg_2$(dobpdc) | 0.86 | 2.7 | 3.3 |

At low pressure, $CO_2$ adsorption isotherms indicated prominent steps and it hindered the calculation of isosteric heat of adsorption with common Lanmuir-Freundlich equation. That steps were caused by the $CO_2$-triggered rearrangement of alkylamine groups with making interaction between neighboring amine groups in *c*-axis for reacting with $CO_2$.[33] Thus, $CO_2$ was adsorbed via weak interaction site instead of strong adsorption sites, amines, at low pressure. Therefore, dual-site Langmuir-Freundlich equation (Eq. 3) was used to model the $CO_2$ adsorption before the step. In

addition, the modified Langmuir-Freundlich equation (Eq. 4) was employed to consider three sites for adsorption and an extra pressure paramenter where the step occurred in the isotherm.

$$q = \frac{q_{sat,A} b_A p^{\alpha_A}}{1+b_A p^{\alpha_A}} + \frac{q_{sat,B} b_B p^{\alpha_B}}{1+b_B p^{\alpha_B}} \quad \text{(Eq. 3)}$$

$$q = \frac{q_{sat,A} b_A (p-p^*)^{\alpha_A}}{1+b_A (p-p^*)^{\alpha_A}} + \frac{q_{sat,B} b_B (p-p^*)^{\alpha_B}}{1+b_B (p-p^*)^{\alpha_B}} + \frac{q_{sat,C} b_C (p-p^*)^{\alpha_C}}{1+b_C (p-p^*)^{\alpha_C}} \quad \text{(Eq. 4)}$$

$$(\ln p)_q = \left(\frac{Q_{st}}{R}\right)\left(\frac{1}{T}\right) + C \quad \text{(Eq. 5)}$$

Using Clausius-Clapeyron equation (Eq. 5) and the fitted isotherms via previous equations, the isosteric heat of mmen-$Mg_2$(dobpdc) was caculated. The calculated isosteric heat of adsorption accorded with the existence of two adsorption sites for $CO_2$ with different interaction strength. At low loading of $CO_2$, the heat of adsorption suggested very weak adsorption but it quickly increased to -71 kJ/mol, maintained until 2.5 mmol/g of $CO_2$ loading and it decreased slowly.

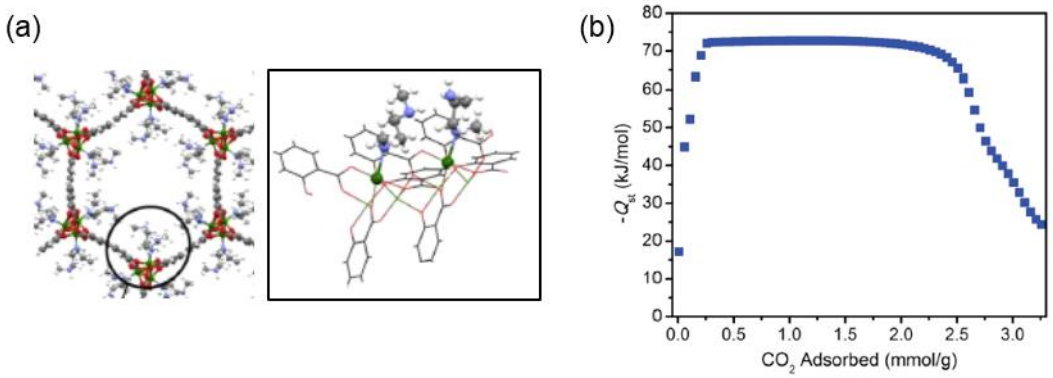


**Figure 1.23.** (a) Interaction of neighboring amine groups along *c*-axis. (b) Isosteric heat of $CO_2$ adsorption onto mmen- $Mg_2$(dobpdc).

The fact that isosteric heat kept until 2.5 mmol/g (~ 0.75 $CO_2$/mmen) suggested that the reaction stoichiometry is different from the conventional chemistry of solution reaction with amine:$CO_2$ = 2:1 mechanism. Thus, new mechanism for reaction between amine and $CO_2$ in solid phase of amine:$CO_2$ = 2:2 stoichiometry was suggested by Gagliardi et al.[33] The proposed mechanism suggested two neighboring amine groups are required for $CO_2$ adsorption by amine molecules in solid phase and it results in bis-carbamic acids stabilized by double hydrogen bonds. The reaction between amine and $CO_2$ is same as the conventional mechanism, but the product after the uptake of first $CO_2$ molecules aren't the most stable form. Thus, the second $CO_2$ molecules are adsorbed consecutively after first uptake, bringing about the stable bis-carbamic acids. The calculated isosteric heat of adsorption by

this mechanism is -69.13 kJ/mol, which is good agreement with the experiment done by Long et al. However, the high isosteric heat value dropped after 75% of amine groups occupied by $CO_2$. The pore blockage effect, the existence of hydrogen bonded amines, and the coorperative binding mechanism were suggested as the reason for drops of strong interaction.[30]

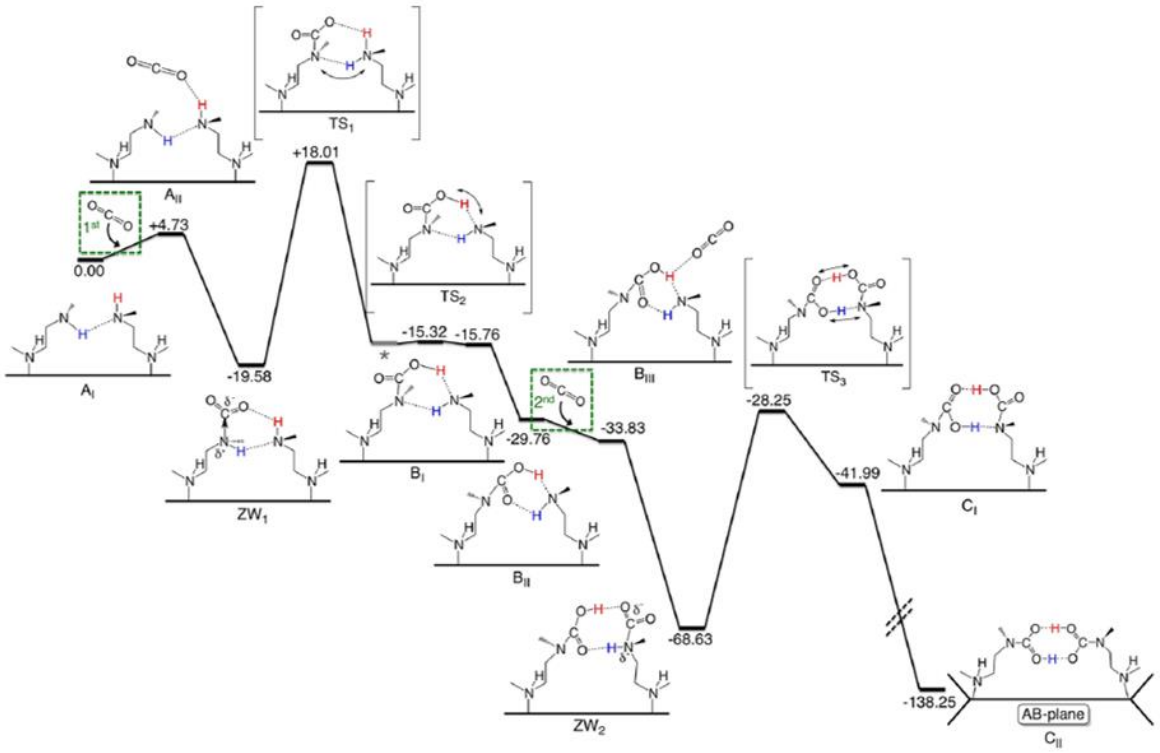


**Figure 1.24.** Reaction mechanism proposed by Gagliardi et al.

The strong interaction between $CO_2$ and amines calculated from the proposed mechanism suggested mmen-$Mg_2$(dobpdc) adsorbs $CO_2$ with high selectivity over $N_2$, and the experimental data from Long's group proved it by calculating the selectivity of $CO_2$.[30] Because the isotherm of mmen-$Mg_2$(dobpdc) couldn't be modeled with a single equation over entire range of pressure, ideal adsorbed solution theory (IAST) couldn't calculate the selectivity of mmen-$Mg_2$(dobpdc). Thus, the selectivities were calculated via following equation. When the adsorption capacity of component $n$ is $q_n$ at the pressure of component $p_n$, selectivity (S) and purity of adsorbed $CO_2$ gas are defined according to Eq. 6 and 7. The resulting selectivity and purity of mmen-$Mg_2$(dobpdc) for $CO_2$ capture at simulated air (0.39 mbar $CO_2$, 21% $O_2$ balanced with $N_2$) and at dry flue gas (0.15 bar $CO_2$ balanced with $N_2$) are represented in Table 1.2.

$$S = \frac{q_{CO_2}/q_2}{p_{CO_2}/P_2} \qquad \text{(Eq. 6)} \qquad\qquad Purity = \frac{q_{CO_2}}{q_{CO_2}+q_2} \qquad \text{(Eq. 7)}$$

**Table 1.2.** Selectivity and purity of adsorbed $CO_2$ by mmen-$Mg_2$(dobpdc).

| Gas condition | Component 2 | $CO_2$ pressure (mbar) | Component 2 pressure (mbar) | Selectivity | Purity |
|---|---|---|---|---|---|
| Air | $N_2$ | 0.4 | 800 | 49000 | 96% |
| Flue gas | $N_2$ | 150 | 750 | 200 | 98% |

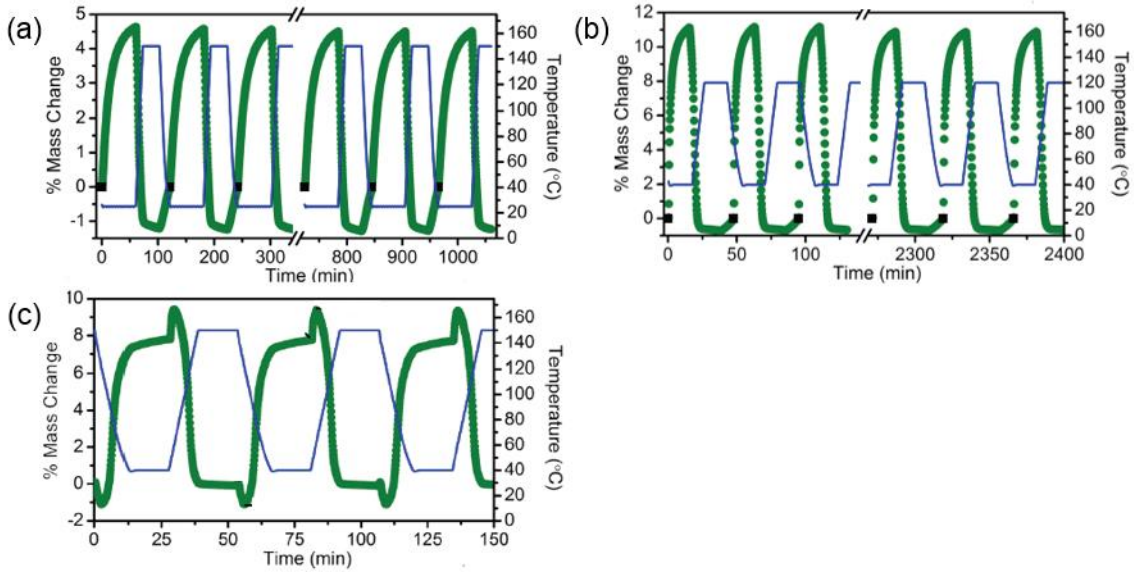


**Figure 1.25.** Adsorption-desorption cycling for mmen-$Mg_2$(dobpdc) with (a) simulate air and (b) dry flue gas. (c) A temperature swing process, dry flue gas for adsorption at 40 °C and 100% $CO_2$ for desorption at 150 °C.

Additionally, mmen-$Mg_2$(dobpdc) showed good adsorption capacity and cyclability under simulated air and flue gas flow. 390 ppm $CO_2$ with $N_2$ and $O_2$ was flowed over the sample at 40 °C for 1 h gave 4.6% of mass change. The complete regeneration of sample was realized by heating at 150 °C under $N_2$ flow, leading to no loss of capacity over repeating cycles. Furthermore, the adsorption of dry flue gas condition (15% $CO_2$ in $N_2$) at 40 °C presented 11.1% mass change and the adsorpbent was regenerated at 120 °C under $N_2$ flow, realizing insignificant capacity loss (0.2%) after 50 cycles. For achieving good capacity at more realistic condition, without a $N_2$ purge, they tested $CO_2$ adsorption cycling via temperature swing protocol. It was done via flowing 15% $CO_2$ in $N_2$ over the sample at 40 °C for adsorption and 100% $CO_2$ at 150 °C for desorption, and it showed a good performance.

Recently, another amine functionalized $Mg_2$(dobpdc) with enhanced $CO_2$ capacities was reported by Hong et al.[31] They grafted $Mg_2$(dobpdc) with primary amine, ethylenediamine (en), generating en-$Mg_2$(dobpdc). en-$Mg_2$(dobpdc) possesses less reduced BET surface area (1253 $m^2/g$) than mmen-$Mg_2$(dobpdc), and therefore it could show higher capacity of $CO_2$ with higher selectivity (Table 1.2). Despite the ultradilute concentration of $CO_2$, en-$Mg_2$(dobpdc) adsorbed significant amount of $CO_2$ (2.83 mmol/g) which exceeds those of well-performing adsorbents such as PEI/Zr-SBA-15 series (PEI = poly(ethyleneimine)) and hyperbranched aminosilica (HAS).[34] In addition, its isosteric heat of $CO_2$ adsorption was in the range of 49~51 kJ/mol indicating the formation of carbamic acid and it can be decomposed via heating over 130 °C.

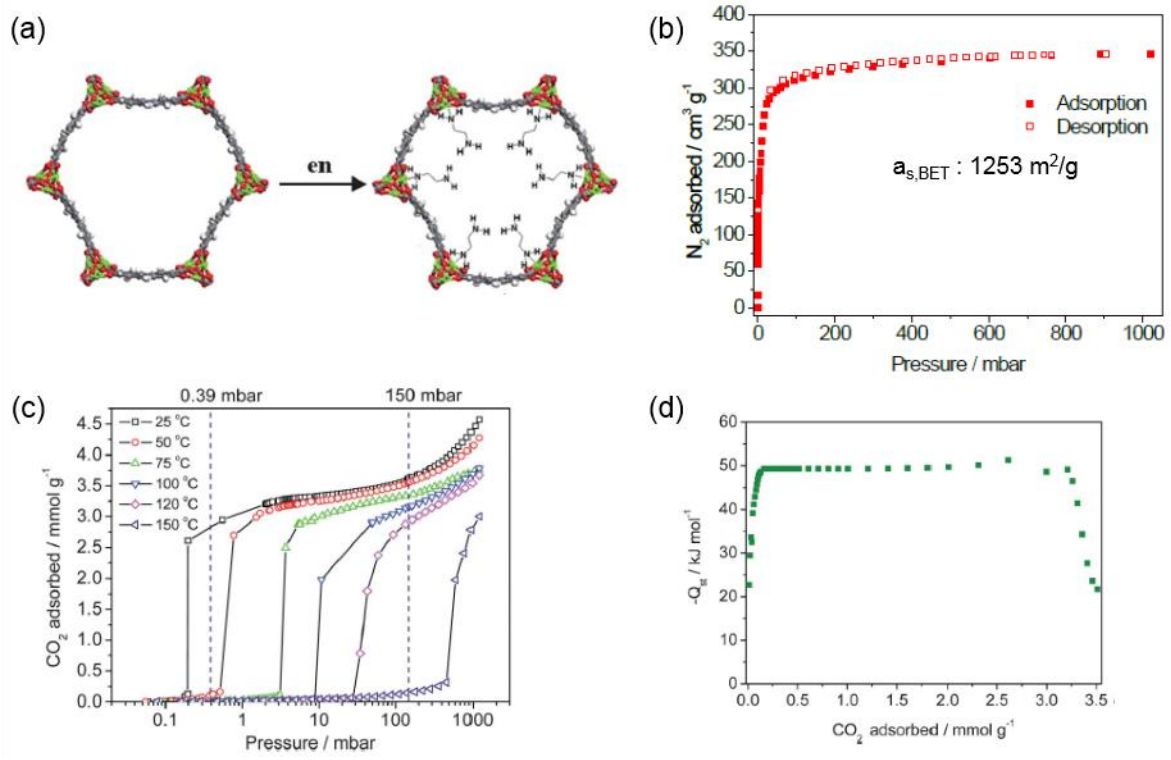


**Figure 1.26.** (a) Scheme for en functionalization of $Mg_2$(dobpdc). Gas sorption isotherms of (b) $N_2$ at 77 K and (c) $CO_2$. (d) The isosteric heat of $CO_2$ adsorption for en-$Mg_2$(dobpdc).

**Table 1.3.** $CO_2$ adsorption capacity and selectivity of $CO_2$ for en-$Mg_2$(dobpdc).

| | 0.39 mbar | 0.15 bar | 1 bar |
|---|---|---|---|
| $CO_2$ capacity (mmol/g) | 2.38 (11.1 wt%) | 3.62 (13.7 wt%) | 4.57 (16.7 wt%) |
| Selectivity | 70000 | 230 | - |

Therefore, en-$Mg_2$(dobpdc) can be applied for reversible $CO_2$ adsorption-desorption process via temperature swing protocol. The flow of simulated air onto the activated en-$Mg_2$(dobpdc) at 25 $^oC$ for 15 h gave 11.8 wt% of $CO_2$ adsorption, and it completely desorbed under same flow at 150 $^oC$ for 2 h (Figure 1.27 (a)). Then, the capacity loss was just 6% after 5 cycles, suggesting the exceptional high $CO_2$ uptake at very dilute $CO_2$ level. Moreover, en-$Mg_2$(dobpdc) selectively adsorbed $CO_2$ (14.6 wt%) in the flow of flue gas at 40 $^oC$ for 90 min, and it could be regenerated under Ar flow at 150 $^oC$ for 90 min leading to 3% capacity loss over 5 cycles (Figure 1.27 (b)). To apply to practical condition, the stability in humidity of en-$Mg_2$(dobpdc) was tested by adsorption-desorption cycles with 6 min exposure of 100% RH after adsorption of $CO_2$ under flue gas and regenerated under Ar at 150 $^oC$ (Figure 1.27 (d)). Remarkably, just 5 % capacity loss after 5 cycles was observed and therefore en-$Mg_2$(dobpdc) suggested good cyclability in temperature swing protocol. Furthermore, the $CO_2$ adsorption rate of en-$Mg_2$(dobpdc) was the best among the prominent porous materials, recording 10 wt% $CO_2$ adsorption within 30 seconds (Figure 1.27 (c)).

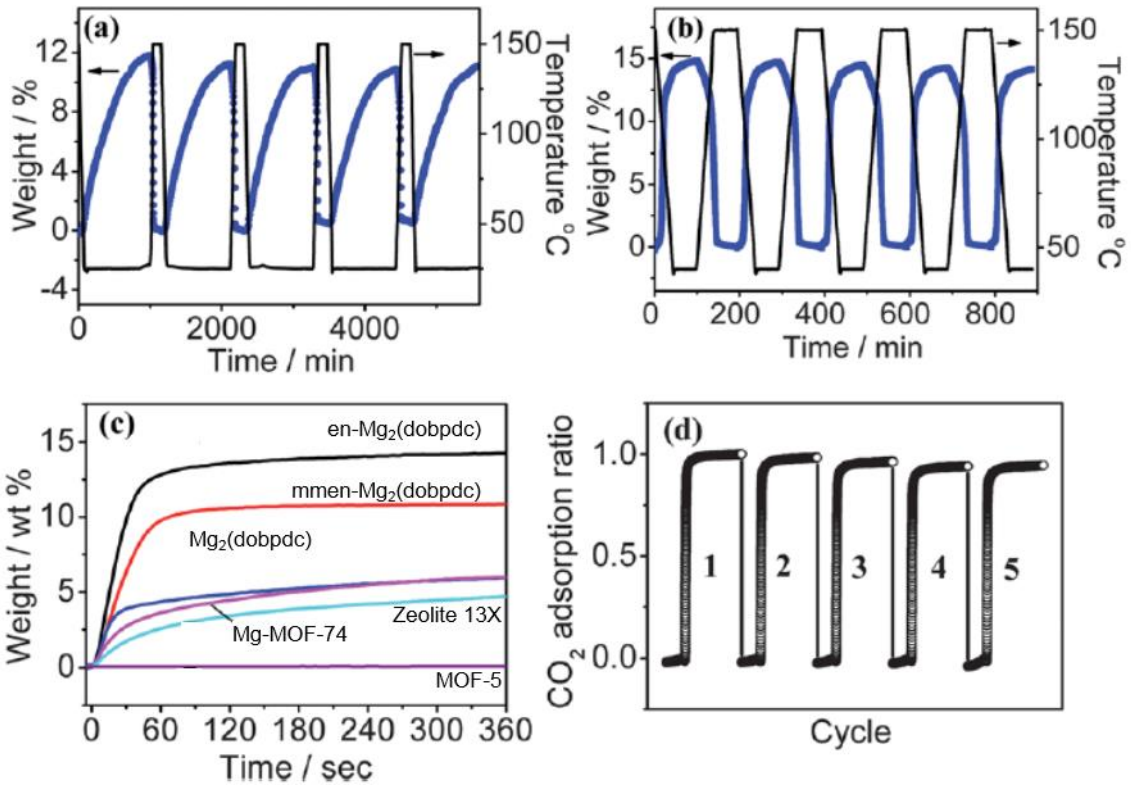


**Figure 1.27.** Adsorption-desorption cycling of $CO_2$ for en-$Mg_2$(dobpdc) with (a) simulated air, (b) simulated flue gas. (c) Time-dependant CO2 adsorption for porous materials. (d) $CO_2$ adsorption ratio of en-$Mg_2$(dobpdc) in flue gas after 6 min exposure to 100% RH at 21 $^oC$ to en-$Mg_2$(dobpdc) in flue gas.

## II. Experimental Section

**Materials and Methods.** All chemicals and solvents used in the syntheses were of reagent grade and they were used without further purification. 2,2',5,5'-tetramethylbiphenyl, 98% was bought from Alfa Aesar and meso-1,2,3,4- butanetetracarboxylic acid ($H_4$BuTC), >98% and 4,4-biphenyldicarboxylic acid ($H_2$BPDC), >97% were purchased from TCI. 1,1'-biphenyl-2,2',5,5'-tetracarboxylic acid ($H_4$BPTC) was prepared by the previously reported method.[35] Acetonitrile (MeCN) was dried by distillation with $P_2O_5$ in a Ar atmosphere prior to use. Infrared spectra were measured by a Thermo Fisher Scientific Nicolet 6700 FT-IR spectrometer. Thermogravimetric analysis (TGA) were performed under $N_2$(g) atmosphere at a scan rate of 5 $^oC$/min using Q50 from TA instruments. UV/Vis diffuse reflectance spectra were recorded with a Cary 5000 UV/Vis spectrophotometer. Elemental analyses were done by UNIST Central Research Facilities center (UCRF) in Ulsan National Institute of Science and Technology (UNIST).

### Syntheses

**Sodium 4,4-biphenyldicarboxylate ($Na_2$BPDC).** 4,4-biphenyldicarboxylic acid ($H_2$BPDC) (2.42 g, 0.01 mol) was dispersed in water (25 mL) by stirring with a magnetic stirrer. NaOH solution, which is prepared through dissolving NaOH (1.20 g, 0.03 mol) in 7 mL water, was added to $H_2$BPDC mixture solution then the white powder was dissolved and small amount of solids were appeared soon. To help further precipitation of products, 20 mL of ethanol (EthOH) was put into the solution and the solution was kept in refrigerator over 3 hours. The white powder was filtered, washed with EthOH, and dried by evacuation under air. Yield: ~72.8%

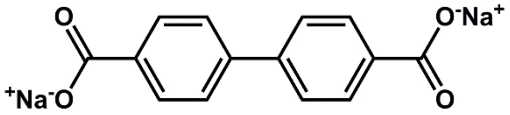


**Figure 2.1.** $Na_2$BPDC.

**$[Ni(C_{14}H_{34}N_6)](ClO_4)_2$ ($[NiL_{propyl}](ClO_4)_2$).** $[NiL_{propyl}](ClO_4)_2$ was prepared by the reported methods with a little modification.[36] $NiCl_2 \cdot 6H_2O$ (11.8 g, 0.05 mol) was dissolved in methanol (MeOH) (50 mL) placed in an ice-bath, and 99% ethylenediamine (6.8 mL, 0.10 mol) was added dropwise to it. Paraformaldehyde (7.50 g, 0.25 mol) and propylamine (7.4 mL, 0.10 mol) were then added at room temperature, slowly with stirring. The remaining paraformaldehyde was dissolved by heating and refluxing it the reaction mixture for 12 h. The dark green solution was filtered while hot to remove by-products like nickel hydroxide, and the filtrate was placed in an ice-bath. Then, 5 mL of

70% $HClO_4$ was added very slowly with stirring and $NaClO_4$ (ca. 3 g) was added. Then yellow solid product was formed, which were filtered off, washed with MeOH, and dried under vacuum. Yield: 21.5%. It was recrystallized from MeCN/$H_2O$ mixture by heating. Then, orange-yellow crystalline product was obtained, filtered, washed with MeOH, and dried under vacuum condition. Yield: 46.3% Anal. Calcd for $Ni_1C_{14}H_{34}N_6O_8Cl_2$: C, 30.91; H, 6.30; N, 15.44.; Found: C, 30.74; H, 6.27; N, 15.67. FT-IR for $[NiL_{propyl}](ClO_4)_2$ (KBr pellet): $\nu_{N-H}$ 3206, $\nu_{ClO4^-}$ = 1117 $cm^{-1}$. UV-Vis (diffuse reflectance spectrum): $\lambda_{max}$= 454 nm

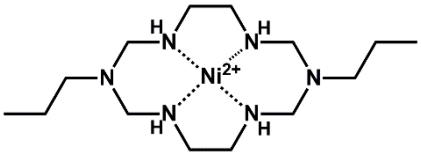

**Figure 2.2.** $[NiL_{propyl}](ClO_4)_2$.

**$[Ni(C_{14}H_{30}N_6)](ClO_4)_2$ ($[NiL_{allyl}](ClO_4)_2$).** $[NiL_{allyl}](ClO_4)_2$ was prepared by modifying the methods for synthesizing hexaaza Ni(II) macrocyclic complexes.[36] $NiCl_2{\cdot}6H_2O$ (11.9 g, 0.05 mol) was dissolved in MeOH (50 mL) placed in an ice-bath, and 99% ethylenediamine (7.0 mL, 0.10 mol) was added dropwise to it. Paraformaldehyde (7.5 g, 0.25 mol) and allylamine (8.4 mL, 0.11mol) were then added at room temperature, slowly with stirring. The remaining paraformaldehyde was dissolved by heating and refluxing it the reaction mixture for 12 h. A pale purple-color powder was formed after 12 h. The powder product was filtered and dissolved in water, and its color turned to yellow. The solution was filtered, and the filtrate was placed in an ice-bath. Then, $HClO_4$ was added very slowly with stirring. The product obtained as yellow precipitates was filtered, washed with MeOH and dried under vacuum. Yield: ~ 25 %. Anal. Calcd for $Ni_1C_{14}H_{30}N_6O_8Cl_2$: C, 31.14; H, 5.60; N, 15.56.; Found: C, 30.51; H, 5.65; N, 15.47. FT-IR for $[NiL_{allyl}](ClO_4)_2$ (KBr pellet): $\nu_{C=C(allylic)}$ 1643, $\nu_{C=C-H}$ 3082, $\nu_{(ClO4)^-}$ 1088 $cm^{-1}$. UV-Vis: $\lambda_{max}$= 455 nm, $\varepsilon$ = 30.20 $M^{-1}cm^{-1}$

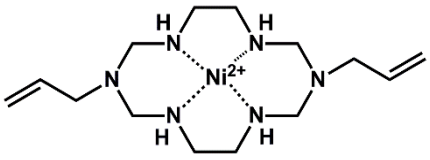

**Figure 2.3.** $[NiL_{allyl}](ClO_4)_2$.

**$[Ni(C_{12}H_{32}N_8)](ClO_4)_2$ ($[NiL_{amine}](ClO_4)_2$).** $[NiL_{amine}](ClO_4)_2$ was prepared by modifying the method reported in the previous study.[37] $Ni(OAc)_2{\cdot}4H_2O$ (9.0 g, 0.04 mol) was dissolved in methanol (MeOH) (50 mL) placed in an ice-bath, and 99% ethylenediamine (10.8 mL, 0.16 mol) was added dropwisely to it. Paraformaldehyde (6.1 g, 0.20 mol) was then added and dissolved with stirring at

room temperature. Then, the reaction mixture was refluxed for 12 h. After 12 h reaction, the mixture solution was placed in an ice-bath and $HClO_4$was added very slowly to pH 5~6 with stirring. The mixture solution was kept in room temperature over 1 week until the yellow powder was precipitated. The precipitates were filtered and reduced by triethylamine (TEA) solution in MeCN solvent. The final product was filtered and dried under vacuum. Yield: ~ 14 %. Anal. Calcd for $Ni_1C_{12}H_{32}N_8O_8Cl_2$: C, 26.40; H, 5.91; N, 20.52.; Found: C, 26.73; H, 5.89; N, 20.46. FT-IR for $[NiL_{amine}](ClO_4)_2$ (KBr pellet): $\nu_{N\text{-}H}$ 3304, 3225, $\nu_{ClO4^-}$ = 1093 $cm^{-1}$. UV-Vis (diffuse reflectance spectrum, $\lambda_{max}$): 450 nm

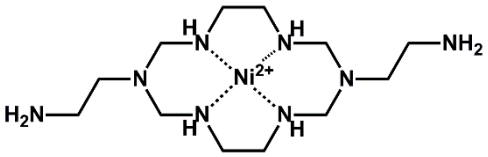

**Figure 2.4.** $[NiL_{amine}](ClO_4)_2$.

**{[($NiL_{propyl}$)$_2$(BPTC)]·4DMF·4$H_2O$} (1-as)**. $[NiL_{propyl}](ClO_4)_2$ (0.020 g, 0.037 mmol) and $H_4$BPTC (0.006 g, 0.018 mmol) were dissolved in mixture solution of *N*,*N*-dimethylformamide (DMF) and $H_2O$ with volume ratio of 1.5 mL:1.5 mL and 2 mL:1 mL with TEA 20 μL respectively. The solution of $H_4$BPTC was diffused onto the former solution and allowed to stand at room temperature. After 1 day pale purple crystals started to be formed and fully synthesized 7 days later. Yield: ~40.5%. Anal. Calcd for $Ni_2C_{56}H_{110}N_{16}O_{16}$: C, 48.71; H, 8.03; N, 16.23.; Found: C, 47.88; H, 8.13; N, 16.34. FT-IR for **1-as** (ATR): $\nu_{N\text{-}H}$ 3247, $\nu_{C\text{-}H(aromatic)}$ 3149, $\nu_{C=O(DMF)}$ 1668, $\nu_{as(O\text{-}C=O)}$ 1568, 1542 (split), $\nu_{s(O\text{-}C=O)}$ 1376, 1348 (split) $cm^{-1}$. UV-Vis (diffuse reflectance spectrum, $\lambda_{max}$): 505 nm.

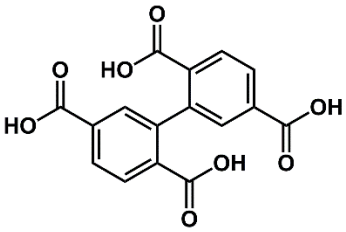

**Figure 2.5.** $H_4$BPTC.

**{[($NiL_{propyl}$)$_2$(BPTC)]$_{1/2}$·3MeCN·3$H_2O$} (1-MeCN).** The mother liquor containing crystals of as-synthesized **1-as** was decanted carefully by pipette, and the crystals were re-immersed in distilled MeCN for 1 day with refreshing the solvent 3 times. FT-IR for **1-MeCN** (ATR): $\nu_{N\text{-}H}$ 3249, $\nu_{C\text{-}H(aromatic)}$ 3148, $\nu_{C\equiv N}$ 2251, $\nu_{as(O\text{-}C=O)}$ 1581, 1544 (split), $\nu_{s(O\text{-}C=O)}$ 1378, 1347 (split) $cm^{-1}$. UV-Vis (diffuse reflectance spectrum, $\lambda_{max}$): 500 nm.

**Partially dried compound {[(NiL$_{propyl}$)$_2$(BPTC)]·x(H$_2$O)} (1').** To analyze the structural change of **1-as** during activation, the partially dried compound **1'** was prepared due to fully activated compound lost the single crystallinity. The crystals of **1-as** was heated at 45 $^oC$ for 1.5 h under air condition by using convention oven, then **1'** was obtained.

**[(NiL$_{propyl}$)$_2$(BPTC)] (1). 1-MeCN** was used for preparing activated sample **1**. **1-MeCN** was filtered and evacuated at 110 $^oC$ for 4 h under vacuum. Then, cooled the sample and refilled the gas with Ar. Anal. Calcd for $Ni_1C_{22}H_{37}N_6O_4$: C, 51.08; H, 7.40; N, 16.25.; Found: C, 50.78; H, 7.46; N, 16.37. FT-IR for **1** (ATR): $\nu_{N-H}$ 3259, $\nu_{C-H(aromatic)}$ 3142, $\nu_{as(O-C=O)}$ 1577, 1543 (split), $\nu_{s(O-C=O)}$ 1371, 1342 (split) $cm^{-1}$. UV-Vis (diffuse reflectance spectrum, $\lambda_{max}$): 509 nm.

**{[(NiL$_{allyl}$)$_2$(BuTC)]·2DEF·2H$_2$O} (2-as)**. [NiL$_{allyl}$](ClO$_4$)$_2$ (0.123 g, 0.2mmol) and H$_4$BuTC (0.028 g, 0.1mmol) were dissolved in mixture solution of *N*,*N*-diethylformamide (DEF) and H$_2$O respectively with volume ratio of 2 mL:0.9 mL and 2 mL:1 mL with TEA 125 μL. The solution of H$_4$BuTC was diffused onto the former solution and allowed to stand at room temperature for 7 days until pale purple crystals formed. Yield: 32.8%. Anal.Calcd for $Ni_2C_{46}H_{92}N_{14}O_{12}$: C, 48.01; H, 8.06; N, 17.04.; Found: C, 47.29; H, 8.25; N, 16.96. FT-IR for **2** (KBr pellet): $\nu_{C=O(DEF)}$ 1663, $\nu_{as(O-C=O)}$ 1558, $\nu_{C=C(allylic)}$ 1644, $\nu_{C=C-H}$ 3083 $cm^{-1}$. UV-Vis (diffuse reflectance spectrum,$\lambda_{max}$): 510 nm ($Ni^{2+}$ d-d transition), 332 nm (allylic double bond n – π* transition), 210 nm (double bond π – π* transition).

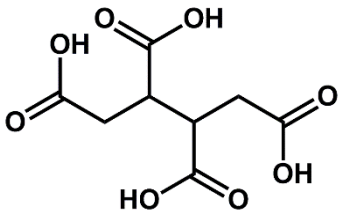


**Figure 2.6.** H$_4$BuTC.

**[(NiL$_{allyl}$)$_2$(BuTC)] (2)**. The as-synthesized compounds **2-as** was heated in round bottom flasks at 100 $^oC$ under vacuum for 7 h. Then, cooled the sample and refilled the gas with Ar. Anal. Calcd for $Ni_2C_{36}H_{66}N_{12}O_8$: C, 47.39; H, 7.29; N, 18.42.; Found: C, 46.44; H, 7.38; N, 18.85. FT-IR for **2** (ATR): $\nu_{as(O-C=O)}$ 1560, $\nu_{C=C(allylic)}$ 1644, $\nu_{C=C-H}$ 3083 $cm^{-1}$. UV-Vis (diffuse reflectance spectrum, $\lambda_{max}$): 516 nm.

**Dried compound [$(NiL_{allyl})_2$(BuTC)] obtained by a supercritical carbon dioxide drying method. (2-sc**) The as-synthesized crystals of **2-as** were soaked in DEF for 1 d. Using supercritical $CO_2$ in a Tousimis Samdri PVT-3D critical point dryer, the sample was dried. The sample in fresh DEF solvent was placed in the chamber, and exchanged DEF with liquid $CO_2$ completely. The $CO_2$ filling was kept for 2 h and then followed by a purge vent for 10 min, which was repeated five times before heating. The sample and liquid $CO_2$ in chamber was heated to 40 ℃ and kept under the supercritical condition (typically 1300 psi) for 1 h. The $CO_2$ was slowly vented overnight from the chamber at 40 ℃.

**{[$(NiL_{allyl})_2$(BuTC)]·3$H_2O$} (3-as).** $[NiL_{allyl}](ClO_4)_2$ (0.120 g, 0.2mmol) was dissolved in mixture solution of MeCN (1.0 mL) and $H_2O$ (0.4 mL) and MeCN solution (1 mL) of $H_4$BuTC (0.027 g, 0.1mmol) with TEA 120 μL was diffused onto the former solution at room temperature. Yield: 63.5%. Anal. Calcd for $Ni_2C_{36}H_{72}N_{12}O_{11}$: C, 44.74; H, 7.51; N, 17.7.; Found: C, 44.50; H, 7.53; N, 17.50. FT-IR for **1** (KBr pellet): $\nu_{as(O\text{-}C=O)}$ 1556, $\nu_{C=C(allylic)}$ 1640, $\nu_{C=C\text{-}H}$ 3075 $cm^{-1}$. UV-Vis (diffuse reflectance spectrum, $\lambda_{max}$): 511 nm ($Ni^{2+}$ d-d transition), 331 nm (allylic double bond n – π* transition), 215 nm (double bond π – π* transition).

**[$(NiL_{allyl})_2$(BuTC)] (3)**. The as-synthesized compounds **3-as** was heated in round bottom flasks at 100 $^oC$ under vacuum for 7 h. Then, cooled the sample and refilled the gas with Ar. Anal. Calcd for $Ni_2C_{36}H_{66}N_{12}O_8$: C, 47.39; H, 7.29; N, 18.42.; Found: C, 46.65; H, 7.48; N, 19.08. FT-IR for **3** (ATR): $\nu_{as(O\text{-}C=O)}$ 1556, $\nu_{C=C(allylic)}$ 1643, $\nu_{C=C\text{-}H}$ 3080 $cm^{-1}$. UV-Vis (diffuse reflectance spectrum, $\lambda_{max}$): 510 nm.

**{[$(NiL_{amine})$(BPDC)]·3$H_2O$} (4-as).** $[NiL_{amine}](ClO_4)_2$ (0.04 g, 0.14 mmol) and $Na_2$BPDC (0.02 g, 0.14 mmol) were dissolved respectively in 4 mL of DEF and in mixture solution of MeCN and $H_2O$ with volume ratio of 2 mL:1 mL. The solution of $Na_2$BPDC was diffused onto the former solution. The mixture solution allowed to stand at room temperature for 1 days until the pale purple crystals were formed with powder. Only crystals were used for analyses. Yield: 22.7 %. Anal. Calcd for $Ni_1C_{26}H_{46}N_8O_7$: C, 48.69; H, 7.23; N, 17.47.; Found: C, 49.36; H, 7.10; N, 17.52. FT-IR for **4-as** (KBr pellet): $\nu_{N\text{-}H}$ 3366, 3294, $\nu_{C\text{-}H(aromatic)}$ 3165, $\nu_{as(O\text{-}C=O)}$ 1587, $\nu_{s(O\text{-}C=O)}$ 1379, $\nu_{N\text{-}H\ bending}$ 1540 $cm^{-1}$. UV-Vis (diffuse reflectance spectrum, $\lambda_{max}$): 517 nm ($Ni^{2+}$ d-d transition).

**[($NiL_{amine}$)(BPDC)] (4).** The as-synthesized compounds **4-as** was heated in round bottom flasks at 90 $^{o}$C under vacuum for 7 h. Then, cooled the sample and refilled the gas with Ar. Anal. Calcd for $Ni_1C_{26}H_{40}N_8O_4$: C, 53.17; H, 6.86; N, 19.08.; Found: C, 52.47; H, 6.91; N, 18.78. FT-IR for **4** (ATR): $\nu_{N\text{-}H}$ 3356, 3292, $\nu_{C\text{-}H(aromatic)}$ 3140, $\nu_{as(O\text{-}C=O)}$ 1588, $\nu_{s(O\text{-}C=O)}$ 1373, $\nu_{N\text{-}H\ bending}$ 1542 $cm^{-1}$. UV-Vis (diffuse reflectance spectrum, $\lambda_{max}$): 512 nm.

**{[($NiL_{propyl}$)(BPDC)]·2.5$H_2O$} (5-as)**. [$NiL_{propyl}$]($ClO_4$)$_2$ (0.02 g, 0.07 mmol) and $Na_2$BPDC (0.01 g, 0.07mmol) were dissolved respectively in mixture solution of acetonitrile and $H_2O$ with volume ratio of 0.5 mL:0.5 mL and 1 mL of water. The solution of [$NiL_{propyl}$]($ClO_4$)$_2$ was diffused onto the latter solution. Pale purple crystals started to form immediately and the mixture solution allowed to stand at room temperature for 3 days until the solution was diffused completely. Yield: 89.0 %. Anal. Calcd for $Ni_2C_{56}H_{94}N_{12}O_{13}$: C, 53.35; H, 7.51; N, 13.33.; Found: C, 53.16; H, 7.52; N, 13.51.FT-IR for **5-as** (KBr pellet): $\nu_2{}^{o}{}_{N\text{-}H}$ 3294, $\nu_{C\text{-}H(aromatic)}$ 3154, $\nu_{as(O\text{-}C=O)}$ 1589 and 1543, $\nu_{s(O\text{-}C=O)}$ 1377 $cm^{-1}$. UV-Vis(diffuse reflectance spectrum, $\lambda_{max}$): 507 nm ($Ni^{2+}$ d-d transition).

**[($NiL_{propyl}$)(BPDC)] (5).** The as-synthesized compounds **5-as** was heated in round bottom flasks at 120 $^{o}$C under vacuum for 6 h. Then, cooled the sample and refilled the gas with Ar. Anal. Calcd for $Ni_1C_{28}H_{42}N_6O_4$: C, 57.45; H, 7.23; N, 14.36.; Found: C, 56.58; H, 7.40; N, 14.52. FT-IR for **5** (ATR): $\nu_{N\text{-}H}$ 3297, $\nu_{C\text{-}H(aromatic)}$ 3137, $\nu_{as(O\text{-}C=O)}$ 1593 and 1545, $\nu_{s(O\text{-}C=O)}$ 1370 $cm^{-1}$. UV-Vis (diffuse reflectance spectrum, $\lambda_{max}$): 510 nm.

**Low-pressure gas sorption measurement.** The gas sorption isotherms were measured by using BELsorp-MAX. To prepare the samples for sorption measurements, **1-MeCN** crystals were fileted and introduced to the gas sorption apparatus. Then, the sample was activated at 110 $^{o}$C under vacuum for 4 h. For **2** and **3**, crystals of **2-as** and **3-as** were loaded to gas sorption apparatus after fitration and the outgassing process was carried out under vacuum at 100 $^{o}$C till all the guest molecules were removed (ca. 7 h). For **4** and **5**, the filtered crystals were added to the gas sorption apparatus, and the samples were heated at 90 $^{o}$C under vacuum for 7 h. After that, the gas sorption was measured. The $N_2$ and $CO_2$ gas sorption isotherms for desolvated solids were monitored at 77 K, 195 K, and 298 K, respectively. And $H_2$ gas sorption isotherms were measured at 77 K.

**High-pressure gas sorption measurement.** High-pressure gas sorption isotherm for $CO_2$ gas was measured on a PCTpro E&E - 122. To prepare the sample for high-pressure gas sorption measurements, **1-MeCN** crystals were filtered, loaded in a sample holder, and evacuated at 110 $^oC$ for 4 h under vacuum. $CO_2$ isotherm measurement was performed over a pressure range of 0 - 45 bar at 308 K.

**X-ray Powder Diffraction (XRPD) Analysis.** The XRPD data of **2-as**, **2**, **3-as**, **3**, **5-as**, and **5** are collected with Bruker D8 Advance at 40 kV and 40 mA with copper radiation ($K\alpha_1$ = 1.5406Å and $K\alpha_2$ = 1.54439 Å). Samples were grinded finely by mortar and were put on low background sample holder. The crystals of **2-as** were prepared with dampled comdition ground in mother liquor due to easy structural trasformation through losing guest during sample preparation. Others were finely ground after filtration. Whole data were recorded with 0.02$^o$ step. The damped sample of **2-as** was measured with scan rate of 0.2 s/step, and the data were recored with scan rate of 0.5 s/step for **2** and **3**. The scan rate of 1 s/step was applied for other measurements.

**Synchrotron XRPD measurment.** The diffraction data were measured with transmission-mode as Debye-Scherrer Pattern with the 180 mm of sample-to-detector distance in 60 s exposure on an ADSC Quantum-210 detector at 2D SMC with a silicon (111) double crystal monochromator (DCM) at the Pohang Accelerator Laboratory, Korea. In-situ variable pressure PXRD was measured with a custom-made vacuum manifold and goinometer head. The ADX program[40] was used for data collection, and the Fit2D[41] program was used for conversion of integrated 2D to 1D patterns, for wavelength and detector distance refinement and for a calibration measurement of a NIST Si 640c standard sample. The XRPD patterns of **1-as** were collected at 195 K and 298 K with synchrotron radiation ($\lambda$ = 1.19998 Å). Because of high flexibility of frameworks, their structures were changed during preparation of XRPD measurement with losing some of their guest molecules in air. Therefore, crystals were finely ground in mother liquor and filled in capillary respectively (diameter, 0.3 mm; wall thickness, 0.01 mm) then the solvent was removed carefully through evacuating slowly under vacuum at ambient temperature. For **4-as** and **4**, the XRPD patterns were measured at 100 K with synchrotron radiation ($\lambda$ = 1.20029 and 1.20024 Å, respectively). The mother liquor of **4-as** crystals were decanted by filtration, and the resulting solids were finely ground and packed in capillary (diameter, 0.3 mm; wall thickness, 0.01 mm). To prepare the sample **4**, the filtered crystals of **4-as** were dried at 90 $^oC$ under vacuum for 7 h, they were finely ground and packed in capillary under Ar atmosphere in glove box (diameter, 0.3 mm; wall thickness, 0.01 mm).

***in-situ* synchrotron XRPD experiment for 1.** To prepare the XPRD samples, the MeCN solvent containing **1-MeCN** crystals was decanted carefully by pipette and evacuated under vacuum at 343 K for 2 h. After that, the crystals were groud and packed into capillary (diameter, 0.3 mm; wall thickness, 0.01 mm) under Ar atmosphere in glove box. Then, the capillary was evacuated at 383 K until sample was fully dried under vacuum (ca. 15 min). After activation, the sample was cooled down to the measurement temperature by using a cryostream, 195 K and 298 K respectively, under vacuum. To observe the structural transformation induced by adsorbing $CO_2$ gas the diffraction patterns were measured with applying various pressure of $CO_2$ gas to capillary at 195 K and 298 K, respectively. The diffraction data were collected with synchrotron radiation ($\lambda$ = 1.39992 Å) at both 195 K and 298 K. For 195 K measurement, XRPD patterns during adsorption of $CO_2$ were sequentially collected at 0.006, 0.16, 0.19, 0.22, 0.39, 0.53, 0.66, 0.79, 0.89, and 1.00 atm, and for desorption measurement at 0.79, 0.59, 0.49, 0.30, 0.20, 0.14, 0.08, 0.05, and 0.006 atm. After 20 min from applying each pressure to the sample, the patterns were collected except for 0.53 atm during adsorption measurement. At 0.53 atm, the XRPD patterns were measured after 20, 30, 40, and 50 min. In addtion, the sample for high pressure measurement from 0 bar to 30 bar at 298 K, XRPD patterns were obtaind sequentailly at 0, 1, 5, 10, 15, 18, 21, 24, 27, and 30 bar for adsorption step and at 27, 24, 21, 18, 15, 12, 9, 5, 1, and 0 bar during desorption measurements. Each pattern was collected 5 min after injection of gas pressure to the sample.

**Single-Crystal X-ray crystallography.** Single-crystals were coated with paratone-*N* oil because they lost their crystallinity upon exposure to the air. The diffraction data measured using synchrotron employing a PLSII-2D SMC an ADSC Quantum-210 detector with a silicon (111) double crstal monochromator (DCM) at Pohang Accelerator Laboratory, Korea. The ADSC Q210 ADX program[40] was used for both data collection, and HKL3000sm (Ver. 703r)[42] was used for cell refinement, reduction and absorption correction. The structures of **1-as**, **1-MeCN**, **1'**, **4-as**, and **5-as** were solved using direct methods with SHELX-XS (Ver. 2013/1) and refined by full-matricx least-squares calculation with SHELX-XL (Ver. 2013/4) program package.[43] For the crystal structures of **2-as** and **3-as** was solved by the direct method and refined by full-matrix least-squares calculations with the SHELX-TL (Ver. 2008) program package.[43] All non-hydrogen atoms in whole structures were refined anisotropically except one of the disordered allyl group in **2-as**. The hydrogen atoms were assigned isotropic displacement coefficients U(H) = 1.2U (C,N) or 1.5($C_{methyl}$), and their coordinates were allowed to ride on their respective atoms. For the structures of **2-as** and **3-as**, all the methyl hydrogen atoms and some hydrogen atoms on the carbon atoms are not included during the least-squares

refinement. A summary of the crystals and some crystallographic data are given in Table 1, 10-11, S1 - S24, S26 - S27, and S29 - S30. CCDC 975745 - 975747, CCDC-922874 and CCDC-922875 contain the supplementary crystallographic data. The data can be obtained free of charge at www.ccdc.cam.ac.uk/conts/retrieving.html or from the Cambridge Crystallographic Data Centre, 12, Union Road, Cambridge CB2 EX, UK.

**Crystal Structure Determination of 1-as.** The diffraction data of **1-as** crystal were measured at 100K ($\lambda$ = 0.65002 Å), 195 K ($\lambda$ = 0.65002 Å) and at 298 K ($\lambda$ = 0.62998 Å). The whole structure of **1-as**, two half of ligands, two half of Ni ions, one half of $BPTC^{4-}$ and two unligated DMF and water molecules were observed as an aymmetric unit. The structural solvent of DMF with poor geometry was restrained using geometrically DFIX and DANG during the least-squares refinement. The final refinements were performed for **1-as** with the modification of the structure factors for the contribution of the disordered solvent electron densities using the SQUEEZE routine of PLATON.[44] Refinement of the structure **1-as** measured at 195 K converged at a final $R_1$ = 0.0416, $wR_2$ = 0.1308 for 30043 reflections with $I > 2\sigma(I)$; $R_1$ = 0.0426, $wR_2$ = 0.1319 for all reflections. The largest difference peak and hole were 0.478 and -0.397e·Å$^{-3}$, respectively. Refinement of the structure **1-as** measured at 298 K converged at a final $R_1$ = 0.0499, $wR_2$ = 0.1742 for 37780 reflections with $I > 2\sigma(I)$; $R_1$ = 0.0539, $wR_2$ = 0.1792 for all reflections. The largest difference peak and hole were 0.567 and -0.659e·Å$^{-3}$, respectively.

**Crystal Structure Determination of 1-MeCN.** The diffraction data of **1-MeCN** crystal were measured at 100K ($\lambda$ = 0.62998 Å), 195 K ($\lambda$ = 0.62998 Å) and at 298 K ($\lambda$ = 0.70001 Å). The whole structure of **1-MeCN**, two half of ligands, two half of Ni ions, one half of $BPTC^{4-}$ and two unligated MeCN and water molecules were observed as an aymmetric unit. For the data collected at 100 K, the structural solvent of water possessed large thermal factors. For the data obtained at 195 and 298 K, the structural solvent of MeCN with poor geometry was restrained using geometrically DFIX and DANG during the least-squares refinement. The final refinements were performed for **1-MeCN** with the modification of the structure factors for the contribution of the disordered solvent electron densities using the SQUEEZE routine of PLATON.[44] Refinement of the structure **1-MeCN** measured at 195 K converged at a final $R_1$ = 0.0416, $wR_2$ = 0.1308 for 30043 reflections with $I > 2\sigma(I)$; $R_1$ = 0.0426, $wR_2$ = 0.1319 for all reflections. The largest difference peak and hole were 0.478 and -0.397e·Å$^{-3}$, respectively. Refinement of the structure **1-MeCN** measured at 100 K converged at a final $R_1$ = 0.0375, $wR_2$ = 0.1073 for 34930 reflections with $I > 2\sigma(I)$; $R_1$ = 0.0395, $wR_2$ = 0.1089 for all

reflections. The largest difference peak and hole were 0.515 and -0.964 e·Å$^{-3}$, respectively. Refinement of the structure **1-MeCN** measured at 195 K converged at a final $R_1$ = 0.0424, $wR_2$ = 0.1342 for 35719 reflections with $I > 2\sigma(I)$; $R_1$ = 0.0451, $wR_2$ = 0.1374 for all reflections. The largest difference peak and hole were 0.676 and -0.591 e·Å$^{-3}$, respectively. Refinement of the structure **1-MeCN** measured at 298 K converged at a final $R_1$ = 0.0749, $wR_2$ = 0.2111 for 31598 reflections with $I > 2\sigma(I)$; $R_1$ = 0.0944, $wR_2$ = 0.2272 for all reflections. The largest difference peak and hole were 0.458 and -0.596 e·Å$^{-3}$, respectively.

**Crystal Structure Determination of 1'.** The diffraction data of **1'** crystals was measured at 195 K ($\lambda$ = 0.79999 Å). For the structure of **1'**, four half of ligands, four half of Ni ions, one BPTC and unligated water molecules were observed as an asymmetric unit. The final refinement was performed for **1'** with the modification of the structure factors for the contribution of the disordered solvent electron densities using the SQUEEZE routine of PLATON.[44] Refinement of the structure **1'** measured at 195 K converged at a final $R_1$ = 0.0792, $wR_2$ = 0.2151 for 12344 reflections with $I > 2\sigma(I)$; $R_1$ = 0.0946, $wR_2$ = 0.2267 for all reflections. The largest difference peak and hole were 1.036 and -0.591e·Å$^{-3}$, respectively.

**Crystal Structure Determination of 2-as and 3-as.** The diffraction data of **2-as** and **3-as** were measured at 100 K Two half of ligands, two half of Ni ions, one half of BuTC and an unligated water molecule were observed as an asymmetric unit. One of the disordered allylgroup in the ligand was restrained using SIMU, DELU and ISOR for **2-as** and using ISOR for **3-as** during the least-squares refinement. For **2-as**, the C-C and C=C in allyl group were restrained using DFIX and DANG andthe structural solvent of DEF was restrained using geometrically DFIX and DANG and using SIMU, DELU and ISOR during the least-squares refinement. The final refinement was performed for **2-as** with the modification of the structure factors for the contribution of the disordered solvent electron densities using the SQUEEZE option of PLATON.[44] Refinement of the structure **2-as** converged at a final $R_1$ = 0.0684, $wR_2$ = 0.2033 for 7882 reflections with $I > 2\sigma(I)$; $R_1$ = 0.0758, $wR_2$ = 0.2101 for all reflections. The largest difference peak and hole were 0.750 and -0.763 e·Å$^{-3}$, respectively. Refinement of the structure **3-as** converged at a final $R_1$ = 0.0812, $wR_2$ = 0.2411 for 17306 reflections with $I > 2\sigma(I)$; $R_1$ = 0.0988, $wR_2$ = 0.2570 for all reflections. The largest difference peak and hole were 1.484 and -0.889 e·Å$^{-3}$, respectively.

**Crystal Structure Determination of 4-as and 5-as.** The diffraction data of **4-as** and **5-as** were measured at 100 K. An half of ligands, an half of Ni ions, an half of BPDC and two unligated water molecule were observed as an asymmetric unit. For the structure **4-as**, the alkyl amine pendant group and one unligated water molecule in the ligand was restrained using ISOR during the least-squares refinement. Refinement of the structure **4-as** converged at a final $R_1$ = 0.0652, $wR_2$ = 0.1975 for 16864 reflections with $I > 2\sigma(I)$; $R_1$ = 0.0696, $wR_2$ = 0.2034 for all reflections. The largest difference peak and hole were 0.696 and -0.533 e·Å$^{-3}$, respectively. Refinement of the structure 5**-as** converged at a final $R_1$ = 0.0472, $wR_2$ = 0.1263 for 20065 reflections with $I > 2\sigma(I)$; $R_1$ = 0.0542, $wR_2$ = 0.1321 for all reflections. The largest difference peak and hole were 0.682 and -0.394 e·Å$^{-3}$, respectively.

## III. Results and Discussion

**X-ray structure of 1-as.** The single crystals of **1-as** was synthesized through the self-assembly of $[NiL_{propyl}]^{2+}$ and $BPTC^{4-}$ in DMF and $H_2O$ mixture solution, yielding the pale purple crystals of $\{[(NiL_{propyl})_2(BPTC)]\cdot 4DMF\cdot 4H_2O\}$ (**1-as**). The fundamental building unit of **1-as** is shown in Figure 3.1, constructed through coordination bonds between carboxylate groups of $BPTC^{4-}$ and $[NiL_{propyl}]^{2+}$ resulting in six-coordinated octahedral Ni(II) centers. Two phenyl rings of $BPTC^{4-}$ are twisted by an angle of 47.432(47)° and bridged four macrocycles to construct a three dimensional (3D) network. The network of **1-as** possesses the monoclinic system with space group *C*2/*c*, and it contains two kinds of Ni(II) macrocycles, Ni1A and Ni2B, which are located on different environment. The pendant chain of Ni1A has disordered positions but only one part is represented on figure to clearly show the connectivity (0.66:0.34).

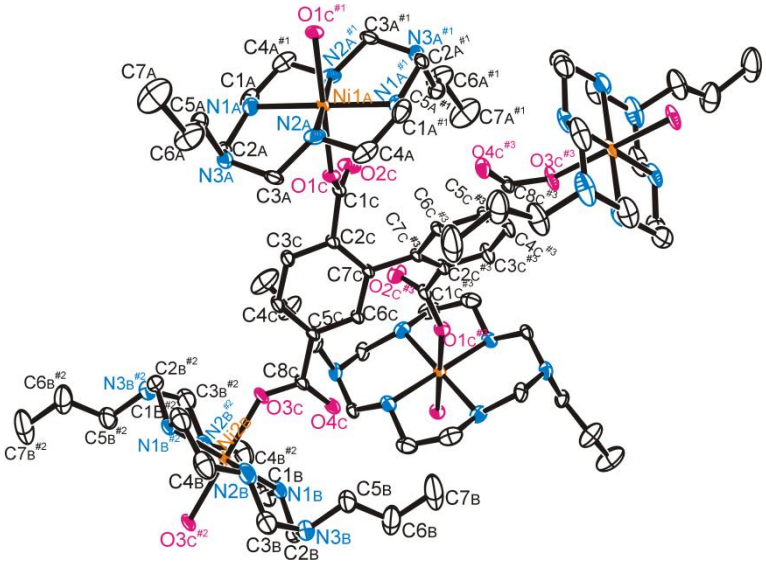


**Figure 3.1.** An ORTEP drawing of **1-as** at 195 K with an atomic numbering scheme (thermal ellipsoids at 30% probability). Symmetry transformations used to generate equivalent atoms:
#1 -x,-y,-z #2 -x+1/2,-y-1/2,-z+1 #3 -x,y,-z+1/2

The axial positions of macrocycles are occupied by oxygen atoms from carboxylate anions of two different $BPTC^{4-}$ ligands in monodentate fashion with average Ni-O distance of 2.1251(6) Å. In addition, every non-coordinating oxygen of carboxylate makes hydrogen bond with one of N-H of the macrocycle (N2A···O2C 2.8596(18) Å, ∠N2A-H2A···O2C 152.3° and N1B···O4C 2.9377(19) Å, ∠N1B-H1B···O4C 151.5°). Among them, O4C makes hydrogen bond with another N-H of the macrocycle of Ni1A (N1A···O4C 2.9784(18) Å, ∠N1A-H1A···O4C 131.2°) as well as that of Ni2B complex.

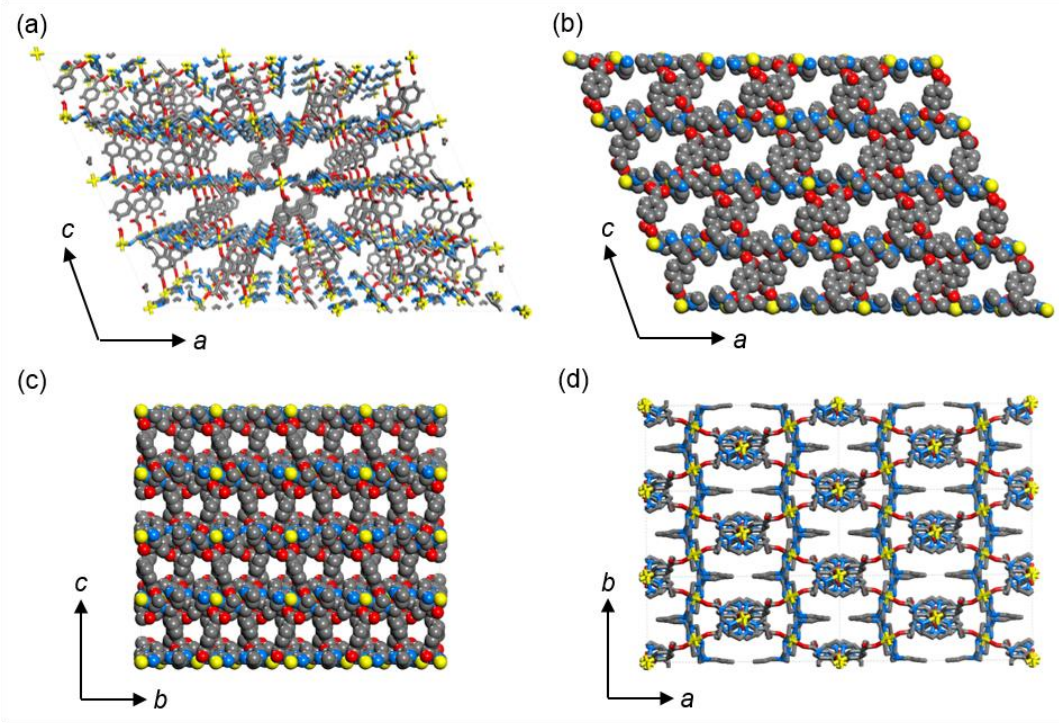


**Figure 3.2.** The structure of **1-as** measured at 195 K (a) A perspective view on *ac* plane. (b) A CPK view on a*c* plane. (c) A CPK view on *bc* plane. (d) A view on *ab* plane (Ni, yellow; C, gray; N, blue; O, red)

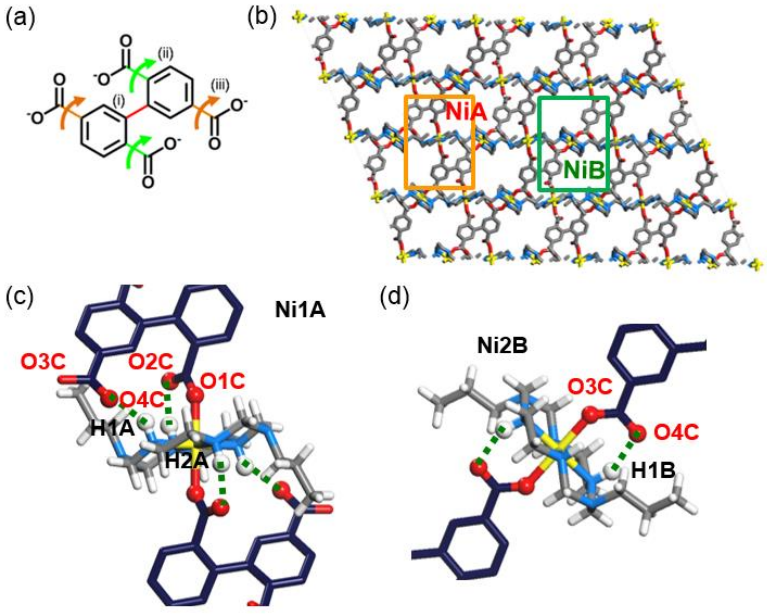


**Figure 3.3.** (a) Freely rotatable single bonds of $BPTC^{4-}$ with labeling. (b) A view on *ab* plane. (c) & (d) An extended view for showing hydrogen bonds between N-H of macrocyclic complex and O of carboxylate (b) of Ni1A. (c) of Ni2B.

Therefore, the macrocycle of Ni1A gets four hydrogen bonds from two different carboxylates, whereas that of Ni2B has two hydrogen bonds. As a result, it makes difference in hydrogen bond energy between two macrocycles in the structure as -81.1 kcal/mol and -41.3 kcal/mol for complex of Ni1A and Ni2B, respectively. Later, this exerts a significant influence on those flexible behaviors upon guest removal and gas uptake. Additionally, two carboxylate groups are twisted with respect to phenyl ring by an angles of 66.080(113)$^{o}$ (angle (i)) for $COO^{-}$ (O1C-C1C-O2C) (angle (ii)) and 7.798(72)$^{o}$ for $COO^{-}$ (O3C-C8C-O4C) (angle (iii)). Three kinds of dihedral angles of $BPTC^{4-}$ makes building units be connected helically in the direction of *b*-axis forming three-dimensional (3D) framework possessing 3D interconnected pores in *a*- and *b*-axis direction. The effective aperture size of pore is 4.5 Å x 3.2 Å in *a*-axis direction and 4.0 Å x 6.7 Å in *b*-axis direction, and the void volume is 40.2% of cell volume, as estimated by PLATON.[44] These channels are filled with guest solvent molecules, but these could not be refined on X-ray structure due to large thermal disorders. Therefore, the number and sort of guest molecules are analyzed through IR spectra, TGA analysis, and elemental analysis. The result revealed that **1-as** contains two DMF and two $H_2O$ molecules per one nickel atom as guest molecules. The detailed crystallographic information and selected bond length and angles are listed on Table 3.1 and S1 to S3.

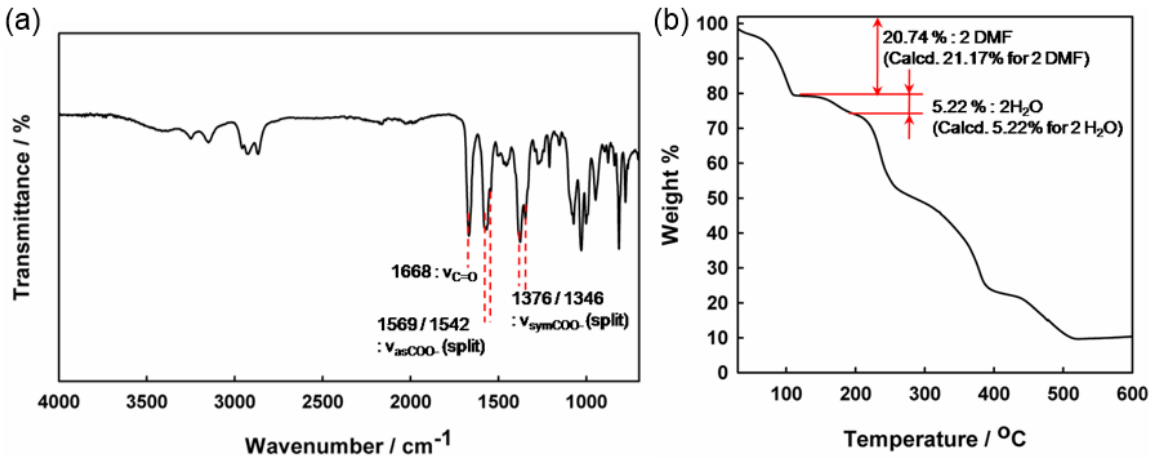


**Figure 3.4.** (a) IR spectrum of **1-as**. (b) TGA trace of **1-as**.

**Table 3.1.** X-ray crystallographic data of **1-as.**

| Compound | ***flex*MOF-DMF (195 K)** |
|---|---|
| formula | $Ni_1C_{22}H_{37}N_6O_4$ |
| crystal system | *Monoclinic* |
| space group | *C*2/*c* |
| fw | 508.28 |
| *a*, Å | 29.788(6) |
| *b*, Å | 11.995(2) |
| *c*, Å | 22.094(4) |
| $\alpha$, deg | 90 |
| $\beta$, deg | 114.76(3) |
| $\gamma$, deg | 90 |
| *V*, Å $^3$ | 7168(3) |
| *Z* | 8 |
| $\rho_{calcd}$, g cm$^{-3}$ | 0.942 |
| temp , K | 195(2) |
| $\lambda$, Å | 0.65002 |
| $\mu$, mm$^{-1}$ | 0.446 |
| goodness-of-fit ($F^2$) | 1.057 |
| *F*(000) | 2168 |
| reflections collected | 30043 |
| independent reflections | 8412 [*R*(int) = 0.0253] |
| completeness to $\theta_{max}$, % | 90.8% |
| data/parameters/restraints | 8412 / 0 / 360 |
| $\theta$ range for data collection, deg | 2.737 to 25.999 |
| diffraction limits (*h*, *k*, *l*) | $-40\leq h\leq 40$, $-16\leq k\leq 16$, $-29\leq l\leq 29$ |
| refinement method | Full-matrix least-squares on $F^2$ |
| $R_1$, $wR_2$ [$I>2\sigma(I)$] | $R_1 = 0.0416^a$, $wR_2 = 0.1308^b$ |
| $R_1$, $wR_2$ (all data) | $R_1 = 0.0426^a$, $wR_2 = 0.1319^b$ |
| largest peak, hole, eÅ $^{-3}$ | 0.478, -0.397 |

$^aR = \Sigma||F_o| - |F_c||/\Sigma|F_o|$. $^bwR(F^2) = [\Sigma w(F_o^2 - F_c^2)^2/\Sigma w(F_o^2)^2]^{1/2}$ where $w = 1/[\sigma^2(F_o^2) + (0.0800P)^2 + (6.0318)P]$, $P = (F_o^2 + 2F_c^2)/3$.

**Flexibility of 1-as upon temperature change.** The structure of **1-as** was slightly expanded upon temperature increase, and this expansion of cell was observed by single crystal X-ray measurements at 100 K, 195 K, and 298 K. The detailed crystallographic information and selected bond length and bond angles are listed in Table 1 and S1 to S10. The obtained cell parameters of framework at each temperature are represented on Table 3.2.

**Table 3.2.** Cell parameters of **1-as** at different temperatures

| *T* (*K*) | *a* (Å ) | *b* (Å ) | *c* (Å ) | *β* (°) | *V* (Å $^3$) |
|---|---|---|---|---|---|
| **100** | 29.857(6) | 11.770(2) | 22.002(4) | 114.78(3) | 7020(3) |
| **195** | 29.788(6) | 11.995(2) | 22.094(4) | 114.76(3) | 7168(3) |
| **298** | 29.537(6) | 12.514(3) | 22.209(4) | 114.76(3) | 7454(3) |

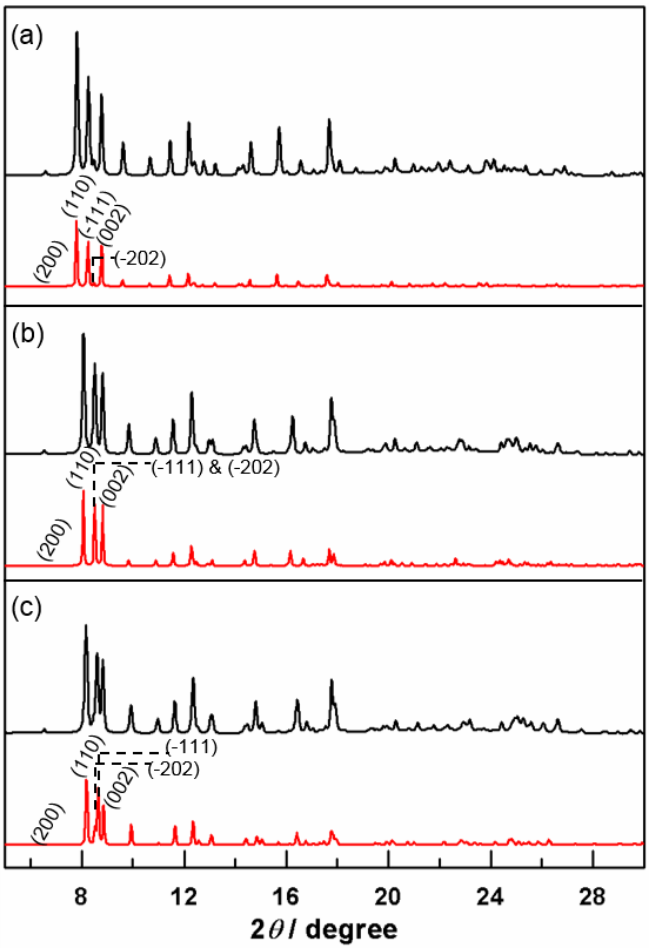


**Figure 3.5.** XRPD patterns (red, simulated patterns; black, measured patterns) of **1-as** (a) at 298 K (b) at 195 K and (c) at 100 K

As temperature increased from 100 K to 298 K, the *b*-axis increased about 0.8 Å but change in *a*- and *c*-axis distance were relatively small (less than 0.3 Å), resulting the expansion of cell volume about 6.2%. It is not large enough to be called "Breathing" upon temperature but enough to bring about the change of XRPD patterns. Thus, main peaks appeared lower than 10° were left shifted as the cell volume expanded, such as the strongest peak, corresponding to (110) plane, was shifted from 8.2° to 7.8° during temperature increased from 100 K to 298 K.

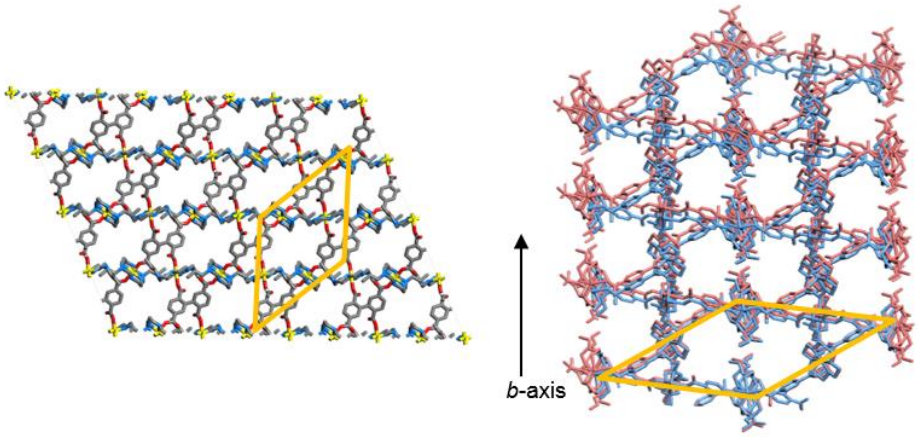


**Figure 3.6.** Overlapped X-ray structures of **1-as** at 100 K (light blue) and at 298 K (pink)

The thermal-induced increase in *b*-axis results from alterations in local structure, such as the change in bond distance, and the rotation of bonds. In particular, the rotation of single bonds in $BPTC^{4-}$ ligand is the important factor because the length in *b*-axis is related to the twisted angles of two phenyl rings, and between phenyl ring and each carboxylate. Additionally, the fact that change in bond length was just 0.01 Å confirms bond rotation is key factor for the expansion of cell volume.

**Table 3.3.** Dihedral angles of $BPTC^{4-}$ of **1-as**.

| ***T* (K)** | **Angle (i) (°)** | **Angle (ii) (°)** | **Angle (iii) (°)** |
|---|---|---|---|
| **100** | 47.342(47) | 67.069(106) | 7.064(68) |
| **195** | 45.843(49) | 66.080(113) | 7.798(72) |
| **298** | 44.232(54) | 65.123(126) | 9.818(83) |

$BPTC^{4-}$ ligand has flexible moieties of freely-rotatable single bonds between two phenyl rings and between phenyl ring and each carboxylate group. The change in angle (i) directly affects *b*-axis, and others, angle (ii) and (iii), gives minor effect to the expansion in *b*-axis direction. Thus, the angle (i)

was expected to increase, however it decreased from 47.34° to 44.26° as temperature increased. It seemed to contradictory to the observed phenomenon, but other dihedral angles it resulted in the opposite effect to the change of angle (i). The angle (ii) decreased by 1.9° and (iii) increased from 7.06° to 8.73° during temperature increase. Their changes gave rise to the extension of *b*-axis because the reduction of angle (ii) and the increase of (iii) make the set of equivalent coordination bonds closer to each other. Therefore, the combination of the whole change in each dihedral angle led to the expansion in *b*-axis.

**Flexibility of 1-as upon guest exchange.** The structural transformation was occurred during the activation of guest molecules. Exchanging the guest molecules with MeCN (linear, smaller and less interactive solvent), the framework was transformed into the structure containing MeCN as guest molecules (**1-MeCN**). After exchanging the guest solvents to MeCN, the whole framework was kept in same state without large change such as crystal system, space group and the connection between metal building blocks and organic linkers. The detailed crystallographic information and selected bond length and angles are listed in Table S11 to S21.

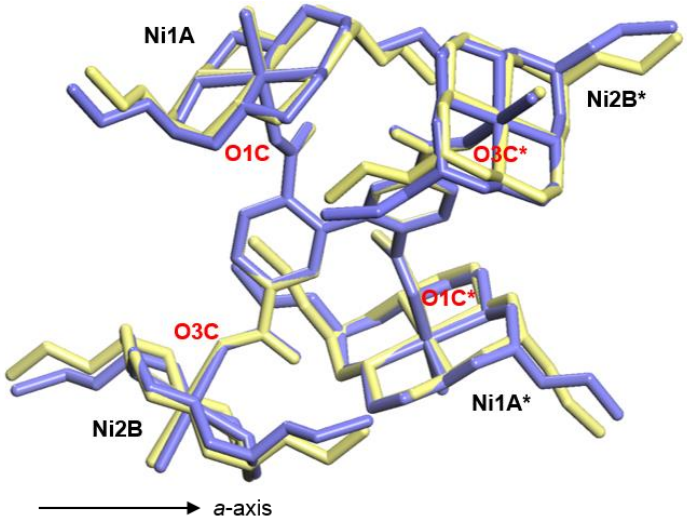


**Figure 3.7.** The overlapped image of local structures of **1-as** (pale yellow) and **1-MeCN** (pale purple), which were collected at 195 K.

**Table 3.4.** Cell parameters of **1-MeCN** at different temperatures

| ***T* (*K*)** | ***a* (Å)** | ***b* (Å)** | ***c* (Å)** | ***β* (°)** | ***V* (Å$^3$)** |
|---|---|---|---|---|---|
| **100** | 29.377(6) | 11.657(2) | 22.227(4) | 114.80(3) | 6909(3) |
| **195** | 29.313(6) | 11.935(2) | 22.254(5) | 114.98(3) | 7057(3) |
| **298** | 29.202(6) | 12.217(2) | 22.261(5) | 115.08(3) | 7193(3) |

**Table 3.5.** Dihedral angles of $BPTC^{4-}$ of **1-MeCN**.

| ***T* (K)** | **Angle (i) (°)** | **Angle (ii) (°)** | **Angle (iii) (°)** |
|---|---|---|---|
| **100** | 43.438(41) | 70.139(79) | 8.585(54) |
| **195** | 43.748(44) | 69.019(92) | 9.642(61) |
| **298** | 44.146(80) | 68.432(184) | 8.948(127) |

**1-MeCN** showed the expansion of cell upon temperature increase either (Table 3.4). However, the local structure was changed and the differences between **1-MeCN** and **1-as** were observed by single crystal X-ray diffraction. Comparing each structure measured at 195 K, the cell volume decreased by 1.55 % mainly due to the reduction of the length in *a*-axis by 0.48 Å. This shrinkage was caused by the rotation of bonds in $BPTC^{4-}$. The change in dihedral angles in $BPTC^{4-}$ were attributed to the decrease of cell volume. First, the decrease in *b* axis arouse from the reduction of the angle (i), but the effect of change in angle (i) was offset by the rotation of carboxylates giving the insignificant decrease in *b*-axis (~0.06 Å). On the other hand, the angle (ii) and (iii) were mainly contributed to decrease in *a*-axis. The phenyl rings of $BPTC^{4-}$ were symmetric to each other, and therefore the one could be generated from the other. The symmetrically generated part is marked by * in Figure 3.7. The increased angle (ii) caused the distance between O1C and O1C* to be shorter because the rotational direction of two carboxylates was symmetric and opposite to each other. The angle (iii) gave rise to similar result. Therefore, the increase of angle (ii) & (iii) brought about the shrinkage in *a*-axis, and the rotation of carboxylates led to the change in orientation of the pendants due to rotation of macrocycles. As a result, the XRPD patterns of **1-MeCN** were different from those of **1-as** at each temperature.

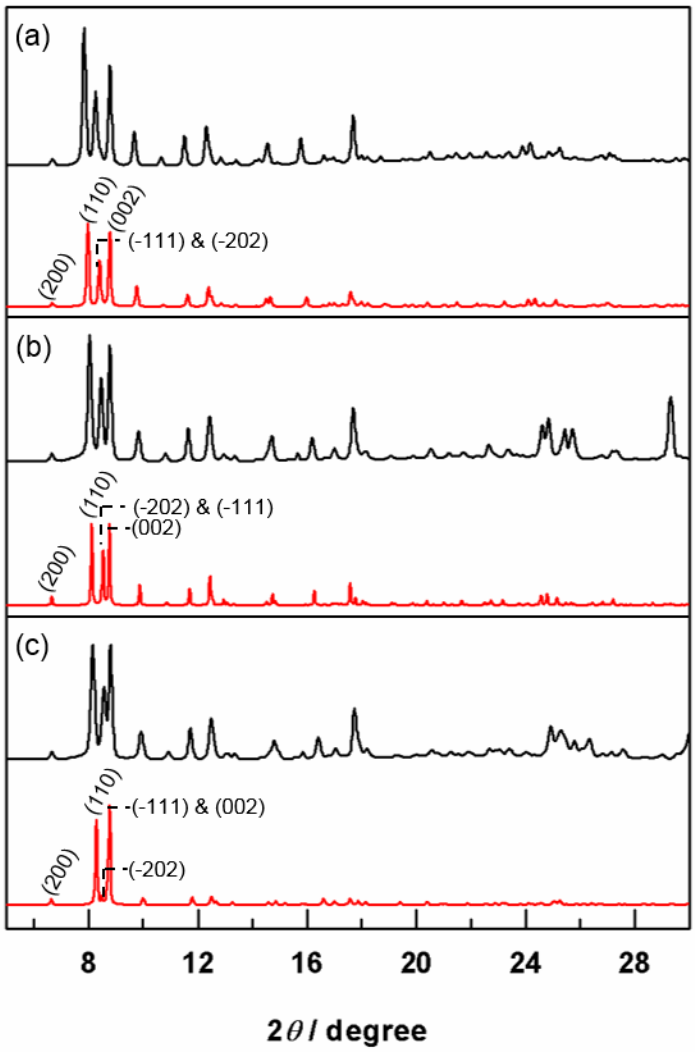


**Figure 3.8.** XRPD patterns of **1-MeCN** at 100 K, 195 K, and 298 K.

**Gas sorption properties of 1.** To prepare the sample, the **1-MeCN** crystals were introduced into the instrument cell and evacuated under vacuum at 110 °C for 4 h. Then the gas sorption behavior of activated sample, **1**, was studied with $N_2$, $H_2$, and $CO_2$. $N_2$ adsorption isotherm showed typical type II sorption behavior, indicating the non-porous nature of **1**, suggesting that the structure of **1** lost the porosity during activation which **1-as** has possessed. Its calculated Brunauer-Emmett-Teller (BET) surface area and total pore volume (7.47 $m^2/g$ and 3.80 x $10^{-2}$ $cm^3/g$, respectively at $p/p_0$ = 0.99) support the suggestion. Thus, it didn't uptake $H_2$ gas at 77 K (7.34 $cm^3/g$) and $CO_2$ gas at 273 K, and 298 K (3.97 wt% and 1.12 wt%, respectively). However, it showed interesting results for $CO_2$ adsorption isotherms at 195 K, it adsorbed 45.6 wt% of $CO_2$ gas with a two-step adsorption profiles as well as a stepwise and hysteretic desorption curve. The abrupt adsorption of $CO_2$ was occurred at 0.16

bar and it indicated that the structure was changed from non-porous to porous, which is called "gate-opening" phenomenon.[18,19]

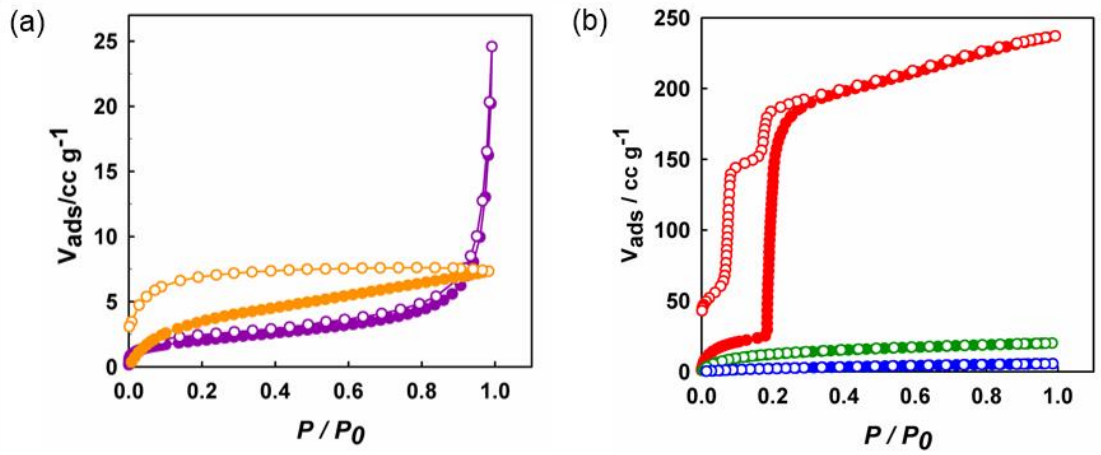


**Figure 3.9.** Gas sorption isotherms of **1** (a) $N_2$ (dark pink) $H_2$ (orange) at 77 K. (b) $CO_2$ at 195 K (red), 273 K (green), and 298 K (blue).

**High pressure gas sorption measurement of 1.** The high pressure gas sorption isotherms of **1** was collected after the activation of the sample through evacuating **1-MeCN** crystals in the instrument cell at 110 $^{o}$C for 4 h. Then, the $CO_2$ gas sorption was measured in pressure range of 0 to 45 bar at 303 K. Its adsorption isotherms showed the two-step profile either with gate-opening pressure at 18 bar, which is much higher than that of 195 K, and desorption curve didn't follow the adsorption curve with large hysteresis and with two-step at a lower pressure, about 15 bar. In addition, the adsorbed amount of $CO_2$ was 28.5 wt% at 45 bar, which was much smaller than the amount of adsorption at 195 K and 1 atm. The reason why the gate-opening pressure increased as the temperature increased has been explained by the rate at which the gas molecules strike the solid surface.[26]

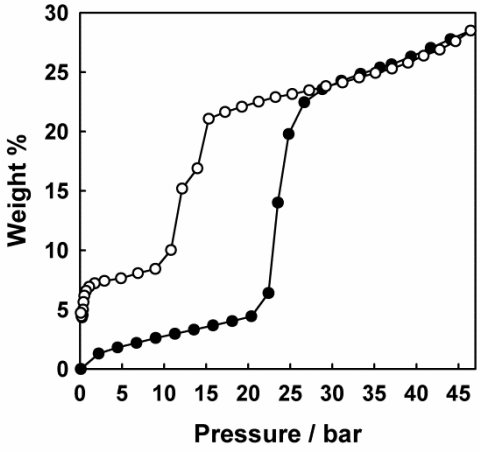


**Figure 3.10.** High pressure $CO_2$ gas sorption isotherm of **1** at 303 K.

***In-situ* XRPD experiments for 1 during $CO_2$ sorption.** In order to investigate the stepwise adsorption behavior of **1**, we conducted in-situ XRPD measurements during $CO_2$ sorption at 195 K and 298 K. **1-MeCN** was dried at 70 $^oC$ for 1 h under vacuum condition, finely ground, and packed in the capillary under Ar in the glove box. Then, the sample was completely dried by evacuating the capillary with heating at 110 $^oC$ about 15 min, and cooled down to 195 K and 298 K, respectively. The XRPD patterns of activated compound, **1**, showed the large difference from those of **1-as** and **1-MeCN** at each temperature, but the XRPD patterns of **1** were same regardless of temperature (at 195 K and 298 K).

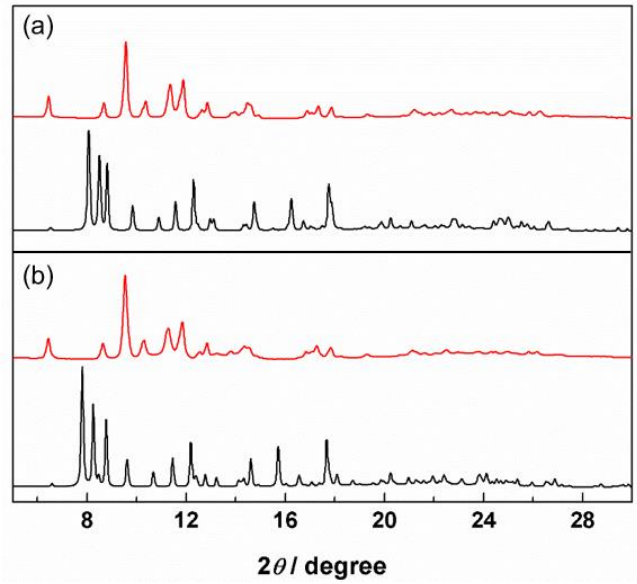


**Figure 3.11.** XRPD patterns of **1-as** (black), and **1** (red) (a) at 195 K, and (b) at 298 K.

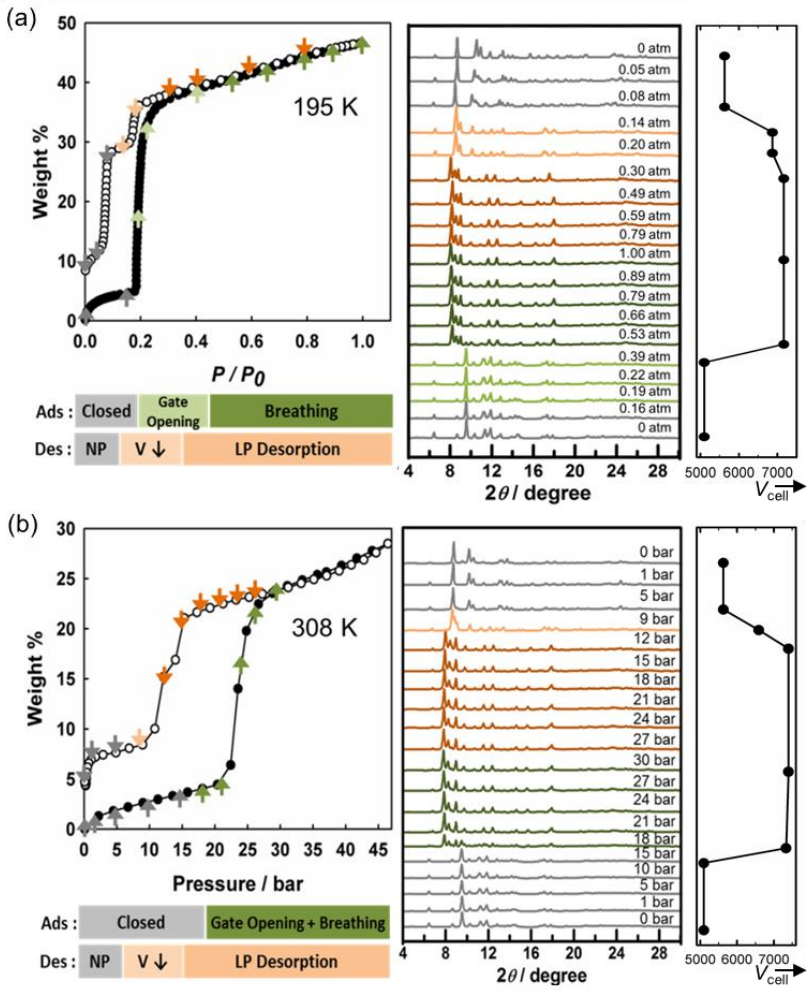


**Figure 3.12.** *In-situ* experimental results of **1** (a) at 195 K and (b) at 298 K.

Predicting the result of experiment at 195 K, the change in XRPD patterns would be expected to appear in the range of 0.16 to 0.19 atm where the abrupt $CO_2$ uptake occurred. Surprisingly, the patterns kept almost same until 0.4 bar, and the drastic change was observed from 0.4 to 0.53 atm, and the completely changed XRPD patterns after 0.53 atm were same as that of as-synthesized compound (**1-as**). In contrast, XRPD patterns were changed at each step of the desorption isotherm, therefore the shrinkage of frameworks occurred step by step causing stepwise desorption profile. The reason for stepwise shrinkage of framework could be explained by the constraint on change of framework by guest molecules filled within the pore.

The unexpected result of experiment at 195 K suggested that the structural transformation during $CO_2$ uptake would be two-kind of change: gate-opening and breathing, and these changes were occurred sequentially. At the pressure of 0.16 to 0.19 atm, the closed pore was open without

expansion of cell volume, that is, gate-opening was occurred. After that, the framework was expanded as pressure increased up to 0.4 atm, which is corresponded to breathing phenomenon, bringing about the change in XRPD patterns. As a result of this sequential structural transformation, the behavior of **1** during adsorption of $CO_2$ at 195 K into three different phases: (1) Closed (~ 0.16 bar) (2) Gate-opening (0.16 ~ 0.4 bar), and (3) Breathing (0.4 bar ~). The XRPD patterns collected at 298 K during $CO_2$ sorption in the range of 0 to 30 bar showed similar trend to the result of 195 K, but the change in patterns was occurred at near the gate-opening pressure. This indicates that gate-opening and breathing took place simultaneously at ambient temperature, and the resulting structure after $CO_2$ adsorption was similar to the as-synthesized structure at 298 K, comparing with XRPD patterns of two. Additionally, the cell volumes at each pressure point adsorption were calculated from the measured XRPD patterns and the single crystal structures whose simulated patterns corresponded to the patterns with $CO_2$ pressure. The resulting plots were represented at Figure 3.12.

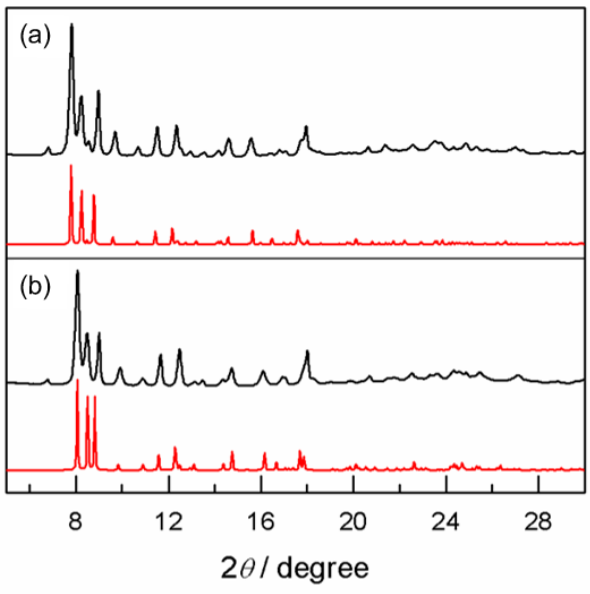


**Figure 3.13.** Comparison of XRPD patterns of **1-as** (simulated, red) with **1** adsorbing $CO_2$ molecules (**1⊃CO₂**) (black) (a) at 30 bar and 298 K, and (b) at 1 atm and 195 K, respectively.

**Structural transformation during gas adsorption.** We tried to measure the single crystal X-ray diffraction to observe the structural difference, but we couldn't get the X-ray crystal information of **1** since the activated sample lost the single crystallinity. Thus, the structure of **1⊃CO₂** couldn't be collected either. However, we could get the structure of the partially dried sample (**1'**), which could be used to estimate the structure of **1**, and **1-as** is able to suggest the structure of **1⊃CO₂** at 195 K and 1

atm since their XRPD patterns were almost same (Figure 3.13).

The structure of **1'** has triclinic system with *P*-1 space group and the drastic decrease of cell volume to 5628.4 Å$^3$ at 195 K due to the smaller twisted angle of two phenyl rings of $BPTC^{4-}$ in **1'** (43.616(176)$^o$). Originally, its cell volume is 2814.2 Å$^3$ but it contains half of molecules than **1-as** has, because of change in space group. Thus, we would consider the cell volume of **1'** as 5628.4 Å$^3$ for easy comparison. The detailed crystallographic information and selected bond length and angles are listed in Table S18 and S22 to S24.

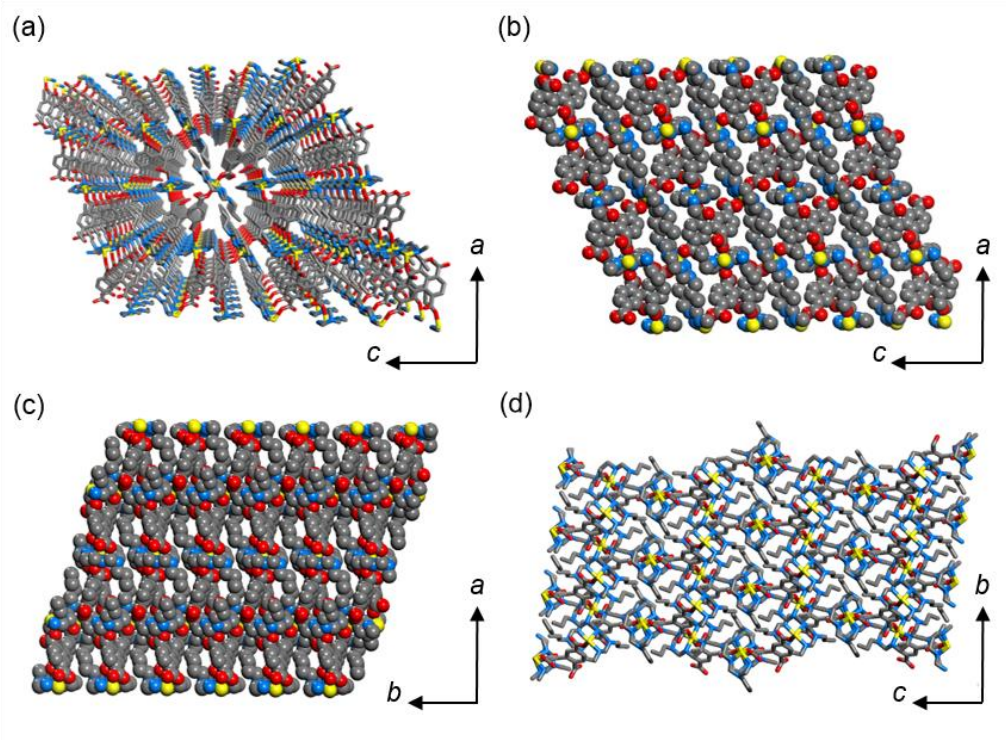


**Figure 3.14.** The structure of **1'** measured at 195 K (a) A perspective view on *ac* plane. (b) A CPK view on a*c* plane. (c) A CPK view on *ab* plane. (d) A view on *bc* plane (Ni, yellow; C, gray; N, blue; O, red)

Predicting the result of experiment at 195 K, the change in XRPD patterns would be expected to appear in the range of 0.16 to 0.19 atm where the abrupt $CO_2$ uptake occurred. Surprisingly, the patterns kept almost same until 0.4 bar, and the drastic change was observed from 0.4 to 0.53 atm, and the completely changed XRPD patterns after 0.53 atm were same as that of as-synthesized compound (**1-as**). In contrast, XRPD patterns were changed at each step of the desorption isotherm, therefore the shrinkage of frameworks occurred step by step causing stepwise desorption profile. The reason for

stepwise shrinkage of framework could be explained by the constraint on change of framework by guest molecules filled within the pore. Additionally, because all Ni(II) macrocyclic complexes have different orientations, the structure contains crystallographically independent four kinds of Ni(II) macrocycles, Ni1A, Ni2B, Ni3C, and Ni4D which were matched to those of Ni1A*, Ni2B*, Ni1A, and Ni2B, respectively (Figure 3.16; *: symmetrically generated ones). One of them (Ni1A) has disordered pendant arms but the only one part is considered for clear analysis. Each axial position of macrocyclic complexes is bonded with oxygens from carboxylate anions of $BPTC^{4-}$ ligands in mondentate fashion with average Ni-O distance of 2.138(2) Å. Furthermore, every non-coordinating oxygen of carboxylate makes hydrogen bond with one of N-H of the macrocycle (N1A···O2E 2.836(6) Å, ∠N1A-H1A···O2E 150.4°; N2B···O4E 2.944(6) Å, ∠N2B-H2B···O4E 151.7°; N2C···O6E 2.878(6) Å, ∠N2C-H2C···O6E 151.8°; N2D···O8E 2.888(6) Å, ∠N2D-H2D···O8E 153.3°). Unlikely to **1-as**, only one of four carboxylate groups, O4E, additionally bonds to N-H of another macrocyclic complex of Ni3C (N1C···O4E 2.998(7) Å, ∠N1C-H1C···O4E 130.1°). As suggested from the different hydrogen bonds, orientations of pendant groups of macrocyclic complexes are changed and blocked the pore of **1'** shown like Figure 3.14.

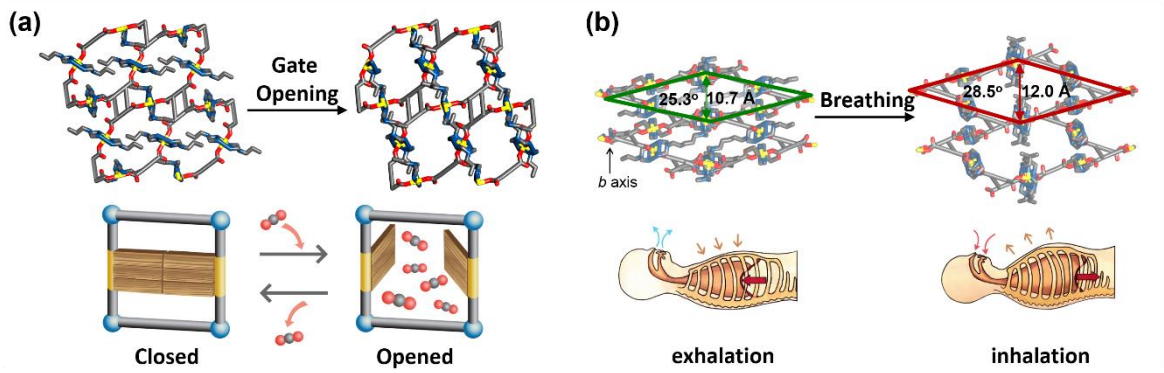


**Figure 3.15.** Schematic view of structural transformation of **1** during $CO_2$ gas uptake.

To observe the structural transformation during $CO_2$ gas sorption, we compared **1'** and **1-as** as the structure before and after $CO_2$ adsorption, respectively. As a result of comparison, the gate-opening arouse from the rotation of macrocycles, whose pendant arms acted as the gate of the pore. On the other hand, the breathing effect resulted from the changes in $BPTC^{4-}$, whose freely rotatable bonds gave rise to the expansion of *b*-axis and *ac* plane. The schematic image of these changes is represented on Figure 3.15. The fundamental unit of two structures was divided into four part matched with Ni1A, Ni2B, Ni3C, and Ni4D, respectively. Due to difference in the asymmetric unit, each part was labeled with I, II, III, and IV like Figure 3.16.

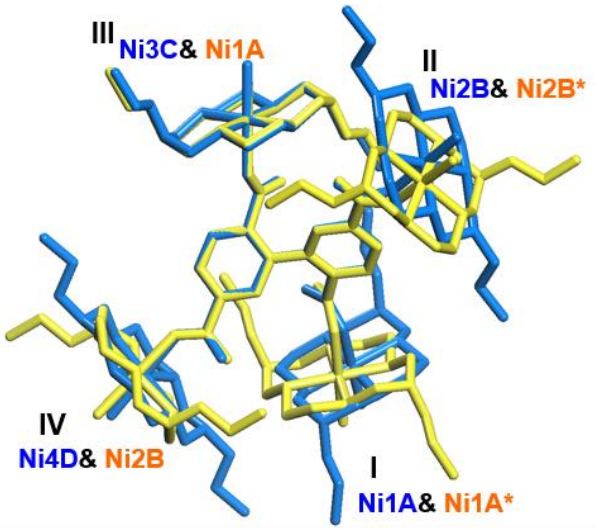


**Figure 3.16.** Overlapped image of local structures for **1** before (**1'**; blue) and after (**1-as**; yellow) $CO_2$ gas uptake.

Analyzing the structural change in details for gate-opening first, three macrocycles in part I, II, and IV were rotated during adsorption of $CO_2$ gas with reconstruction of hydrogen bonds between amine in macrocycle and not coordinated oxygen from carboxylate (Table 3.6, Figure 3.17). For the part I, carboxylate was bonded to N1A, but it was changed to N2A, and the additional hydrogen bond was formed for N1A with carboxylate of part IV. Similarly, the hydrogen bonds were changed from nitrogen labeled with N2B and N2D to N1B & N1D without making additional hydrogen bond at part II and IV. However, unlike other macrocyclic complexes the macrocycle at part III wasn't rotated without reconstruction of hydrogen bonds. This is because the macrocycle at part III was bonded with two different carboxylates from part III and II before adsorption. This two hydrogen bonds apply energy to $[NiL_{propyl}]^{2+}$ about 78.4 kcal/mol, which is much larger than that applied to others at I, II, and IV (averagely, 43.0 kcal/mol). By the way, the reason for the irreversible structural transformation during the $CO_2$ sorption of **1** seemed to be the formation of additional hydrogen bond on macrocycle in part I. This new hydrogen bond reduced the opportunity of rotation due to increase of energy barriers for transformation, and it was not enough to overcome through interaction energy of $CO_2$.

**Table 3.6.** Changes in hydrogen bonds of macrocycles at each part upon $CO_2$ gas adsorption.

| | | Before sorption | After sorption |
|---|---|---|---|
| I | **H-bonded N label** | 1 | 2 |
| | **N···O** | 2.836(6) Å | 2.860(2) Å |
| | **∠N-H···O** | 150.4° | 152.3° |
| | **Additional H-bond** | - | N1···O4 2.978(2) Å<br>∠N1-H1···O4 131.2° |
| II | **H-bonded N label** | 2 | 1 |
| | **N···O** | 2.944(6) Å | 2.938(2) Å |
| | **∠N-H···O** | 151.7° | 151.5° |
| | **Additional H-bond** | - | - |
| III | **H-bonded N label** | 2 | 2 |
| | **N···O** | 2.878(6) Å | 2.859(2) Å |
| | **∠N-H···O** | 151.8° | 152.3° |
| | **Additional H-bond** | N1···O4 2.998(7) Å<br>∠N1-H1···O4 130.1° | N1···O4 2.978(2) Å<br>∠N1-H1···O4 131.2° |
| IV | **H-bonded N label** | 2 | 1 |
| | **N···O** | 2.888(6) Å | 2.938(2) Å |
| | **∠N-H···O** | 153.3° | 151.5° |
| | **Additional H-bond** | - | - |

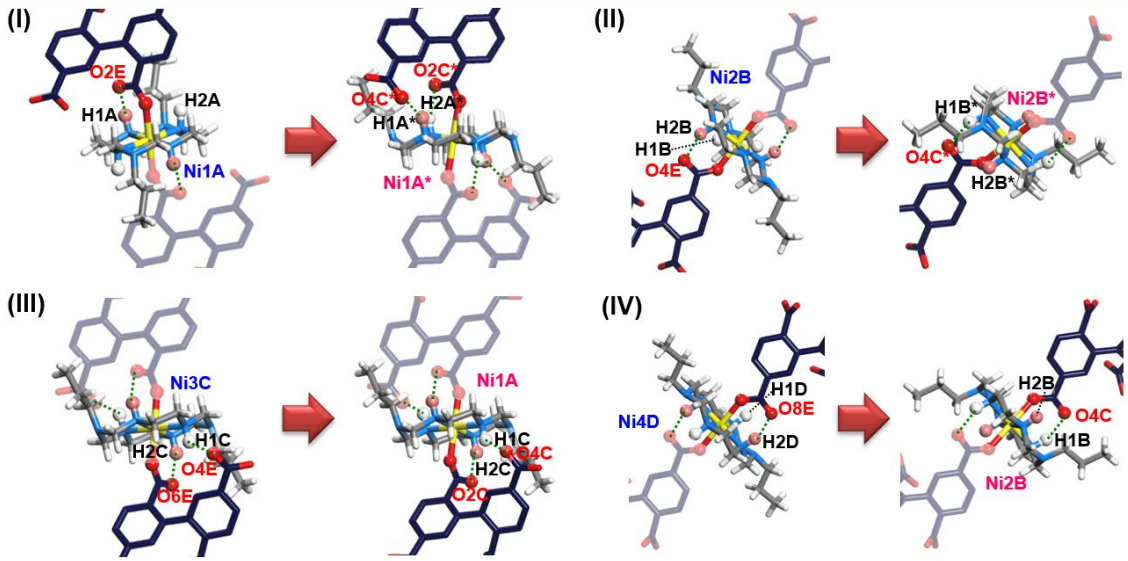


**Figure 3.17.** Breaking and reconstruction of H-bond by rotation of macrocycles at each part.

On the contrary, the breathing behaviors was induced mostly by the change in dihedral angle between two phenyl rings (angle ①). It was increased from 43.616(176)° to 45.843(49)° during uptake of $CO_2$ gas molecules, resulting in the increase in *b*-axis. Additionally, the change in the angles between carboxylate groups and phenyl rings (②,③,④, and ⑤) gave minor contribution to the breathing behavior. Furthermore, the expansion of pore wall on *ac* plane was observed as a result of breathing event. Considering the difference in crystal systems of two structures before and after $CO_2$ gas sorption, we transformed the cell parameters of **1′** to new parameters represented in Table 3.7 based on **1-as** structure. Comparing two structures, the reduction in *a*-axis direction and the increase of *c*-axis were occurred during $CO_2$ adsorption. As a result, the distance between two nickels located at the diagonals represented on Figure 3.15 (b) increased from 10.7 Å to 12.0 Å. This increased aperture size of pore on *ac* plane was attributed to changes in twisted angles ②,③,④, and ⑤ (Figure 3.15 (b)). Consequently, the rotations of single bonds in $BPTC^{4-}$ ligand leaded to the breathing behavior of **1** during the $CO_2$ gas sorption, leading to the increase of cell volume (5628 $Å^3$ to 7168 $Å^3$).

**Table 3.7.** Comparison of cell parameters of the structure before adsorption, **1'** (transformed based on the **1-as** system), and after adsorption, **1-as**.

| | ***a*** | ***b*** | ***c*** | ***V*** |
|---|---|---|---|---|
| **Before sorption** | 32.334 | 9.1860 | 21.820 | 5628 |
| **After sorption** | 29.788 | 11.995 | 22.096 | 7168 |

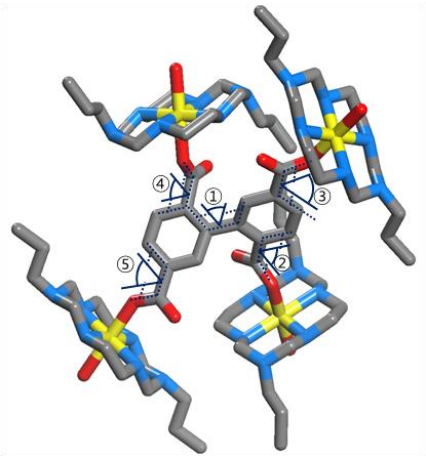


**Figure 3.18.** Angles in $BPTC^{4-}$ of **1'**.

**Table 3.8.** Changes in dihedral angles of $BPTC^{4-}$ upon $CO_2$ gas adsorption.

| | **Before sorption** | **After sorption** |
|---|---|---|
| ① | 43.616(176)° | 45.843(49)° |
| ② | 45.226(415)° | 66.080(113)° |
| ③ | 12.293(416)° | 7.798(72)° |
| ④ | 69.547(467)° | 66.080(113)° |
| ⑤ | 19.347(926)° | 7.798(72)° |

**Gas adsorption behavior studies on structural view.** For the structural transformation of **1** during $CO_2$ uptake at 195 K, it was indicated that the gate-opening was occurred independently to breathing through the gas sorption isotherms and *in-situ* XRPD experiment. That is, the abrupt increase in $CO_2$ adsorption at 195 K was attributed only to the gate-opening, not to cell expansion. It suggested that the rotation of macrocycle could generate the void that can accommodate 39.0 wt% of $CO_2$. For this reason, we calculated how many $CO_2$ molecules can reside in the void of each structure, **1'** and **1-as**, on minimum energy state at 195 K. In addition, we assumed that the void volume of dried structure wouldn't be changed until 0.4 atm. That is, the phase of **1** would be changed once in the view of change of void volume.

**Table. 3.9.** Calculation results for the possible number of $CO_2$ in void space of each structure

| | Unit cell volume (Å$^3$) | Void volume (Å$^3$) | # of $CO_2$ in void | $CO_2$ wt% in void |
|---|---|---|---|---|
| **1-as** | 7168 | 2878.6 | 55.51 | 60.08 |
| **1'** | 5628 | 909.4 | 20.00 | 21.64 |

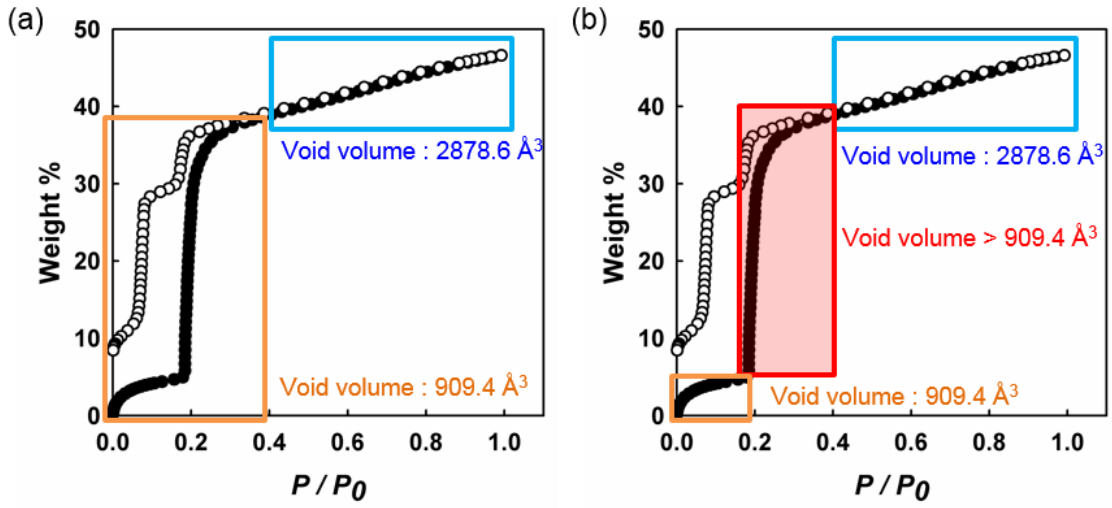


**Figure 3.19.** Assumptions for $CO_2$ sorption isotherms in the point of change in void space (a) isotherms of two phases. (b) isotherms of three phases.

The structure of **1-as**, which is same as the structure of **1⊃CO₂**, has 7168 Å$^3$ of cell volume is and 40.2% void space (2878.6 Å$^3$). It indicates that this MOF can contain 60.08 wt% of $CO_2$, corresponded to 55.51 $CO_2$ molecules, after finishing structural transformation. On the other hand, **1'**

has 5628 Å$^3$ of cell volume and 16.3% of cell volume is void volume (909.4 Å$^3$), which can contain 20.00 $CO_2$ molecules. That is, the dried structure has the potential to adsorb 21.64 wt% of $CO_2$ unless the pore is blocked. The void space of **1-as** is 3.16 times larger than void of **1'**, which is good agreement with the fact that **1-as** can accommodate 2.78 times of $CO_2$ than **1'**. However, the value of 21.64 wt% is too small to explain the abrupt increase from 0.16 atm to 0.4 atm, since the adsorbed amount of $CO_2$ has increased up to 39.0 wt% at 0.4 atm. However, the actual void volume of structure after gate-opening occurs would be considered larger than that of dried state because the different orientations for pendants groups of Ni (II) macrocycles could give larger accessible space for $CO_2$ gas molecules. Thus, it is possible that the abrupt increase of adsorption amount up to 39 wt% only through the gate-opening process.

**X-ray structure of 2-as and 3-as.** To construct the guest-responsive coordination polymers, we employed a flexible aliphatic ligand, $H_4$BuTC and Ni (II) macrocyclic complex with two allyl pendant arms presenting in a square planar geometry, $[NiL_{allyl}]^{2+}$. The self-assembly reaction of $[NiL_{allyl}]^{2+}$ and $BuTC^{4-}$ in DEF and $H_2O$ mixture solution and in MeCN and $H_2O$ mixture solution yield pale purple crystals and powders of $\{[(NiL_{allyl})_2(BuTC)]\cdot 2DEF\cdot 2H_2O\}$ (**2-as**) and $\{[(NiL_{allyl})_2(BuTC)]\cdot 3H_2O\}$ (**3-as**), respectively.

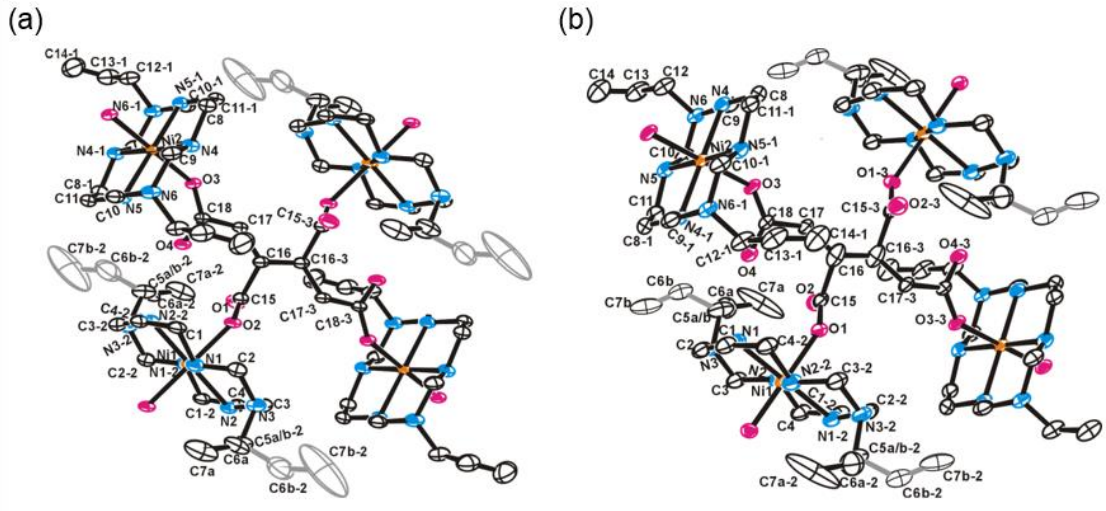


**Figure 3.20.** ORTEP drawings of (a) **2-as**, and (b) **3-as** at 100 K with an atomic numbering scheme (thermal ellipsoids at 30% probability). Symmetry transformations used to generate equivalent atoms: 1,-x+1,-y-1,-z 2, -x,-y,-z 3,-x,-y-1,-z.

The fundamental building unit of **2-as** and **3-as** are shown in Figure 3.20, and both structures have the same fundamental building unit. The unit was assembled via coordination bonds between carboxylates of $BuTC^{4-}$ and $[NiL_{allyl}]^{2+}$, resulting in six-coordinated octahedral Ni (II) center. The unit contains two crystallographically independent Ni (II) macrocycles, which are coordinated with the carboxylate groups located on two different environments, 1 and 4 *versus* 2 and 3 positions on the butane chain of 1,2,3,4-$BuTC^{4-}$ ligand. In both structures, the allyl pendant arms of macrocycles coordinated with the carboxylates on 2 and 3 positions of the butane backbone show the disorderness in the structure (0.57:0.43 for **2-as** and 0.52:0.48 for **3-as**). The axial positions of $[NiL_{ally}]^{2+}$ are occupied by carboxylate anions from two different $BuTC^{4-}$ in monodentate fashion with the average Ni-O distance of 2.105(2) Å for **2-as**, and 2.108(2) Å for **3-as**. In addition, the infinite coordination between macrocycles and $BuTC^{4-}$, stretched along four different directions, generates the 2D layer (*ab* plane) composed of rectangular compartment in each structure. Although the conformation of $BuTC^{4-}$ ligand in **3-as** is slightly different from that in **2-as** in respect of the tilted angle of 2,3-carboxylate groups due to the flexibility of the aliphatic chain of $BuTC^{4-}$, both have almost same layer structure.

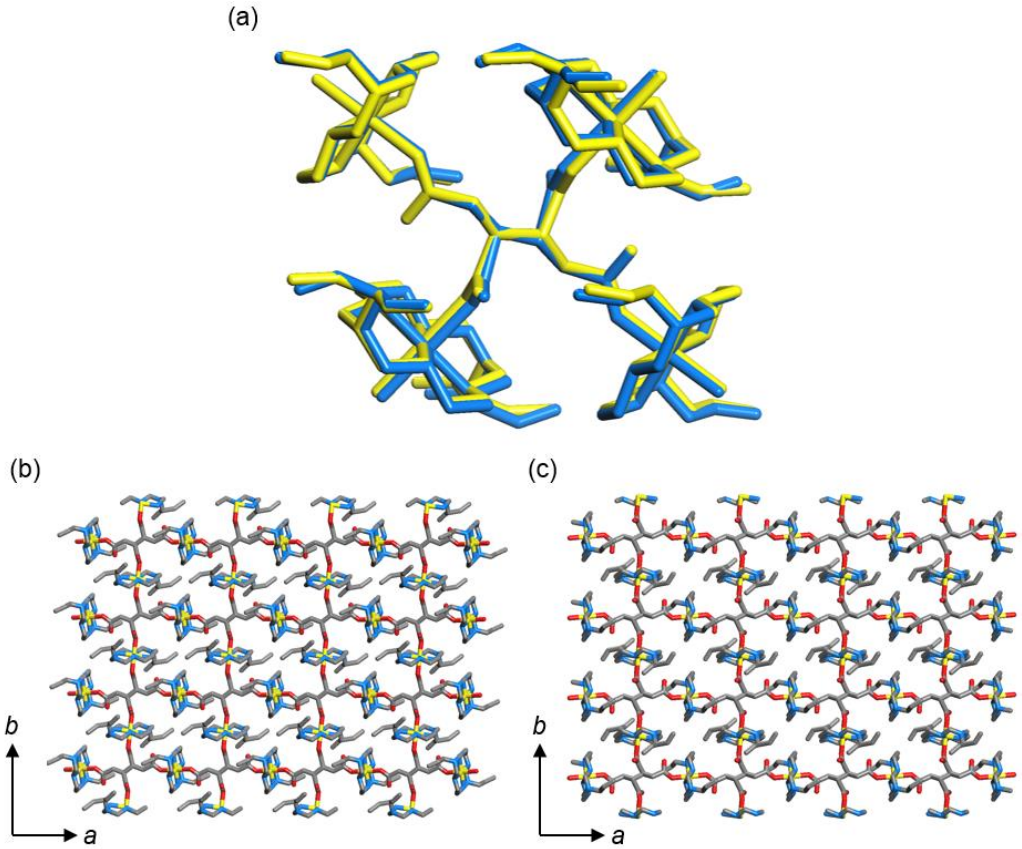


**Figure 3.21.** (a) The overlapped image of fundamental building unit of **2-as** (yellow) and **3-as** (light blue). (b) A view onto *ab*-layer of **2-as**. (c) A view onto *ab*-layer of **3-as**.

While the composition of the reaction solvents mixtures does not affect to the local structure on each layer, it greatly affects the infinite structure made by stacking of the 2D layers in both coordination polymers. In addition, the guest molecules, two DEF and two water molecules for **2-as** and three water molecules for **3-as** per formula, are intercalated between the layers and affect the layer-layer distance and the stacked manner. Because of the bulkiness of DEF molecules, the layer-layer distance in **2-as** (12.96 Å) is much larger than that in **3-as** (9.47 Å) as shown in Figure 3.22. Coordination polymer **2-as** possesses the triclinic system with space group *P*-1, whereas **3-as** is crystallized in monoclinic system with the space group *P*2/*c*. In the coordination polymer **2-as**, equivalent layers are stacked in the ···A-A-A··· manner (Figure 3.22. (a)). However, in the coordination polymer **3-as**, due to the existence of a two-fold screw axis between the layers, two different kinds of layers are packed alternatively through the *c* axis in the ···A-B-A-B··· fashion (Figure 3.22. (b)).

Despite the high boiling point of DEF molecules, those are easily liberated from **2-as** at a relatively low temperature (~100 °C), which might be attributed to the week molecular interaction between the guest molecules and the host framework. For that reason, even under the careful treatment of the crystal, disordered DEF molecules were not refined properly in the X-ray structure of **2-as**, and thus the data was necessarily squeezed. Therefore, the guest molecules, DEF, are evidenced by IR, elemental analyses and TGA. Since the guest water molecules in **2-as** and **3-as** are located close to the secondary amine group of the macrocycles with very strong hydrogen bonds (N4···OW1 3.015(5) Å and N4—H4···OW1 148.6° for **2-as**; N5···OW1 2.968(13) Å and N5—H5···OW1 148.9° for **3-as**), those were confirmed by single crystal X-ray crystallography. Detailed single crystal X-ray crystallographic information and selected bond lengths and bond angles for **2-as** and **3-as** are listed in Table 3.10 and S26 to S27.

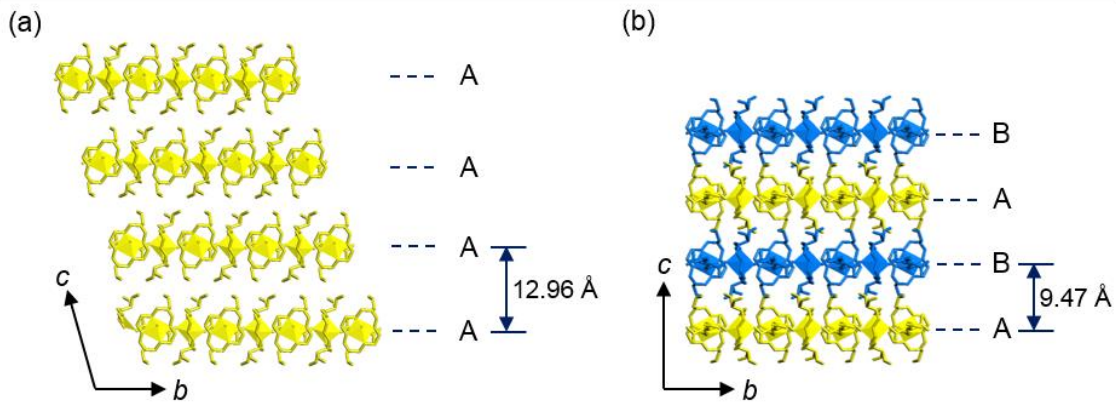


**Figure 3.22.** The stacking of the 2D layers for (a) **2-as** and (b) **3-as**. Six coordinated Ni (II) center was described as an octahedron.

**Table 3.10**. X-ray crystallographic data of **2-as** and **3-as**.

| Compound | **2-as** | **3-as** |
|---|---|---|
| formula | $Ni_1C_{18}H_{35}N_6O_5$ | $Ni_2C_{36}H_{68}N_{12}O_{10}$ |
| crystal system | *Triclinic* | *Monoclinic* |
| space group | *P-1* | *P2/c* |
| fw | 474.23 | 946.44 |
| *a*, Å | 12.276(3) | 12.243(2) |
| *b*, Å | 9.7320(19) | 9.5530(19) |
| *c*, Å | 12.961(3) | 18.947(4) |
| $\alpha$, deg | 106.74(3) | 90 |
| $\beta$, deg | 76.14(3) | 101.88(3) |
| $\gamma$, deg | 86.62(3) | 90 |
| *V*, Å $^3$ | 1426.0(5) | 2168.5(7) |
| *Z* | 2 | 2 |
| $\rho_{calcd}$, g cm$^{-3}$ | 1.104 | 1.449 |
| temp , K | 100(2) | 100(2) |
| $\lambda$, Å | 0.74999 | 0.75002 |
| $\mu$, mm$^{-1}$ | 0.781 | 1.028 |
| goodness-of-fit ($F^2$) | 1.107 | 1.101 |
| *F*(000) | 506 | 1008 |
| reflections collected | 7882 | 17306 |
| independent reflections | 3991 [*R*(int) = 0.0150] | 4754 [*R*(int) = 0.0280] |
| completeness to $\theta_{max}$, % | 93.4% | 96.8% |
| data/parameters/restraints | 3991 / 294 / 4 | 4754 / 294 / 6 |
| $\theta$ range for data collection, | 2.88 to 25.00 | 1.79 to 29.00 |
| diffraction limits (*h*, *k*, *l*) | $-13 \le h \le 13$, $-10 \le k \le 10$, $-14 \le l \le 14$ | $-15 \le h \le 15$, $-12 \le k \le 12$, $-24 \le l \le 24$ |
| refinement method | Full-matrix least-squares on $F^2$ | Full-matrix least-squares on $F^2$ |
| $R_1$, $wR_2$ [$I>2\sigma(I)$] | $R_1$ = 0.0684,[a] $wR_2$ = 0.2033[b] | $R_1$ = 0.0812,[a] $wR_2$ = 0.2411[c] |
| $R_1$, $wR_2$ (all data) | $R_1$ = 0.0758,[a] $wR_2$ = 0.2101[b] | $R_1$ = 0.0988,[a] $wR_2$ = 0.2570[c] |
| largest peak, hole, eÅ $^{-3}$ | 0.750, -0.763 | 1.484, -0.889 |

[a] $R = \Sigma||F_O| - |F_C||/\Sigma|F_O|$. [b] $wR(F^2) = [\Sigma w(F_O^2 - F_C^2)^2/\Sigma w(F_O^2)^2]^{1/2}$ where $w = 1/[\sigma^2(F_O^2) + (0.1940P)^2 + (1.73)P]$, $P = (F_O^2 + 2F_C^2)/3$. [c] $wR(F^2) = [\Sigma w(F_O^2 - F_C^2)^2/\Sigma w(F_O^2)^2]^{1/2}$ where $w = 1/[\sigma^2(F_O^2) + (0.2000P)^2 + (0.0000)P]$, $P = (F_O^2 + 2F_C^2)/3$.

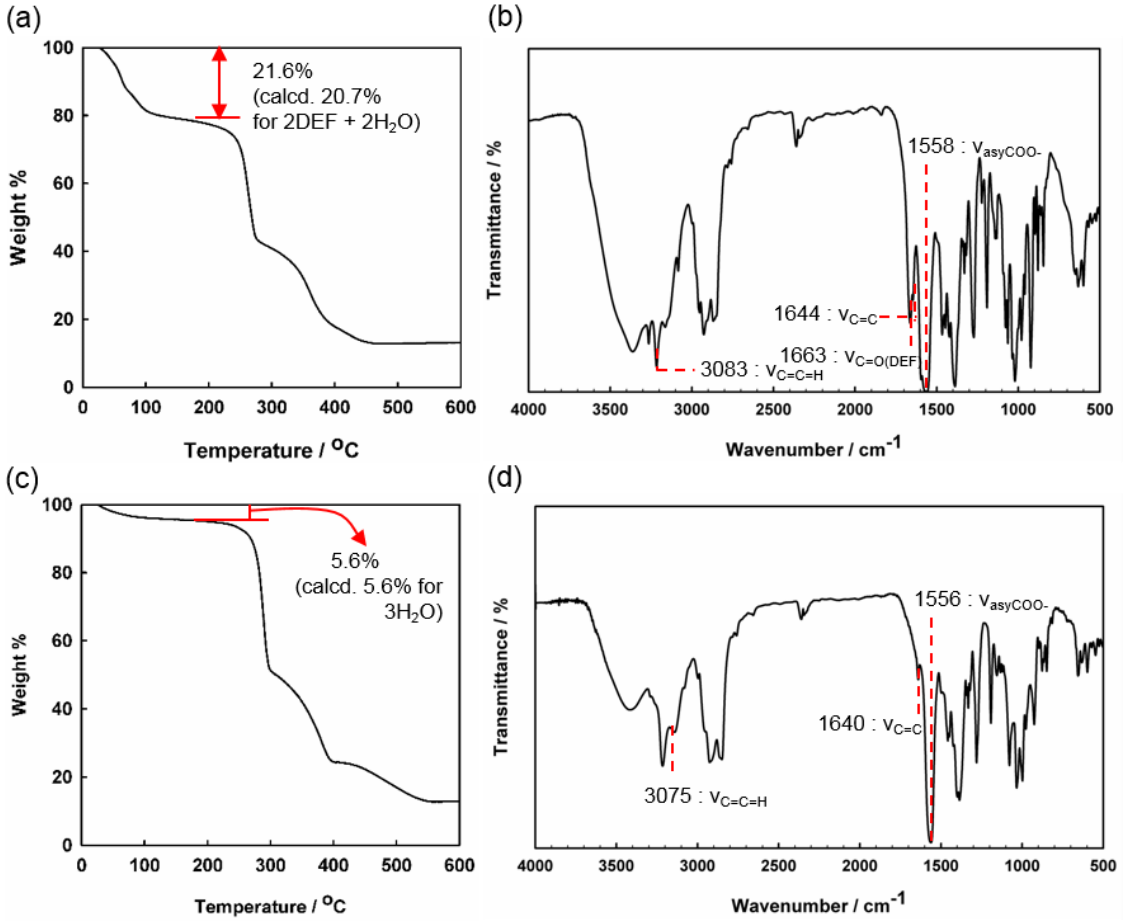


**Figure 3.23.** IR spectra and TGA traces of **2-as** ((a) and (b)) and **3-as** ((c) and (d))

**Structural transformation of 2-as.** To examine structural changes in compounds driven by the removal of guest molecules, both compounds **2-as** and **3-as** were dried by heating at 100 °C under vacuum for 7 h, generating the dried compounds **2** and **3**, respectively. The structural diversities in **2** and **3** were proved by the XRPD patterns. The measured XRPD pattern for **2-as** shows good agreement with the simulated pattern based on the single crystal X-ray diffraction data except for $2\theta$ = 9.76, 11.9, 14.7, 16.1° peaks (Figure 3.24 (a)). The mismatched peaks of **2-as** agree with the peaks from the XRPD pattern of dried compound **2**. Those mismatched peaks might have been generated during the sample preparation and data collection, and those peaks slightly appeared even in the measurement of the wet sample in mother liquor with a faster scan rate (Figure 3.24 (c)). Consequently, they are attributed to the instability of the DEF molecules in structure **2-as**, and DEF molecules were rapidly removed from the interlayer spaces, resulting in the coexistence of the dried structure **2** with the original structure **2-as**. On the other hand, XRPD pattern of **3-as** exhibits the same pattern as that of the **3** as well as that from the simulated data (Figure 3.24 (b)).

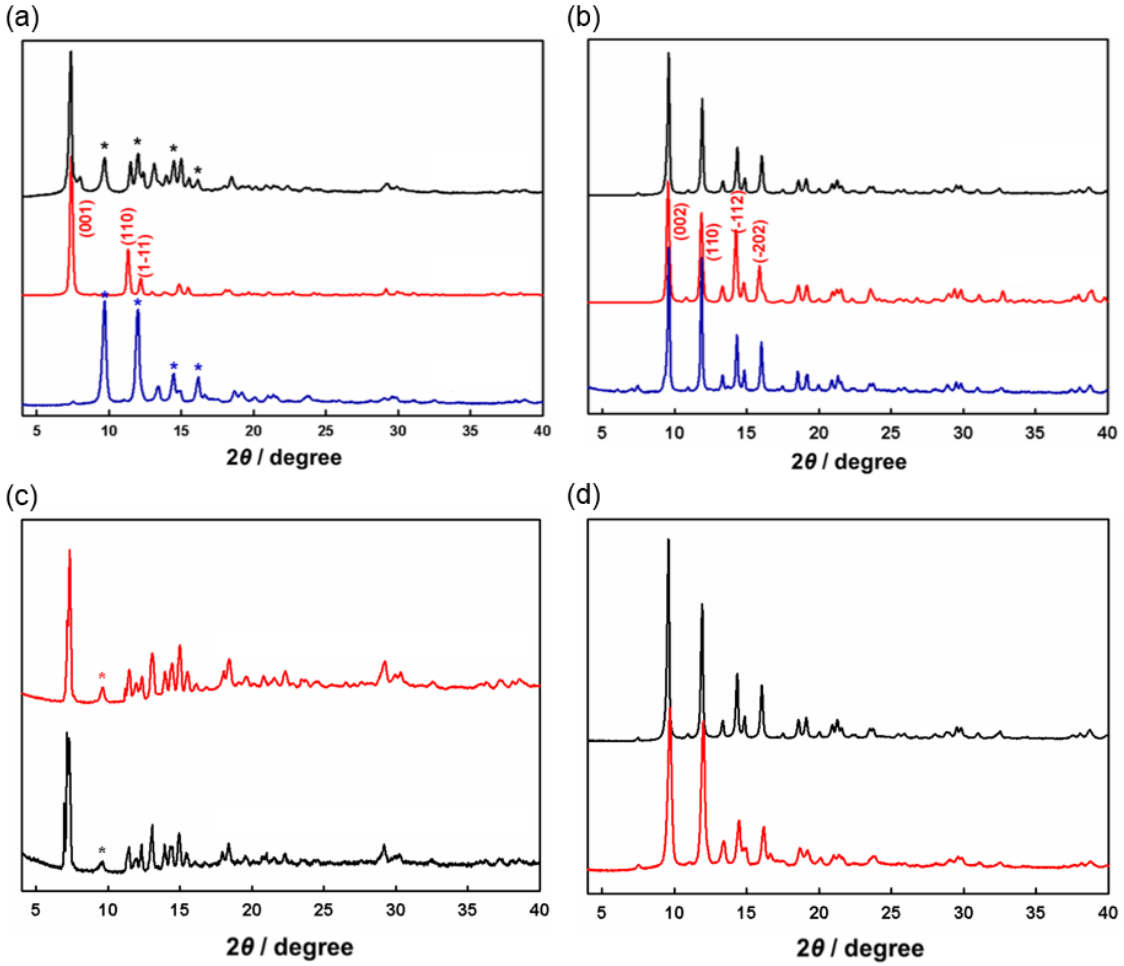


**Figure 3.24.** XRPD patterns of (a) **2-as** (black), simulated pattern of **2-as** (red), and **2** (blue). (b) **3-as** (black), simulated pattern of **3-as** (red) and **3** (blue). (c) XRPD patterns of **2-as** with faster scan rate (0.5 s/step, red; 0.2 s/step, black). (d) Comparison of XRPD patterns of **2** (red) and **3-as** (black).

Interestingly, **2** showed the same pattern as **3-as** and **3** with slightly different relative intensities (Figure 3.24 (d)). The similar but non-identical XRPD patterns revealed that the dried structure of **2** had the same interlayer distance as well as the same intra-layer structure as compounds **3-as** and **3**, but its layer packing retained the ···A-A-A··· structure of **2-as**, instead of the ···A-B-A-B··· structure of **3-as**. To test the reversibility of structural transformation, **2**, **3-as**, and **3** was immersed in neat DEF solvent for 1 week. Interestingly, only the structure **2** was transformed into the expanded interlayer structure, but no change in structures for **3-as** and **3** were observed by XRPD patterns (Figure 3.25). It was confirmed that the different behaviors for guest inclusion of structure **2** and structures **3-as** and **3** were attributed to the different interlayer interaction. It suggested that the stacking manner of layers can play a critical role for flexible behaviors of 2D structure.

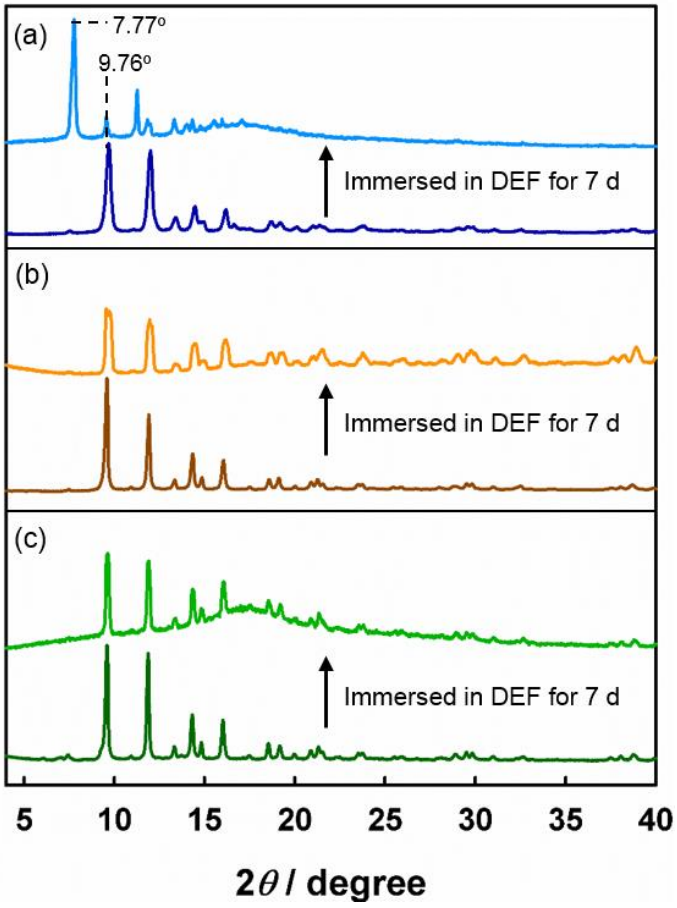


**Figure 3.25.** Comparison of XRPD patterns before and after immersion of frameworks in neat DEF for 7 d (a) **2** (before immersion, dark blue; after immersion, light blue) (b) **3-as** (before immersion, dark orange; after immersion, light orange) and (c) **3** (before immersion, dark green; after immersion, light green).

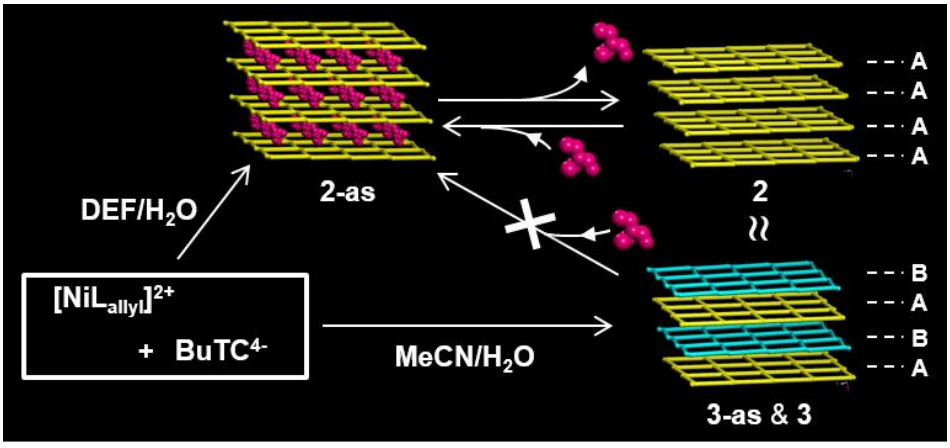


**Figure 3.26.** The schematic representation of structural transformation of **2** and **3**.

**Gas sorption properties of 2-as and 3-as.** Gas sorption behavior of **2** and **3** were studied with $N_2$, $H_2$, and $CO_2$. Both compounds **2** and **3** showed typical type II sorption behavior for $N_2$ adsorption, indicating the non-porous nature. However, both structure had different calculated BET surface area (6.7 $m^2/g$ for **2** and 30 $m^2/g$ for **3** at $P/P_0$ = 0.98) and total pore volume (3.2 × $10^{-2}$ $cm^3/g$ for **2** and 8.1× $10^{-2}$ $cm^3/g$ for **3**). The BET surface area of **2** is only 22% of **3** in spite of the same interlayer distance. In addition, the similar results were obtained for $H_2$ uptake at 77 K, both adsorbed very small amount of $H_2$ gas but different amount (2.30 $cm^3/g$ for **2** and 5.31 $cm^3/g$ for **3**). On the other hand, $CO_2$ gas sorption isotherms of **2** and **3** measured at 195 K exhibited different adsorption behaviors, even though the total uptake amounts were similar (2.5 wt% for **2**, and 2.7 wt% for **3**). **2** adsorbed $CO_2$ molecules with a two-step adsorption profile as well as a large hysteretic desorption curve. On the contrary, **3** showed no abrupt increase in adsorption of $CO_2$, that is **3** adsorbed $CO_2$ in a single-step, and it had a moderate hysteretic desorption curve.

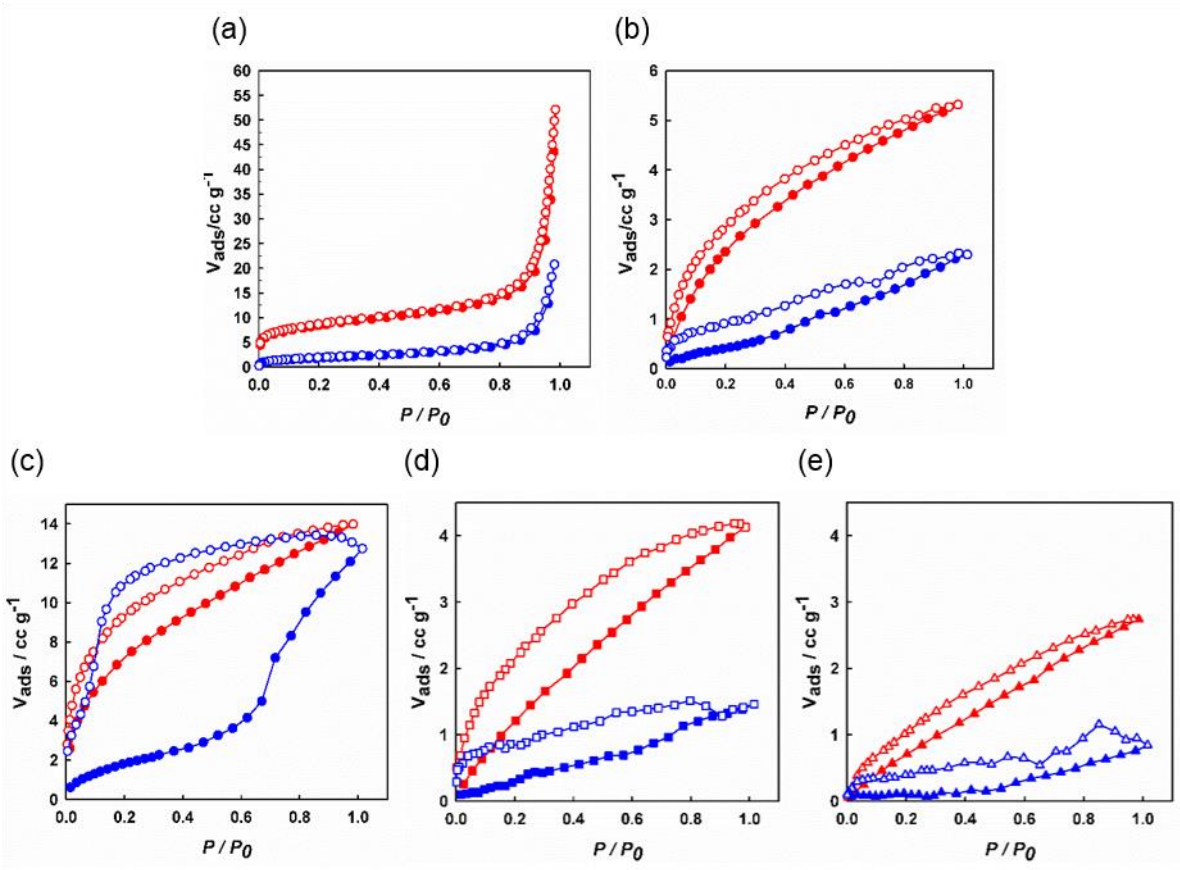


**Figure 3.27.** Gas sorption isotherms of **2** (red) and **3** (blue) (a) $N_2$ isotherms measured at 77 K, (b) $H_2$ isotherms measured at 77 K, (c) $CO_2$ isotherms measured at 195 K, (d) $CO_2$ isotherms measured at 273 K, and (e) $CO_2$ isotherms measured at 298 K.

These different behaviors for gas molecule uptake might be attributed to the subtle structural differences between **2** and **3** as described previously. Because the dried compounds of both **2** and **3** lost the single crystallinity, we couldn't analyze the exact difference in local structure but it might be inferred via the different stacking manner. Although the differences in structures are not distinguishable by XRPD patterns, the different packing manners results in the different inner pore structures.[7] In other words, **2** with the ···A-A-A··· structure gives more closed pores, and therefore it accommodate the smaller amount of gas molecules than **3** with the ···A-B-A-B··· structure. However, for $CO_2$ gas molecules, which have a small kinetic diameter (3.3 Å) and high quadrupole moment (-1.4 × $10^{-39}$ $cm^2$)[38] can induce the local structure change of **2** during adsorption, giving the similar porosity to **3**. The local structural changes might be attributed to the change in orientations of allyl pendent arms because they have flexibility and exposed in between the layers where the gas molecules enter the framework. The adsorbed $CO_2$ molecules interacted with the framework and changed the pendant groups, generating the open pores. Consequently, **2** shows the second large adsorption step, keeping the same interlayer distance in **2** and **3**. This allows the similar total amount of adsorbed $CO_2$.

**Structure of 4-as and 5-as.** To directly compare the effect of amine functional groups for $CO_2$ adsorption, two isostructural MOFs having functional ends with methyl and amine group due to their similar shape and formula weight. Thus, they were built with the same organic linker ($BPDC^{2-}$) and two Ni (II) macrocycles with propyl pendants ($[NiL_{propyl}]^{2+}$) and ethylamine pendants ($[NiL_{amine}]^{2+}$), respectively. The self-assembly of $BPDC^{2-}$ ligands and $[NiL_{amine}]^{2+}$ in DEF/MeCN/$H_2O$ mixture solution, and $[NiL_{propyl}]^{2+}$ in MeCN/$H_2O$ mixture solution generate $\{[(NiL_{amine})_2(BPDC)_2]\cdot(H_2O)_6\}$ (**4-as**) and $\{[(NiL_{propyl})_2(BPDC)_2]\cdot(H_2O)_5\}$(**5-as**), respectively. Both have same structure and it is confirmed by XRPD patterns of **4-as** and **5-as** (Figure 3.28).

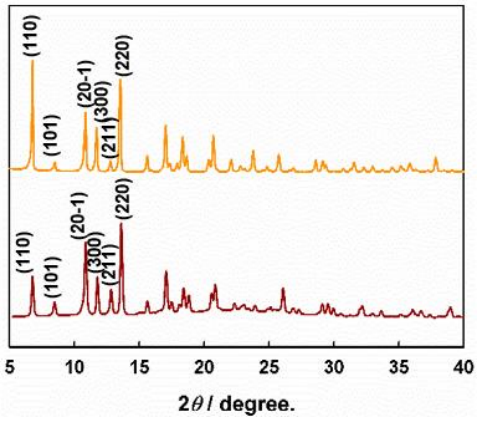


**Figure 3.28.** The collected XRPD patterns of **4-as** (dark red) and **5-as** (orange).

Both are crystallized in trigonal system in *R*-3 space group with little difference in cell parameters. Each $BPDC^{2-}$ ligand binds two Ni (II) complexes in a monodentate fashion, and the axial sites of each macrocycle with square planar geometry are occupied by two carboxylate oxygen atoms from two different $BPDC^{2-}$. The infinite coordination between $BPDC^{2-}$ and Ni (II) macrocycles yielded the 1D chains by resulting in octahedral Ni (II) centers, and they are extended in three different directions to construct a double network of threefold braids, which was previously reported.[39] Because **4-as** and **5-as** possess almost same structure, their simulated XPRD patterns showed similar patterns (Figure 3.28 (d)). Although there is very little difference between **4-as** and **5-as**, the void volume of each structure are 652.6 Å (9.6%) and 489.2 $Å^3$ (7.1%). Detailed single crystal X-ray crystallographic information and selected bond lengths and bond angles for **4-as** and **5-as** are listed in Table 3.11 and S29 to S30.

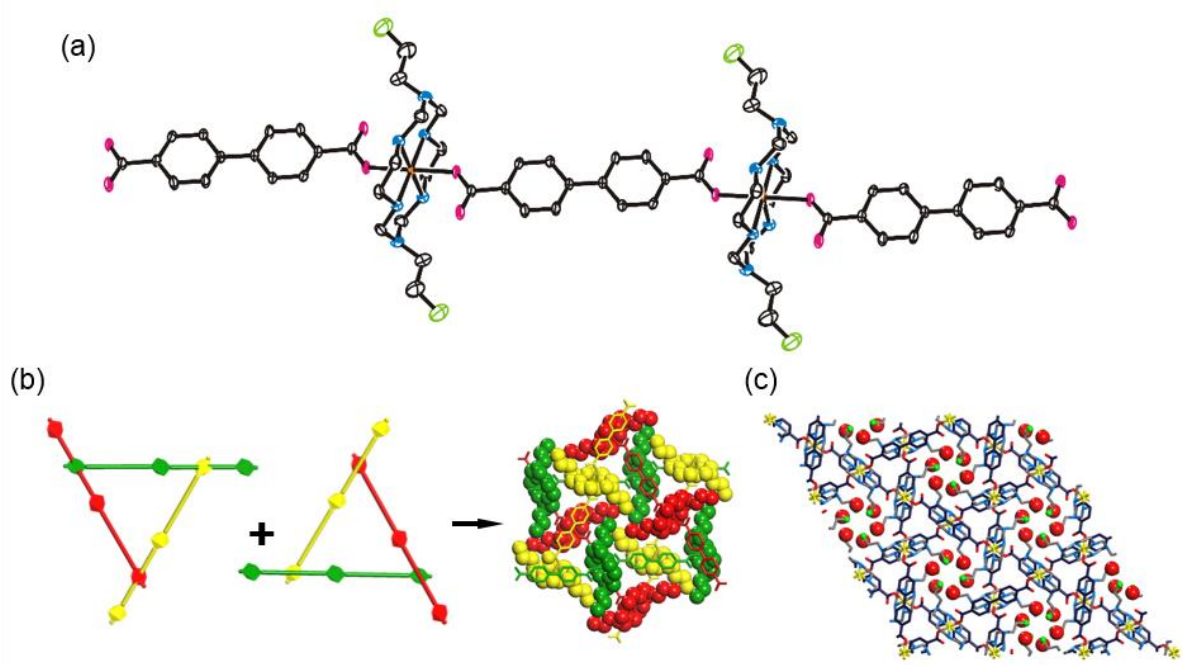


**Figure 3.29.** Schematic view for construction of isostructural frameworks for **4-as** and **5-as**. (a) An ORTEP drawing of 1D chain (thermal ellipsoids at 30% probability, C, black; N, blue; O, red). (b) A view for double network of threefold braids (c) *ab* plane view of framework. (Yellow green color in (a) and (c) represents N for **4-as** and C for **5-as**)

The three-directional packing generates honeycomb-like 1D channels, which are taken up by the macrocyclic pendant groups and water molecules, and the guest molecules are confirmed by x-ray diffraction, IR, TGA and EA. The guest water molecules in both structures were liberated at 90 °C under vacuum condition for 7 h, resulting in activated structures **4** and **5**, respectively. In addition, the macrocycles are located onto the flat plane of $BPDC^{2-}$ on other chain with interchain CH···π

interactions between the CH of macrocycle and the phenyl rings of the $BPDC^{2-}$ (the average C-H$\cdots\pi$ distance, 3.174 Å; dihedral angles, 43.5°). Due to the interchain interaction, the framework are rigid and their structure were kept in same during activation. Therefore, all XRPD patterns of as-synthesized and activated samples were matched with simulated patterns of each structure.

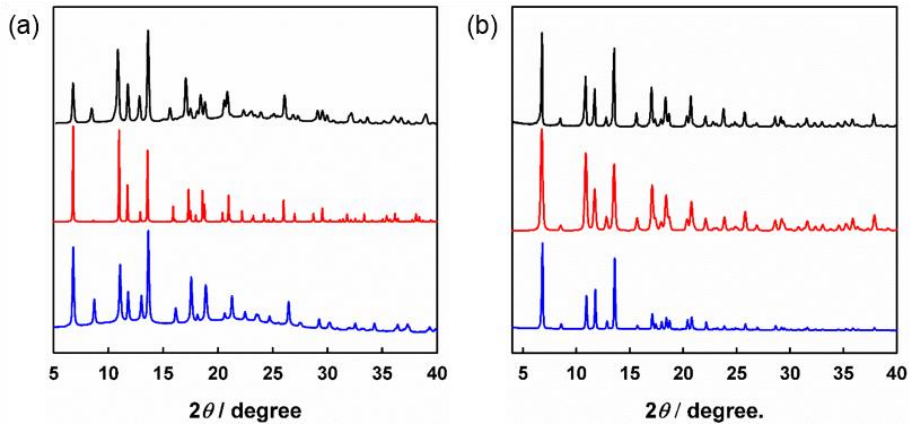


**Figure 3.30.** XRPD patterns of (a) **4-as** and **4**, and (b) **5-as** and **5**. (Simulated pattern, red; as-synthesized compound, black; dried compound, blue)

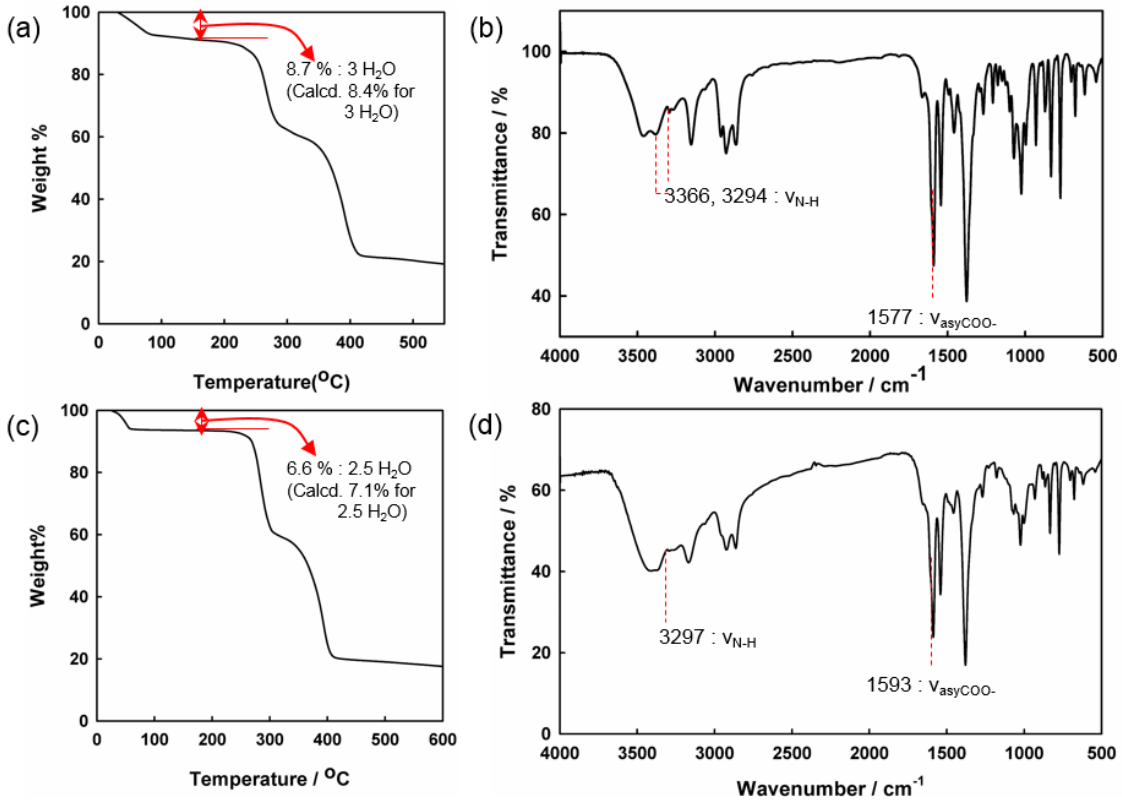


**Figure 3.31.** IR spectra and TGA traces of **4-as** ((a) and (b)) and **5-as** ((c) and (d)).

**Table 3.11**. X-ray crystallographic data of **4-as** and **5-as**.

| Compound | **4-as** | **5-as** |
|---|---|---|
| formula | $Ni_1C_{26}H_{40}N_8O_6$ | $NiC_{28}H_{46}N_6O_6$ |
| crystal system | *Trigonal* | *Trigonal* |
| space group | *R*-3 :*H* | *R*-3 :*H* |
| fw | 619.37 | 621.42 |
| *a*, Å | 26.077(4) | 26.1625(8) |
| *b*, Å | 26.077(4) | 26.1625(8) |
| *c*, Å | 11.485(2) | 11.6677(3) |
| $\alpha$, deg | 90 | 90 |
| $\beta$, deg | 90 | 90 |
| $\gamma$, deg | 120 | 120 |
| *V*, Å $^3$ | 6764(2) | 6916.3(5) |
| *Z* | 9 | 9 |
| $\rho_{calcd}$, g cm$^{-3}$ | 1.369 | 1.343 |
| temp , K | 100(2) | 173(2) |
| $\lambda$, Å | 0.70000 | 0.71073 |
| $\mu$, mm$^{-1}$ | 0.698 | 0.681 |
| goodness-of-fit ($F^2$) | 1.066 | 1.048 |
| *F*(000) | 506 | 2988 |
| reflections collected | 16864 | 20065 |
| independent reflections | 2922 [*R*(int) = 0.0268] | 3009 [*R*(int) = 0.0280] |
| completeness to $\theta_{max}$, % | 94.5% | 99.4% |
| data/parameters/restraints | 2922 / 24 / 187 | 3009 / 0 / 178 |
| $\theta$ range for data collection, | 2.928 to 25.997 | 3.115 to 25.980 |
| diffraction limits (*h*, *k*, *l*) | $-32 \le h \le 32$, $-32 \le k \le 32$, $-13 \le l \le 13$ | $-32 \le h \le 32$, $-32 \le k \le 32$, $-14 \le l \le 13$ |
| refinement method | Full-matrix least-squares on $F^2$ | Full-matrix least-squares on $F^2$ |
| $R_1$, $wR_2$ [$I>2\sigma(I)$] | $R_1$ = 0.0652,[a] $wR_2$ = 0.1975[b] | $R_1$ = 0.0472,[a] $wR_2$ = 0.1263[c] |
| $R_1$, $wR_2$ (all data) | $R_1$ = 0.0699,[a] $wR_2$ = 0.2034[b] | $R_1$ = 0.0542,[a] $wR_2$ = 0.1321[c] |
| largest peak, hole, eÅ $^{-3}$ | 0.696, -0.533 | 0.682, -0.394 |

[a] $R = \Sigma||F_O| - |F_C||/\Sigma|F_O|$. [b] $wR(F^2) = [\Sigma w(F_O^2 - F_C^2)^2/\Sigma w(F_O^2)^2]^{1/2}$ where $w = 1/[\sigma^2(F_O^2) + (0.1505P)^2 + (7.0566)P]$, $P = (F_O^2 + 2F_C^2)/3$. [c] $wR(F^2) = [\Sigma w(F_O^2 - F_C^2)^2/\Sigma w(F_O^2)^2]^{1/2}$ where $w = 1/[\sigma^2(F_O^2) + (0.0728P)^2 + (16.1542)P]$, $P = (F_O^2 + 2F_C^2)/3$.

**Gas sorption properties of 4 and 5.** To examine the effect of amines on CO2 capture, gas sorption isotherms were measured with $N_2$, $H_2$ and $CO_2$ for **4** and **5**. $N_2$ isotherm of **4** showed type II shape and **5** showed negligible uptake, indicating non-porous nature of both structure. $H_2$ sorption supported their non-porous properties, and the uptake amount of **4** was larger than **5** due to the difference in void space. However, the $CO_2$ sorption behaviors of **4** and **5** measured at 195 K indicated reversed result. The framework **4** (3.74 cc/g) adsorbed much smaller amount of $CO_2$ than **5** (47.46 cc/g) at 195 K. Moreover, the amount of $CO_2$ uptake for the framework **4** increased at the temperature increased, which is not common in physisorbing MOFs (Figure 3.31). In addition, desorption isotherms were not trace back to the adsorption plot with large hysteresis and they cannot be desorbed completely. However, **5** showed drastic decrease of $CO_2$ uptake upon the temperature rise and there was no hysteresis at 273 and 298 K, only the isotherms at 195 K showed small hysteresis, and the framework **4** adsorbed larger amount of $CO_2$ at 298 K (13.6 cc/g) than **5** (5.45 cc/g).

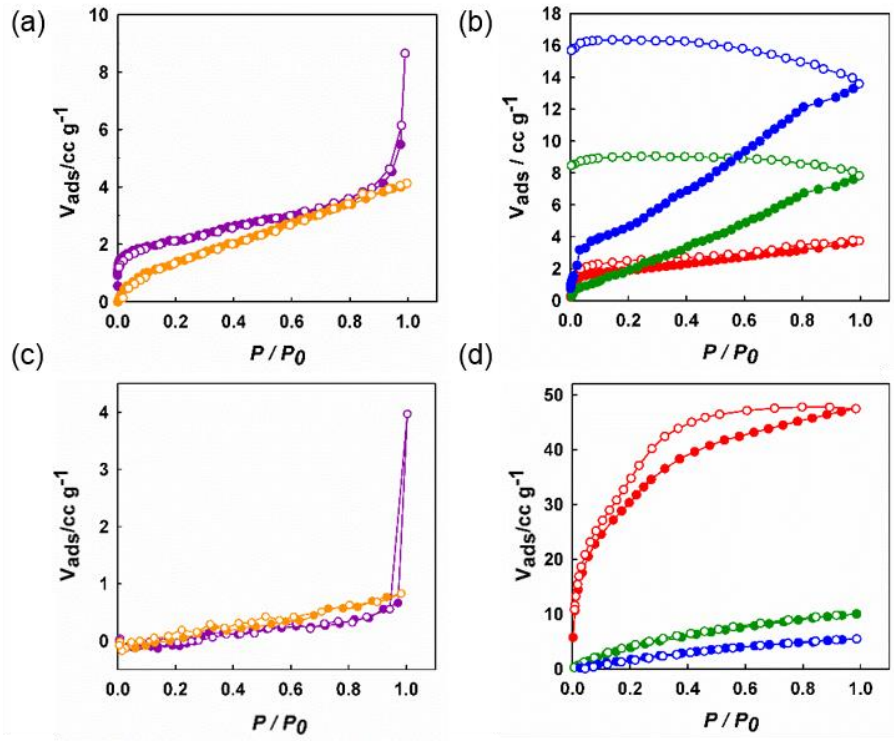


**Figure 3.32.** Gas sorption isotherms of **4** (a, b) and **5** (c, d). (a, c) $N_2$ (dark pink) and $H_2$ (orange) isotherms measured at 77K and (b, d) $CO_2$ isotherms measured at 195 K (red), 273 K (green), and 298 K (blue).

These differences seemed to arise from the amine functional groups on the pore surface. The low uptake of $CO_2$ for **4** at 195 K could be attributed to the small-size pore and the interaction between amine and $CO_2$. The adsorbed $CO_2$ molecules interact with abundant amine groups on the surface of the channel and it block the pore due to narrow aperture. Thus, $CO_2$ molecules cannot diffuse further into the pore. However, the temperature 195 K is too low to overcome the barrier for making bonds between $CO_2$ and amines,[33] and therefore the desorption could be achieved at 195 K. As temperature increased to 273 and 298 K, the diffusion of $CO_2$ could be enhanced and therefore the gas molecules could take up the larger portion of crystals and interact with more amines. As a result, the amount of $CO_2$ uptake would be increased upon temperature rise. In addition, higher temperature gave enough energy to overcome the barrier for C-N bond formation between N of amine and C of $CO_2$. Consequently, the end of desorption curves showed large hysteresis and couldn't meet with the adsorption curves.

To confirm the formation of chemical bonding between $CO_2$ and amine and the resulting pore-blocking, the change in the exposed surface and size of crystals of **4** was required. Thus, gas sorption isotherms were collected with the sample **4** possessing two different size distribution. To prepare different size of **4**, one sample was prepared in crystal form without grinding ($\mathbf{4_{xstal}}$) and the other was ground finely ($\mathbf{4_{grind}}$), and both samples were activated at the same condition (heating to 90 $^oC$ under vacuum for 7 h). The different size distributions depending on sample preparation methods were measured with scanning election microscope (SEM) images. $\mathbf{4_{xstal}}$ showed fragments of rod shape with average size of 58.7 $\mu$m distributed from 23.7 to 158 $\mu$m. On the other hand, $\mathbf{4_{grind}}$ had no particular shape composed of fine particles with average size of 3.62 $\mu$m and larger particles with average size of 18.1 $\mu$m. The resulting $N_2$ and $H_2$ isotherms of $\mathbf{4_{xstal}}$ and $\mathbf{4_{grind}}$ showed similar behavior, indicating that there was no other changes apart from the size. On the other hand, $CO_2$ isotherms were different for each sample. The sample $\mathbf{4_{grind}}$ adsorbed larger amount of $CO_2$ than $\mathbf{4_{xstal}}$ but both showed same isotherm shapes (Figure 3.32). In addition, the series of $CO_2$ sorption measurement at 298 K suggested that $CO_2$ adsorption of **4** occurred with making chemical bonds. After measuring $CO_2$ sorption isotherms at 298 K, the second measurement without activation step was performed. Then, the uptake amount was reduced to 7.28 cc/g for $\mathbf{4_{xstal}}$ and 9.26 cc/g for $\mathbf{4_{grind}}$, indicating reduced free space due to unremoved $CO_2$ molecules of previous measurement. To confirm that the reduction in uptake amount didn't come from the collapse of framework, the third $CO_2$ sorption was obtained after evacuating samples at 120 $^oC$ under vacuum condition for 1 h. Then, the uptake amount was recovered for $\mathbf{4_{grinding}}$ and even enhanced for $\mathbf{4_{xstal}}$, which could result from the creation of defects on crystals upon the activation. Consequently, the framework **4** adsorbs $CO_2$ in chemisorption manner and therefore high temperature would be required to regenerate samples.

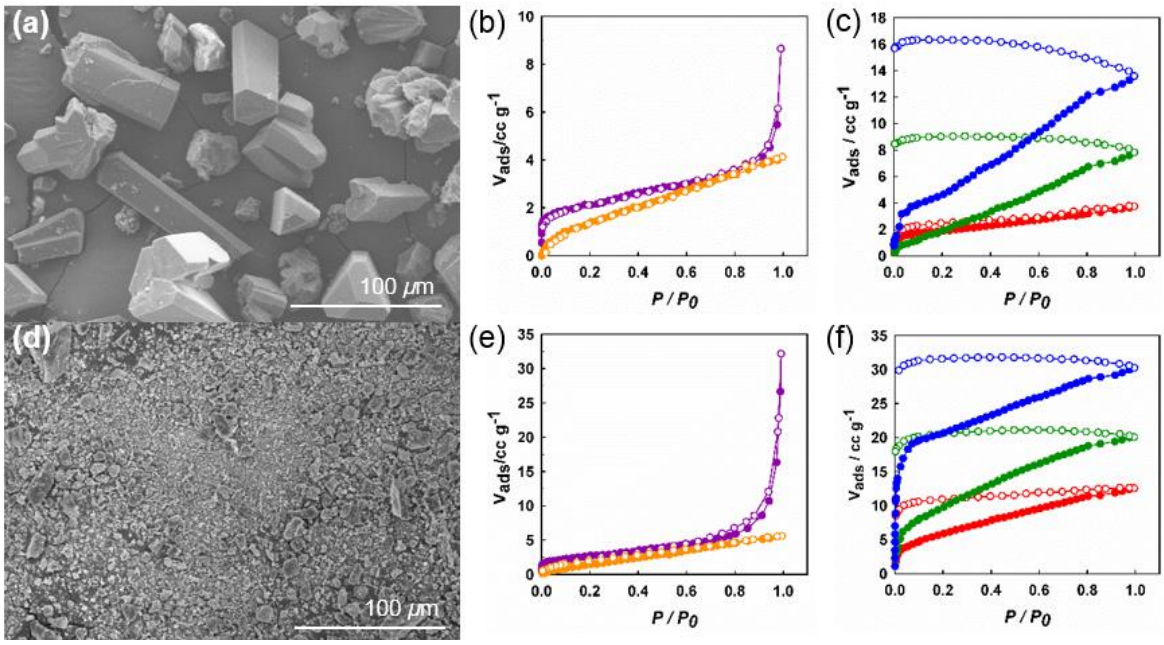


**Figure 3.33.** Comparison of $\mathbf{4}_{\mathbf{xstal}}$ and $\mathbf{4}_{\mathbf{grind}}$. SEM images of (a) $\mathbf{4}_{\mathbf{xstal}}$ and (d) $\mathbf{4}_{\mathbf{grind}}$. Gas sorption isotherms of $N_2$ (dark pink) and $H_2$ (orange) at 77 K for (b) $\mathbf{4}_{\mathbf{xstal}}$ and (e) $\mathbf{4}_{\mathbf{grind}}$, and of $CO_2$ at 195 (red), 273 (green), and 298 K (blue) for (c) $\mathbf{4}_{\mathbf{xstal}}$ and (f) $\mathbf{4}_{\mathbf{grind}}$.

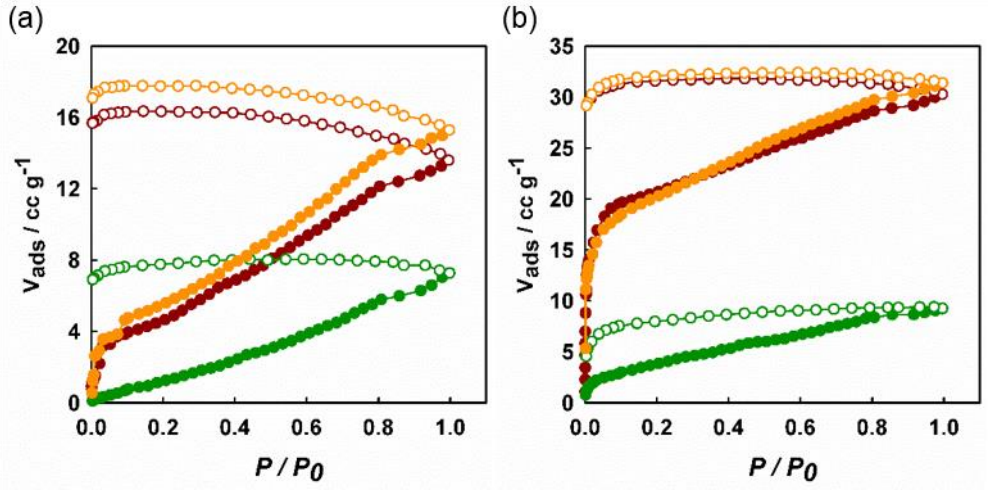


**Figure 3.34.** $CO_2$ gas sorption isotherms of **4** at 298 K. Gas sorption isotherms were measured in two different sample preparation (a) without grinding the sample and (b) with grinding the sample.

To prove the chemisorption between amine and $CO_2$ further, $CO_2$ adsorption-desorption cycling experiments of **4** and **5** were conducted with TGA instruments. The samples **4-as** and **5-as** were ground and were activated at 120 $^oC$ under $N_2$ flow in sample holder of TGA instrument. After activation the samples were cooled down to 30 $^oC$ and then $CO_2$ gas flowed onto samples **4** and **5** resulting in the increase in weight of 3.1 wt% and 0.23 wt% (Figure 3.34 (a) and (b)), respectively. After flowing $CO_2$ for 1 h, flowing gas was changed to $N_2$ for desorption at the same temperature for 1h. For the sample **5**, rapid decrease in weight was observed, indicating weak interaction between $CO_2$ and framework **5**, and similar adsorption-desorption shape was kept during cycles (Figure 3.33 (b)). On the other hand, the weight of **4** was slowly decreased by 0.8 wt% and increased to 1.2 wt% for next adsorption (Figure 3.34 (a)), and its behavior would be changed when the sample was regenerated at 120 $^oC$ under $N_2$ flow for 1 h (Figure 3.33 (c)). The weight dropped sharply during desorption step, and it showed similar adsorption-desorption shape upon repeating cycles. Therefore, it is confirmed that amine functional groups decorated on the pore surface could enhance the interaction between $CO_2$ and MOFs via making chemical bonds.

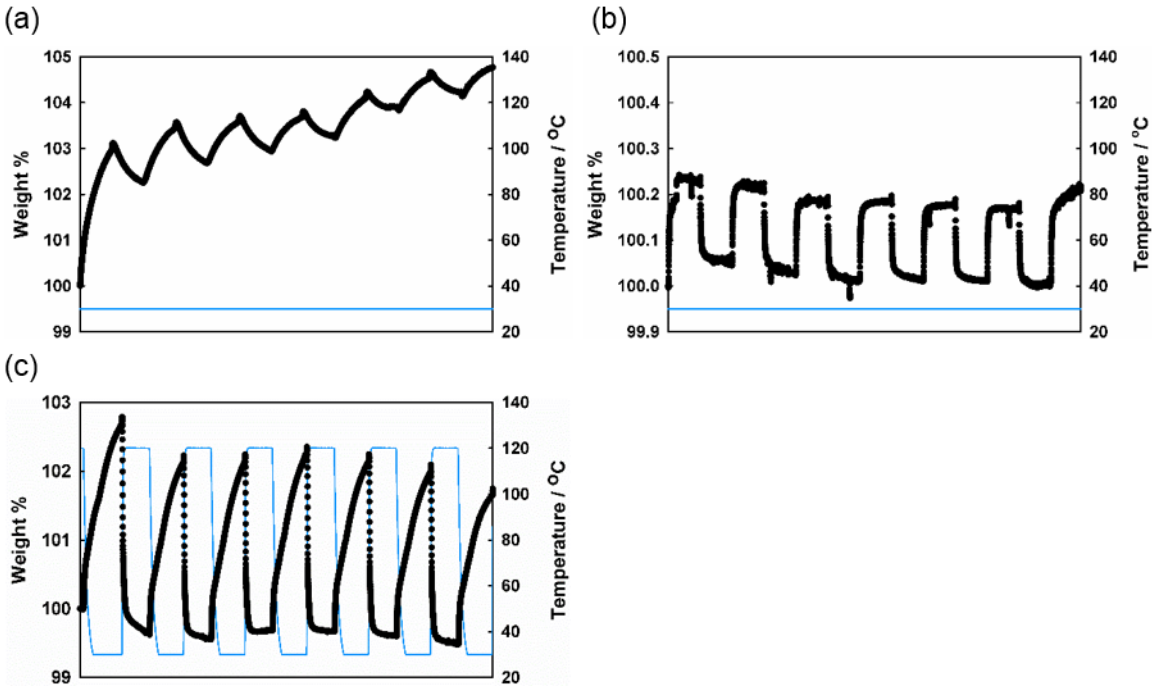


**Figure 3.35.** $CO_2$ gas adsorption-desorption cycling results (blue-line-plot, temperature; black-dot-plot, weight%). For adsorption for all sample, $CO_2$ gas was flowed onto the sample at 30 $^oC$ for 1 h. (a) For **4** and (b) **5**, samples were regenerated at 30 $^oC$ under $N_2$ flow for 1 h. (c) The sample was regenerated at 120 $^oC$ under $N_2$ flow for 1 h for **4**.

## IV. Conclusion

We have synthesized several MOFs via self-assembly methods for studying their flexible behaviors and gas sorption properties, especially for $CO_2$. To research the structural dynamics of flexible MOFs, we have prepared {[$(NiL_{propyl})_2$(BPTC)]·4DMF·$2H_2O$} (**1-as**), {[$(NiL_{allyl})_2$(BuTC)]·2DEF·$2H_2O$} (**2-as**), and {[$(NiL_{allyl})_2$(BuTC)]·$3H_2O$} (**3-as**) through incorporating flexible building blocks. To build a flexible MOF, the host frameworks need to possess flexible moieties. Thus, we employed $H_4$BPTC as an organic linker since it has many rotational motifs between two phenyl rings and between phenyl rings and four carboxylate groups. In addition, a Ni(II) macrocyclic complex, $[NiL_{propyl}]^{2+}$, was used as a linear metal building block with two axial coordination sites and its square planar geometry. The reason why we utilized a linear metal node is linear connection can rotate more freely than other metal clusters having bonds at least two different directions. Furthermore, $[NiL_{propyl}]^{2+}$ has two propyl chains as pendants, which can act as a gate of pore through changing the pore shape, volume, and accessibility depending on their orientations. Due to flexibility of **1-as**, the structure of **1-as** changed upon various external stimuli, such as temperature, and kinds of and the amount of guest molecules. In addition, the activated compound of **1-as** (**1**) has a shrunk and closed structure as evidenced by gas sorption and XRPD measurements. However, it selectively adsorbed $CO_2$ at 195 K up to 1 atm and at 298 K up to 30 bar in two-step via structural transformation to expanded and porous structure. Furthermore, *in-situ* XRPD patterns revealed that the structural transition of **1** upon $CO_2$ uptake at 195 K was occurred in two distinct steps, gate-opening and breathing independently. From the single crystal x-ray diffraction data, we could find the origin of this flexible behavior, gate-opening and breathing. Gate-opening happened through rotation of Ni (II) macrocycles with breaking and reconstruction of hydrogen bonds between secondary amines on macrocycles and carboxylates. On the other hand, breathing resulted from the rotation of single bonds in $BPTC^{4-}$ ligands.

Moreover, 2D coordination polymers offers a good example for demonstrating the flexible change in their structures depending on the amount as well as the size and shape of the intercalated guest molecules. Thus, we incorporated a flexible aliphatic organic linkers, extending four directions on a layer, and a Ni (II) macrocyclic complex, $[NiL_{allyl}]^{2+}$ as a metal building block for a linear linker. To understand the guest-host interaction on forming the whole structure of layered MOFs and on their properties, we utilized two different mixture solutions DEF/$H_2O$ and MeCN/$H_2O$, respectively for synthesizing **2-as** and **3-as**. Since both MOFs were constructed from the same building blocks, the structure of each layer was identical, but layer packing and interlayer distance were different depending on the size and the nature of guest molecules. Interestingly, **2-as** was easily contracted upon losing guest molecules, resulting in the same interlayer distance as **3-as** and **3** but different interlayer and intra-layer structure. The similar but non-identical structure gave that the difference in

the reversibility of structural transformation and in $CO_2$ uptake behaviors at 195 K.

To study about the gas sorption properties of MOFs especially for $CO_2$, many researches for amine-functionalized MOFs were done and they have brought many attention to the potentials of MOFs as a $CO_2$ adsorbent. However, most of them showed the effect of amine groups without comparison group or with comparison group of different formula weight, pore shape and size. Therefore, the exact effects of amine groups in MOFs were not directly observed. Thus, we plan to incorporate methyl and amine functional groups for synthesizing two similar structure MOFs with different fucntional groups of similar formula weight for directly comparing the weight percent of adsorbed $CO_2$ between two MOFs with and without amine groups. Therefore, two isostructural MOFs with little difference in formula weight and similar pores possessing different functional groups, **4-as** and **5-as**, were constructed. After activation of compounds, **4** and **5** were obtained and the gas sorption isotherms for both frameworks were measured. They showed very different $CO_2$ sorption behavior. The framework **4** indicated chemisorption behaviors but **5** only showed physisorption characteristics. It was confirmed through gas sorption isotherms and TGA cycling.

## V. Supporting Information

**Table S1**. Selected bond distances [Å ] and angles [°] of **1-as (195K)**.

| | | | |
|---|---|---|---|
| Ni(1A)-N(1A)$^{\#1}$ | 2.0627(13) | Ni(2B)-N(1B)$^{\#2}$ | 2.0613(15) |
| Ni(1A)-N(1A) | 2.0627(13) | Ni(2B)-N(1B) | 2.0613(15) |
| Ni(1A)-N(2A)$^{\#1}$ | 2.0523(13) | Ni(2B)-N(2B)$^{\#2}$ | 2.0580(18) |
| Ni(1A)-N(2A) | 2.0524(13) | Ni(2B)-N(2B) | 2.0580(18) |
| Ni(1A)-O(1C)$^{\#1}$ | 2.1329(11) | Ni(2B)-O(3C)$^{\#2}$ | 2.1159(12) |
| Ni(1A)-O(1C) | 2.1328(11) | Ni(2B)-O(3C) | 2.1159(12) |
| | | | |
| N(1A)$^{\#1}$-Ni(1A)-N(1A) | 180.0 | N(1B)$^{\#2}$-Ni(2B)-N(1B) | 180.0 |
| N(1A)$^{\#1}$-Ni(1A)-N(2A)$^{\#1}$ | 94.18(6) | N(1B)$^{\#2}$-Ni(2B)-N(2B)$^{\#2}$ | 94.03(7) |
| N(1A)$^{\#1}$-Ni(1A)-N(2A) | 85.82(6) | N(1B)$^{\#2}$-Ni(2B)-N(2B) | 85.97(7) |
| N(1A)$^{\#1}$-Ni(1A)-O(1C)$^{\#1}$ | 90.67(5) | N(1B)$^{\#2}$-Ni(2B)-O(3C)$^{\#2}$ | 91.72(5) |
| N(1A)$^{\#1}$-Ni(1A)-O(1C) | 89.33(5) | N(1B)$^{\#2}$-Ni(2B)-O(3C) | 88.28(5) |
| N(1A)-Ni(1A)-N(2A)$^{\#1}$ | 85.82(6) | N(1B)-Ni(2B)-N(2B)$^{\#2}$ | 85.97(7) |
| N(1A)-Ni(1A)-N(2A) | 94.18(6) | N(1B)-Ni(2B)-N(2B) | 94.03(7) |
| N(1A)-Ni(1A)-O(1C)$^{\#1}$ | 89.33(5) | N(1B)-Ni(2B)-O(3C)$^{\#2}$ | 88.28(5) |
| N(1A)-Ni(1A)-O(1C) | 90.67(5) | N(1B)-Ni(2B)-O(3C) | 91.72(5) |
| N(2A)$^{\#1}$-Ni(1A)-N(2A) | 180.0 | N(2B)$^{\#2}$-Ni(2B)-N(2B) | 180 |
| N(2A)$^{\#1}$-Ni(1A)-O(1C)$^{\#1}$ | 88.15(5) | N(2B)$^{\#2}$-Ni(2B)-O(3C)$^{\#2}$ | 88.46(6) |
| N(2A)$^{\#1}$-Ni(1A)-O(1C) | 91.85(5) | N(2B)$^{\#2}$-Ni(2B)-O(3C) | 91.54(6) |
| N(2A)-Ni(1A)-O(1C)$^{\#1}$ | 91.85(5) | N(2B)-Ni(2B)-O(3C)$^{\#2}$ | 91.54(6) |
| N(2A)-Ni(1A)-O(1C) | 88.15(5) | N(2B)-Ni(2B)-O(3C) | 88.46(6) |
| O(1C)$^{\#1}$-Ni(1A)-O(1C) | 180.0 | O(3C)$^{\#2}$-Ni(2B)-O(3C) | 180.0 |

Symmetry transformations used to generate equivalent atoms:

#1 -x,-y+1,-z  #2 -x+1/2,-y+1/2,-z+1

**Table S2**. Selected torsion angles [°] of **1-as (195 K)**.

| | |
|---|---|
| C(2C)-C(7C) : C(2C)$^{\#1}$ - C(7C)$^{\#1}$ | 45.843(49) |
| O(1C)-C(1C)-O(2C) : C(2C)-C(7C) | 66.080(113) |
| O(3C)-C(8C)-O(4C) : C(2C)-C(7C) | 7.798(72) |

Symmetry transformations used to generate equivalent atoms:

#1 -x, y, -z+1/2

**Table S3**. Hydrogen bonds for **1-as (195 K)** [Å and °].

| D-H···A | d(D-H) | d(H···A) | d(D···A) | ∠(DHA) |
|---|---|---|---|---|
| N(1A)-H(1A)...O(4C)$^{\#2}$ | 1.00 | 2.22 | 2.9784(18) | 131.2 |
| N(2A)-H(2A)...O(2C)$^{\#1}$ | 1.00 | 1.94 | 2.8596(18) | 152.3 |
| N(1B)-H(1B)...O(4C)$^{\#2}$ | 1.00 | 2.02 | 2.9377(19) | 151.5 |

Symmetry transformations used to generate equivalent atoms:

#1 -x,-y+1,-z #2 x,-y+1,z-1/2

**Table S4**. X-ray crystallographic data of **1-as**.

| Compound | **1-as (100 K)** | **1-as (298 K)** |
|---|---|---|
| formula | $Ni_1C_{22}H_{37}N_6O_4$ | $Ni_1C_{22}H_{37}N_6O_4$ |
| crystal system | *Monoclinic* | *Monoclinic* |
| space group | *C*2/*c* | *C*2/*c* |
| fw | 508.28 | 508.28 |
| *a*, Å | 29.857(6) | 29.537(6) |
| *b*, Å | 11.770(2) | 12.514(3) |
| *c*, Å | 22.002(4) | 22.209(4) |
| $\alpha$, deg | 90 | 90 |
| $\beta$, deg | 114.78(3) | 114.76(3) |
| $\gamma$, deg | 90 | 90 |
| *V*, Å $^3$ | 7020(3) | 7454(3) |
| *Z* | 8 | 8 |
| $\rho_{calcd}$, g cm$^{-3}$ | 0.962 | 0.906 |
| temp , K | 100(2) | 298(2) |
| $\lambda$, Å | 0.65002 | 0.62998 |
| $\mu$, mm$^{-1}$ | 0.456 | 0.394 |
| goodness-of-fit ($F^2$) | 1.057 | 1.094 |
| *F*(000) | 2168 | 2168 |
| reflections collected | 30585 | 37780 |
| independent reflections | 8287 [*R*(int) = 0.0187] | 9898 [*R*(int) = 0.0225] |
| completeness to $\theta_{max}$, % | 91.3% | 94.6% |
| data / parameters / restraints | 8287 / 6 / 396 | 9898 / 0 / 303 |
| $\theta$ range for data | 2.742 to 26.000 | 2.653 to 25.999 |
| diffraction limits (*h*, *k*, *l*) | -40≤*h*≤40, -15≤*k*≤15,-29≤*l*≤28 | -41≤*h*≤41, -17≤*k*≤17,-.30≤*l*≤30 |
| refinement method | Full-matrix least-squares on $F^2$ | Full-matrix least-squares on $F^2$ |
| $R_1$, $wR_2$ [$I>2\sigma(I)$] | $R_1$ = 0.0406[a], $wR_2$ = 0.1149[b] | $R_1$ = 0.0499[a], $wR_2$ = 0.1742[c] |
| $R_1$, $wR_2$ (all data) | $R_1$ = 0.0414[a], $wR_2$ = 0.1155[b] | $R_1$ = 0.0539[a], $wR_2$ = 0.1792[c] |
| largest peak, hole, eÅ $^{-3}$ | 0.776, -0.437 | 0.567, -0.659 |

[a] $R = \Sigma||F_O| - |F_C||/\Sigma|F_O|$. [b] $wR(F^2) = [\Sigma w(F_O^2 - F_C^2)^2/\Sigma w(F_O^2)^2]^{1/2}$ where $w = 1/[\sigma^2(F_O^2) + (0.0617P)^2 + (10.3409)P]$, $P = (F_O^2 + 2F_C^2)/3$. [c] $wR(F^2) = [\Sigma w(F_O^2 - F_C^2)^2/\Sigma w(F_O^2)^2]^{1/2}$ where $w = 1/[\sigma^2(F_O^2) + (0.1281P)^2 + (1.2200)P]$, $P = (F_O^2 + 2F_C^2)/3$.

**Table S5**. Selected bond distances [Å ] and angles [º] of **1-as (100 K)**.

| | | | |
|---|---|---|---|
| Ni(1A)-N(1A1)$^{\#1}$ | 2.062(5) | Ni(2B)-N(1B)$^{\#2}$ | 2.0612(14) |
| Ni(1A)-N(1A1) | 2.062(5) | Ni(2B)-N(1B) | 2.0611(14) |
| Ni(1A)-N(2A1)$^{\#1}$ | 2.053(3) | Ni(2B)-N(2B)$^{\#2}$ | 2.0591(16) |
| Ni(1A)-N(2A1) | 2.053(3) | Ni(2B)-N(2B) | 2.0592(16) |
| Ni(1A)-O(1C)$^{\#1}$ | 2.1182(11) | Ni(2B)-O(3C)$^{\#2}$ | 2.1083(12) |
| Ni(1A)-O(1C) | 2.1181(11) | Ni(2B)-O(3C) | 2.1083(12) |
| | | | |
| N(1A1)$^{\#1}$-Ni(1A)-N(1A1) | 180.0 | N(1B)$^{\#2}$-Ni(2B)-N(1B) | 180.0 |
| N(1A1)$^{\#1}$-Ni(1A)-N(2A1)$^{\#1}$ | 93.87(12) | N(1B)$^{\#2}$-Ni(2B)-N(2B)$^{\#2}$ | 93.96(6) |
| N(1A1)$^{\#1}$-Ni(1A)-N(2A1) | 86.13(12) | N(1B)$^{\#2}$-Ni(2B)-N(2B) | 86.04(6) |
| N(1A1)$^{\#1}$-Ni(1A)-O(1C)$^{\#1}$ | 91.48(15) | N(1B)$^{\#2}$-Ni(2B)-O(3C)$^{\#2}$ | 91.72(5) |
| N(1A1)$^{\#1}$-Ni(1A)-O(1C) | 88.52(15) | N(1B)$^{\#2}$-Ni(2B)-O(3C) | 88.28(5) |
| N(1A1)-Ni(1A)-N(2A1)$^{\#1}$ | 86.13(12) | N(1B)-Ni(2B)-N(2B)$^{\#2}$ | 86.04(6) |
| N(1A1)-Ni(1A)-N(2A1) | 93.87(12) | N(1B)-Ni(2B)-N(2B) | 93.96(6) |
| N(1A1)-Ni(1A)-O(1C)$^{\#1}$ | 88.52(15) | N(1B)-Ni(2B)-O(3C)$^{\#2}$ | 88.27(5) |
| N(1A1)-Ni(1A)-O(1C) | 91.48(15) | N(1B)-Ni(2B)-O(3C) | 91.72(5) |
| N(2A1)$^{\#1}$-Ni(1A)-N(2A1) | 180.0 | N(2B)$^{\#2}$-Ni(2B)-N(2B) | 180.0 |
| N(2A1)$^{\#1}$-Ni(1A)-O(1C)$^{\#1}$ | 87.91(8) | N(2B)$^{\#2}$-Ni(2B)-O(3C)$^{\#2}$ | 88.46(6) |
| N(2A1)$^{\#1}$-Ni(1A)-O(1C) | 92.09(8) | N(2B)$^{\#2}$-Ni(2B)-O(3C) | 91.55(6) |
| N(2A1)-Ni(1A)-O(1C)$^{\#1}$ | 92.09(8) | N(2B)-Ni(2B)-O(3C)$^{\#2}$ | 91.54(6) |
| N(2A1)-Ni(1A)-O(1C) | 87.91(8) | N(2B)-Ni(2B)-O(3C) | 88.46(6) |
| O(1C)$^{\#1}$-Ni(1A)-O(1C) | 180.0 | O(3C)$^{\#2}$-Ni(2B)-O(3C) | 180.0 |

Symmetry transformations used to generate equivalent atoms:

#1 -x,-y+1,-z #2 -x+1/2,-y+1/2,-z+1

**Table S6**. Selected torsion angles [º] of **1-as (100 K)**.

| | |
|---|---|
| C(2C)-C(7C) : C(2C)$^{\#1}$ - C(2C)$^{\#1}$ | 47.342(47) |
| O(1C)-C(1C)-O(2C) : C(2C)-C(7C) | 67.069(106) |
| O(3C)-C(8C)-O(4C) : C(2C)-C(7C) | 7.064(68) |

Symmetry transformations used to generate equivalent atoms:

#1 -x, y, -z+1/2

**Table S7**. Hydrogen bonds for **1-as (100 K)** [Å and °].

| D-H···A | d(D-H) | d(H···A) | d(D···A) | ∠(DHA) |
|---|---|---|---|---|
| N(2A1)-H(2A1)...O(2C)$^{\#1}$ | 1.00 | 1.94 | 2.859(3) | 150.8 |
| N(2A)-H(2A)...O(4C)$^{\#2}$ | 1.00 | 2.20 | 2.945(5) | 130.4 |
| N(1B)-H(1B)...O(4C) | 1.00 | 2.02 | 2.9415(19) | 151.4 |

Symmetry transformations used to generate equivalent atoms:

#1 -x,-y,-z #2 x,-y,z-1/2

**Table S8**. Selected bond distances [Å ] and angles [º] of **1-as (298 K)**.

| | | | |
|---|---|---|---|
| Ni(1A)-N(1A)$^{\#1}$ | 2.0475(15) | Ni(2B)-N(1B)$^{\#2}$ | 2.0536(16) |
| Ni(1A)-N(1A) | 2.0475(15) | Ni(2B)-N(1B) | 2.0535(16) |
| Ni(1A)-N(2A)$^{\#1}$ | 2.0628(14) | Ni(2B)-N(2B)$^{\#2}$ | 2.050(2) |
| Ni(1A)-N(2A) | 2.0628(14) | Ni(2B)-N(2B) | 2.049(2) |
| Ni(1A)-O(1C)$^{\#1}$ | 2.1521(11) | Ni(2B)-O(3C)$^{\#2}$ | 2.1243(13) |
| Ni(1A)-O(1C) | 2.1520(11) | Ni(2B)-O(3C) | 2.1244(13) |
| | | | |
| N(1A)$^{\#1}$-Ni(1A)-N(1A) | 180.0 | N(1B)$^{\#2}$-Ni(2B)-N(1B) | 180.0 |
| N(1A)$^{\#1}$-Ni(1A)-N(2A)$^{\#1}$ | 94.18(6) | N(1B)$^{\#2}$-Ni(2B)-N(2B)$^{\#2}$ | 94.08(9) |
| N(1A)$^{\#1}$-Ni(1A)-N(2A) | 85.82(6) | N(1B)$^{\#2}$-Ni(2B)-N(2B) | 85.92(9) |
| N(1A)$^{\#1}$-Ni(1A)-O(1C)$^{\#1}$ | 88.11(5) | N(1B)$^{\#2}$-Ni(2B)-O(3C)$^{\#2}$ | 91.81(5) |
| N(1A)$^{\#1}$-Ni(1A)-O(1C) | 91.89(5) | N(1B)$^{\#2}$-Ni(2B)-O(3C) | 88.19(5) |
| N(1A)-Ni(1A)-N(2A)$^{\#1}$ | 85.82(6) | N(1B)-Ni(2B)-N(2B)$^{\#2}$ | 85.92(9) |
| N(1A)-Ni(1A)-N(2A) | 94.18(6) | N(1B)-Ni(2B)-N(2B) | 94.08(9) |
| N(1A)-Ni(1A)-O(1C)$^{\#1}$ | 91.89(5) | N(1B)-Ni(2B)-O(3C)$^{\#2}$ | 88.19(5) |
| N(1A)-Ni(1A)-O(1C) | 88.11(5) | N(1B)-Ni(2B)-O(3C) | 91.81(5) |
| N(2A)$^{\#1}$-Ni(1A)-N(2A) | 180.0 | N(2B)$^{\#2}$-Ni(2B)-N(2B) | 180 |
| N(2A)$^{\#1}$-Ni(1A)-O(1C)$^{\#1}$ | 90.51(6) | N(2B)$^{\#2}$-Ni(2B)-O(3C)$^{\#2}$ | 88.35(7) |
| N(2A)$^{\#1}$-Ni(1A)-O(1C) | 89.50(6) | N(2B)$^{\#2}$-Ni(2B)-O(3C) | 91.65(7) |
| N(2A)-Ni(1A)-O(1C)$^{\#1}$ | 89.49(6) | N(2B)-Ni(2B)-O(3C)$^{\#2}$ | 91.65(7) |
| N(2A)-Ni(1A)-O(1C) | 90.50(6) | N(2B)-Ni(2B)-O(3C) | 88.35(7) |
| O(1C)$^{\#1}$-Ni(1A)-O(1C) | 180.0 | O(3C)$^{\#2}$-Ni(2B)-O(3C) | 180.0 |

Symmetry transformations used to generate equivalent atoms:

#1 -x,-y+1,-z #2 -x+1/2,-y+1/2,-z+1

**Table S9**. Selected torsion angles [°] of **1-as (298 K)**.

| | |
|---|---|
| C(2C)-C(7C) : C(2C)$^{\#1}$ - C(2C)$^{\#1}$ | 44.232(54) |
| O(1C)-C(1C)-O(2C) : C(2C)-C(7C) | 65.123(126) |
| O(3C)-C(8C)-O(4C) : C(2C)-C(7C) | 9.818(83) |

Symmetry transformations used to generate equivalent atoms:

#1 -x, y, -z+1/2

**Table S10**. Hydrogen bonds for **1-as (298 K)** [Å and °].

| D-H···A | d(D-H) | d(H···A) | d(D···A) | ∠(DHA) |
|---|---|---|---|---|
| N(1A)-H(1A)...O(2C)$^{\#1}$ | 1.00 | 1.96 | 2.8674(19) | 152.9 |
| N(2A)-H(2A)...O(4C)$^{\#2}$ | 1.00 | 2.24 | 2.9874(19) | 132.2 |
| N(1B)-H(1B)...O(4C) | 1.00 | 2.02 | 2.923(2) | 152.3 |

Symmetry transformations used to generate equivalent atoms:

#1 -x,-y,-z #2 x,-y,z-1/2

**Table S11**. X-ray crystallographic data of **1-MeCN**.

| Compound | **1-MeCN (100 K)** | **1-MeCN (195 K)** |
|---|---|---|
| formula | $NiC_{28}H_{46}N_9O_4$ | $Ni_1C_{22}H_{37}N_6O_4$ |
| crystal system | *Monoclinic* | *Monoclinic* |
| space group | *C*2/*c* | *C*2/*c* |
| fw | 631.45 | 508.28 |
| *a*, Å | 29.377(6) | 29.313(6) |
| *b*, Å | 11.657(2) | 11.935(2) |
| *c*, Å | 22.227(4) | 22.254(5) |
| $\alpha$, deg | 90 | 90 |
| $\beta$, deg | 114.80(3) | 114.98(3) |
| $\gamma$, deg | 90 | 90 |
| *V*, Å $^3$ | 6909(3) | 7057(3) |
| *Z* | 8 | 8 |
| $\rho_{calcd}$, g cm$^{-3}$ | 1.214 | 0.957 |
| temp , K | 100(2) | 195(2) |
| $\lambda$, Å | 0.62998 | 0.62998 |
| $\mu$, mm$^{-1}$ | 0.438 | 0.417 |
| goodness-of-fit ($F^2$) | 1.064 | 1.115 |
| *F*(000) | 2696 | 2168 |
| reflections collected | 34930 | 35719 |
| independent reflections | 9335 [*R*(int) = 0.0225] | 9583 [*R*(int) = 0.0224] |
| completeness to $\theta_{max}$, % | 96.3% | 96.8% |
| data / parameters / restraints | 9335 / 12 / 479 | 9583 / 6 / 387 |
| $\theta$ range for data | 2.245 to 25.999 | 2.219 to 26.000 |
| diffraction limits (*h*, *k*, *l*) | -40≤*h*≤40, -16≤*k*≤16,-30≤*l*≤30 | -40≤*h*≤40, -16≤*k*≤16,-.30≤*l*≤30 |
| refinement method | Full-matrix least-squares on $F^2$ | Full-matrix least-squares on $F^2$ |
| $R_1$, $wR_2$ [$I>2\sigma(I)$] | $R_1$ = 0.0375[a], $wR_2$ = 0.1073[b] | $R_1$ = 0.0424[a], $wR_2$ = 0.1342[c] |
| $R_1$, $wR_2$ (all data) | $R_1$ = 0.0395[a], $wR_2$ = 0.1089[b] | $R_1$ = 0.0451[a], $wR_2$ = 0.1374[c] |
| largest peak, hole, eÅ $^{-3}$ | 0.515, -0.964 | 0.676, -0.591 |

[a] $R = \Sigma||F_O| - |F_C||/\Sigma|F_O|$. [b] $wR(F^2) = [\Sigma w(F_O^2 - F_C^2)^2/\Sigma w(F_O^2)^2]^{1/2}$ where $w = 1/[\sigma^2(F_O^2) + (0.0715P)^2 + (4.4334)P]$, $P = (F_O^2 + 2F_C^2)/3$. [c] $wR(F^2) = [\Sigma w(F_O^2 - F_C^2)^2/\Sigma w(F_O^2)^2]^{1/2}$ where $w = 1/[\sigma^2(F_O^2) + (0.0875P)^2 + (4.0099)P]$, $P = (F_O^2 + 2F_C^2)/3$.

**Table S12**. Selected bond distances [Å ] and angles [°] of **1-MeCN (100 K)**.

| | | | |
|---|---|---|---|
| Ni(1A)-N(1A)$^{\#1}$ | 2.0493(11) | Ni(2B)-N(1B1)$^{\#2}$ | 2.064(2) |
| Ni(1A)-N(1A) | 2.0494(11) | Ni(2B)-N(1B1) | 2.064(2) |
| Ni(1A)-N(2A)$^{\#1}$ | 2.0677(10) | Ni(2B)-N(2B1)$^{\#2}$ | 2.0616(18) |
| Ni(1A)-N(2A) | 2.0676(10) | Ni(2B)-N(2B1) | 2.0616(18) |
| Ni(1A)-O(1C)$^{\#1}$ | 2.1470(9) | Ni(2B)-O(3C)$^{\#2}$ | 2.1089(11) |
| Ni(1A)-O(1C) | 2.1470(9) | Ni(2B)-O(3C) | 2.1089(11) |
| | | | |
| N(1A)$^{\#1}$-Ni(1A)-N(1A) | 180.0 | N(1B1)$^{\#2}$-Ni(2B)-N(1B1) | 180.0 |
| N(1A)$^{\#1}$-Ni(1A)-N(2A)$^{\#1}$ | 94.16(4) | N(1B1)$^{\#2}$-Ni(2B)-N(2B1)$^{\#2}$ | 93.81(7) |
| N(1A)$^{\#1}$-Ni(1A)-N(2A) | 85.84(4) | N(1B1)$^{\#2}$-Ni(2B)-N(2B1) | 86.19(7) |
| N(1A)$^{\#1}$-Ni(1A)-O(1C)$^{\#1}$ | 88.97(4) | N(1B1)$^{\#2}$-Ni(2B)-O(3C)$^{\#2}$ | 92.83(6) |
| N(1A)$^{\#1}$-Ni(1A)-O(1C) | 91.03(4) | N(1B1)$^{\#2}$-Ni(2B)-O(3C) | 87.17(6) |
| N(1A)-Ni(1A)-N(2A)$^{\#1}$ | 85.84(4) | N(1B1)-Ni(2B)-N(2B1)$^{\#2}$ | 86.19(7) |
| N(1A)-Ni(1A)-N(2A) | 94.16(4) | N(1B1)-Ni(2B)-N(2B1) | 93.81(7) |
| N(1A)-Ni(1A)-O(1C)$^{\#1}$ | 91.03(4) | N(1B1)-Ni(2B)-O(3C)$^{\#2}$ | 87.17(6) |
| N(1A)-Ni(1A)-O(1C) | 88.98(4) | N(1B1)-Ni(2B)-O(3C) | 92.83(6) |
| N(2A)$^{\#1}$-Ni(1A)-N(2A) | 180.0 | N(2B1)$^{\#2}$-Ni(2B)-N(2B1) | 180.0 |
| N(2A)$^{\#1}$-Ni(1A)-O(1C)$^{\#1}$ | 89.07(5) | N(2B1)$^{\#2}$-Ni(2B)-O(3C)$^{\#2}$ | 87.52(7) |
| N(2A)$^{\#1}$-Ni(1A)-O(1C) | 90.93(5) | N(2B1)$^{\#2}$-Ni(2B)-O(3C) | 92.48(7) |
| N(2A)-Ni(1A)-O(1C)$^{\#1}$ | 90.93(5) | N(2B1)-Ni(2B)-O(3C)$^{\#2}$ | 92.48(7) |
| N(2A)-Ni(1A)-O(1C) | 89.07(5) | N(2B1)-Ni(2B)-O(3C) | 87.52(7) |
| O(1C)$^{\#1}$-Ni(1A)-O(1C) | 180.00(4) | O(3C)$^{\#2}$-Ni(2B)-O(3C) | 180.0 |

Symmetry transformations used to generate equivalent atoms:

#1 -x,-y+1,-z #2 -x+1/2,-y+1/2,-z+1

**Table S13**. Selected torsion angles [°] of **1-MeCN (100 K)**.

| | |
|---|---|
| C(2C)-C(7C) : C(2C)$^{\#1}$ - C(2C)$^{\#1}$ | 43.438(41) |
| O(1C)-C(1C)-O(2C) : C(2C)-C(7C) | 70.139(79) |
| O(3C)-C(8C)-O(4C) : C(2C)-C(7C) | 8.585(54) |

Symmetry transformations used to generate equivalent atoms:

#1 -x, y, -z+1/2

**Table S14**. Hydrogen bonds for **1-MeCN (100 K)** [Å and °].

| D-H···A | d(D-H) | d(H···A) | d(D···A) | ∠(DHA) |
|---|---|---|---|---|
| N(1A)-H(1A)...O(2C)$^{\#1}$ | 1.00 | 1.93 | 2.8646(14) | 153.5 |
| N(2A)-H(2A)...O(4C)$^{\#2}$ | 1.00 | 2.17 | 2.9477(14) | 133.4 |
| N(1B1)-H(1B)...O(4C) | 1.00 | 2.01 | 2.916(2) | 149.2 |

Symmetry transformations used to generate equivalent atoms:

#1 -x,-y,-z #2 x,-y,z-1/2

**Table S15**. Selected bond distances [Å ] and angles [°] of **1-MeCN (195 K)**.

| | | | |
|---|---|---|---|
| Ni(1A)-N(1A)$^{\#1}$ | 2.0490(13) | Ni(2B)-N(1B1)$^{\#2}$ | 2.086(10) |
| Ni(1A)-N(1A) | 2.0490(13) | Ni(2B)-N(1B) | 2.086(10) |
| Ni(1A)-N(2A)$^{\#1}$ | 2.0593(12) | Ni(2B)-N(2B)$^{\#2}$ | 2.0499(14) |
| Ni(1A)-N(2A) | 2.0592(12) | Ni(2B)-N(2B) | 2.0500(14) |
| Ni(1A)-O(1C)$^{\#1}$ | 2.1500(11) | Ni(2B)-O(3C)$^{\#2}$ | 2.1169(12) |
| Ni(1A)-O(1C) | 2.1500(11) | Ni(2B)-O(3C) | 2.1169(12) |
| | | | |
| N(1A)$^{\#1}$-Ni(1A)-N(1A) | 180.0 | N(1B1)$^{\#2}$-Ni(2B)-N(1B1) | 180.0 |
| N(1A)$^{\#1}$-Ni(1A)-N(2A)$^{\#1}$ | 94.21(6) | N(1B1)$^{\#2}$-Ni(2B)-N(2B)$^{\#2}$ | 99.36(18) |
| N(1A)$^{\#1}$-Ni(1A)-N(2A) | 85.78(6) | N(1B1)$^{\#2}$-Ni(2B)-N(2B) | 80.64(18) |
| N(1A)$^{\#1}$-Ni(1A)-O(1C)$^{\#1}$ | 88.89(4) | N(1B1)$^{\#2}$-Ni(2B)-O(3C)$^{\#2}$ | 92.3(3) |
| N(1A)$^{\#1}$-Ni(1A)-O(1C) | 91.11(4) | N(1B1)$^{\#2}$-Ni(2B)-O(3C) | 92.3(3) |
| N(1A)-Ni(1A)-N(2A)$^{\#1}$ | 94.78(6) | N(1B1)-Ni(2B)-N(2B)$^{\#2}$ | 80.64(18) |
| N(1A)-Ni(1A)-N(2A) | 94.22(6) | N(1B1)-Ni(2B)-N(2B) | 99.36(18) |
| N(1A)-Ni(1A)-O(1C)$^{\#1}$ | 91.11(4) | N(1B1)-Ni(2B)-O(3C)$^{\#2}$ | 92.3(3) |
| N(1A)-Ni(1A)-O(1C) | 88.89(4) | N(1B1)-Ni(2B)-O(3C) | 87.7(3) |
| N(2A)$^{\#1}$-Ni(1A)-N(2A) | 180.0 | N(2B)$^{\#2}$-Ni(2B)-N(2B) | 180.0 |
| N(2A)$^{\#1}$-Ni(1A)-O(1C)$^{\#1}$ | 90.36(5) | N(2B)$^{\#2}$-Ni(2B)-O(3C)$^{\#2}$ | 92.60(5) |
| N(2A)$^{\#1}$-Ni(1A)-O(1C) | 90.36(5) | N(2B)$^{\#2}$-Ni(2B)-O(3C) | 87.40(5) |
| N(2A)-Ni(1A)-O(1C)$^{\#1}$ | 90.36(5) | N(2B)-Ni(2B)-O(3C)$^{\#2}$ | 87.41(5) |
| N(2A)-Ni(1A)-O(1C) | 89.63(5) | N(2B)-Ni(2B)-O(3C) | 92.60(5) |
| O(1C)$^{\#1}$-Ni(1A)-O(1C) | 180.0 | O(3C)$^{\#2}$-Ni(2B)-O(3C) | 180.0 |

Symmetry transformations used to generate equivalent atoms:

#1 -x,-y+1,-z #2 -x+1/2,-y+1/2,-z+1

**Table S16**. Selected torsion angles [°] of **1-MeCN (195 K)**.

| | |
|---|---|
| C(2C)-C(7C) : C(2C)$^{\#1}$ - C(2C)$^{\#1}$ | 43.438(41) |
| O(1C)-C(1C)-O(2C) : C(2C)-C(7C) | 70.139(79) |
| O(3C)-C(8C)-O(4C) : C(2C)-C(7C) | 8.585(54) |

Symmetry transformations used to generate equivalent atoms:

#1 -x, y, -z+1/2

**Table S17**. Hydrogen bonds for **1-MeCN (195 K)** [Å and °].

| D-H···A | d(D-H) | d(H···A) | d(D···A) | ∠(DHA) |
|---|---|---|---|---|
| N(1A)-H(1A)...O(2C)$^{\#1}$ | 1.00 | 1.94 | 2.8718(17) | 153.5 |
| N(2A)-H(2A)...O(4C)$^{\#2}$ | 1.00 | 2.15 | 2.9246(17) | 133.1 |
| N(2B)-H(2B)...O(4C) | 1.00 | 1.99 | 2.906(2) | 150.9 |

Symmetry transformations used to generate equivalent atoms:

#1 -x,-y,-z #2 x,-y,z-1/2

**Table S18**. X-ray crystallographic data of **1-MeCN** and **1'**.

| Compound | **1-MeCN (298 K)** | **1' (195 K)** |
|---|---|---|
| formula | $Ni_1C_{22}H_{37}N_6O_4$ | $Ni_2C_{44}H_{74}N_{12}O_8$ |
| crystal system | *Monoclinic* | *Triclinic* |
| space group | *C2/c* | *P*-1 |
| fw | 508.28 | 1016.57 |
| *a*, Å | 29.202(6) | 21.820(4) |
| *b*, Å | 12.217(2) | 9.1860(18) |
| *c*, Å | 22.261(5) | 16.167(3) |
| $\alpha$, deg | 90 | 112.32(3) |
| $\beta$, deg | 115.08(3) | 101.56(3) |
| $\gamma$, deg | 90 | 100.54(3) |
| *V*, Å $^3$ | 7193(3) | 2814.2(12) |
| *Z* | 8 | 2 |
| $\rho_{calcd}$, g cm$^{-3}$ | 0.939 | 1.2000 |
| temp , K | 195(2) | 195(2) |
| $\lambda$, Å | 0.70001 | 0.79999 |
| $\mu$, mm$^{-1}$ | 0.567 | 0.995 |
| goodness-of-fit ($F^2$) | 0.969 | 0.999 |
| *F*(000) | 2168 | 1084 |
| reflections collected | 31598 | 12344 |
| independent reflections | 8629 [*R*(int) = 0.0725] | 6345 [*R*(int) = 0.0323] |
| completeness to $\theta_{max}$, % | 95.6% | 91.2% |
| data / parameters / restraints | 8629 / 0 / 304 | 6345 / 0 / 626 |
| $\theta$ range for data | 2.828 to 27.999 | 1.605 to 24.999 |
| diffraction limits (*h*, *k*, *l*) | -39≤*h*≤39, -16≤*k*≤16,-29≤*l*≤29 | -23≤*h*≤23, -9≤*k*≤9,-17≤*l*≤17 |
| refinement method | Full-matrix least-squares on $F^2$ | Full-matrix least-squares on $F^2$ |
| $R_1$, $wR_2$ [$I>2\sigma(I)$] | $R_1$ = 0.0749[a], $wR_2$ = 0.2111[b] | $R_1$ = 0.0792[a], $wR_2$ = 0.2151[b] |
| $R_1$, $wR_2$ (all data) | $R_1$ = 0.0944[a], $wR_2$ = 0.2272[b] | $R_1$ = 0.0946[a], $wR_2$ = 0.2267[b] |
| largest peak, hole, eÅ $^{-3}$ | 0.458, -0.596 | 1.036, -0.591 |

[a] $R = \Sigma||F_O| - |F_C||/\Sigma|F_O|$. [b] $wR(F^2) = [\Sigma w(F_O^2 - F_C^2)^2/\Sigma w(F_O^2)^2]^{1/2}$ where $w = 1/[\sigma^2(F_O^2) + (0.1624P)^2]$, $P = (F_O^2 + 2F_C^2)/3$. [c] $wR(F^2) = [\Sigma w(F_O^2 - F_C^2)^2/\Sigma w(F_O^2)^2]^{1/2}$ where $w = 1/[\sigma^2(F_O^2) + (0.1774P)^2]$, $P = (F_O^2 + 2F_C^2)/3$.

**Table S19**. Selected bond distances [Å ] and angles [°] of **1-MeCN (298 K)**.

| | | | |
|---|---|---|---|
| Ni(1A)-N(1A)$^{\#1}$ | 2.055(2) | Ni(2B)-N(1B)$^{\#2}$ | 2.052(2) |
| Ni(1A)-N(1A) | 2.055(2) | Ni(2B)-N(1B) | 2.052(2) |
| Ni(1A)-N(2A)$^{\#1}$ | 2.058(3) | Ni(2B)-N(2B)$^{\#2}$ | 2.059(4) |
| Ni(1A)-N(2A) | 2.058(3) | Ni(2B)-N(2B) | 2.059(4) |
| Ni(1A)-O(1C)$^{\#1}$ | 2.1531(18) | Ni(2B)-O(3C)$^{\#2}$ | 2.124(2) |
| Ni(1A)-O(1C) | 2.1531(18) | Ni(2B)-O(3C) | 2.124(2) |
| | | | |
| N(1A)$^{\#1}$-Ni(1A)-N(1A) | 180.0 | N(1B)$^{\#2}$-Ni(2B)-N(1B) | 180.0 |
| N(1A)$^{\#1}$-Ni(1A)-N(2A)$^{\#1}$ | 94.10(11) | N(1B)$^{\#2}$-Ni(2B)-N(2B)$^{\#2}$ | 93.66(15) |
| N(1A)$^{\#1}$-Ni(1A)-N(2A) | 85.91(11) | N(1B)$^{\#2}$-Ni(2B)-N(2B) | 86.34(15) |
| N(1A)$^{\#1}$-Ni(1A)-O(1C)$^{\#1}$ | 90.08(9) | N(1B)$^{\#2}$-Ni(2B)-O(3C)$^{\#2}$ | 92.46(9) |
| N(1A)$^{\#1}$-Ni(1A)-O(1C) | 89.92(9) | N(1B)$^{\#2}$-Ni(2B)-O(3C) | 87.54(9) |
| N(1A)-Ni(1A)-N(2A)$^{\#1}$ | 82.90(11) | N(1B)-Ni(2B)-N(2B)$^{\#2}$ | 86.34(15) |
| N(1A)-Ni(1A)-N(2A) | 94.09(11) | N(1B)-Ni(2B)-N(2B) | 93.66(15) |
| N(1A)-Ni(1A)-O(1C)$^{\#1}$ | 89.92(9) | N(1B)-Ni(2B)-O(3C)$^{\#2}$ | 87.54(9) |
| N(1A)-Ni(1A)-O(1C) | 90.08(9) | N(1B)-Ni(2B)-O(3C) | 92.46(9) |
| N(2A)$^{\#1}$-Ni(1A)-N(2A) | 180.0 | N(2B)$^{\#2}$-Ni(2B)-N(2B) | 180.0 |
| N(2A)$^{\#1}$-Ni(1A)-O(1C)$^{\#1}$ | 88.97(9) | N(2B)$^{\#2}$-Ni(2B)-O(3C)$^{\#2}$ | 88.07(12) |
| N(2A)$^{\#1}$-Ni(1A)-O(1C) | 91.03(9) | N(2B)$^{\#2}$-Ni(2B)-O(3C) | 91.93(12) |
| N(2A)-Ni(1A)-O(1C)$^{\#1}$ | 91.03(9) | N(2B)-Ni(2B)-O(3C)$^{\#2}$ | 91.93(12) |
| N(2A)-Ni(1A)-O(1C) | 88.97(9) | N(2B)-Ni(2B)-O(3C) | 88.07(12) |
| O(1C)$^{\#1}$-Ni(1A)-O(1C) | 180.0 | O(3C)$^{\#2}$-Ni(2B)-O(3C) | 180.0 |

Symmetry transformations used to generate equivalent atoms:

#1 -x,-y+1,-z #2 -x+1/2,-y+1/2,-z+1

**Table S20**. Selected torsion angles [°] of **1-MeCN (298 K)**.

| | |
|---|---|
| C(2C)-C(7C) : C(2C)$^{\#1}$ - C(2C)$^{\#1}$ | 44.146(80) |
| O(1C)-C(1C)-O(2C) : C(2C)-C(7C) | 68.432(184) |
| O(3C)-C(8C)-O(4C) : C(2C)-C(7C) | 8.948(127) |

Symmetry transformations used to generate equivalent atoms:

#1 -x, y, -z+1/2

**Table S21**. Hydrogen bonds for **1-MeCN (298 K)** [Å and °].

| D-H···A | d(D-H) | d(H···A) | d(D···A) | ∠(DHA) |
|---|---|---|---|---|
| N(2A)-H(2A)...O(2C)$^{\#1}$ | 1.00 | 1.96 | 2.868(3) | 153.3 |
| N(1A)-H(1A)...O(4C)$^{\#2}$ | 1.00 | 2.19 | 2.942(3) | 132.9 |
| N(1B)-H(1B)...O(4C) | 1.00 | 2.00 | 2.899(3) | 152.3 |

Symmetry transformations used to generate equivalent atoms:

#1 -x,-y,-z #2 x,-y,z-1/2

**Table S22**. Selected bond distances [Å] and angles [°] of **1' (195 K)**.

| | | | |
|---|---|---|---|
| Ni(1A)-N(1A)$^{\#1}$ | 2.048(6) | Ni(3C)-N(1C)$^{\#3}$ | 2.056(5) |
| Ni(1A)-N(1A) | 2.048(6) | Ni(3C)-N(1C) | 2.056(5) |
| Ni(1A)-N(2A)$^{\#1}$ | 2.047(5) | Ni(3C)-N(2C)$^{\#3}$ | 2.058(5) |
| Ni(1A)-N(2A) | 2.047(5) | Ni(3C)-N(2C) | 2.058(5) |
| Ni(1A)-O(1E)$^{\#1}$ | 2.169(4) | Ni(3C)-O(5E)$^{\#3}$ | 2.136(4) |
| Ni(1A)-O(1E) | 2.169(4) | Ni(3C)-O(5E) | 2.136(4) |
| Ni(2B)-N(1B)$^{\#2}$ | 2.053(5) | Ni(4D)-N(1D)$^{\#4}$ | 2.039(5) |
| Ni(2B)-N(1B) | 2.053(5) | Ni(4D)-N(1D) | 2.039(5) |
| Ni(2B)-N(2B)$^{\#2}$ | 2.053(5) | Ni(4D)-N(2D)$^{\#4}$ | 2.046(5) |
| Ni(2B)-N(2B) | 2.053(5) | Ni(4D)-N(2D) | 2.046(5) |
| Ni(2B)-O(3E)$^{\#2}$ | 2.125(4) | Ni(4D)-O(7E)$^{\#4}$ | 2.123(4) |
| Ni(2B)-O(3E) | 2.125(4) | Ni(4D)-O(7E) | 2.123(4) |
| | | | |
| N(1A)$^{\#1}$-Ni(1A)-N(1A) | 180.0 | N(1C)$^{\#3}$-Ni(3C)-N(1C) | 180.0 |
| N(1A)$^{\#1}$-Ni(1A)-N(2A)$^{\#1}$ | 94.6(2) | N(1C)$^{\#3}$-Ni(3C)-N(2C)$^{\#3}$ | 94.2(2) |
| N(1A)$^{\#1}$-Ni(1A)-N(2A) | 85.4(2) | N(1C)$^{\#3}$-Ni(3C)-N(2C) | 85.8(2) |
| N(1A)$^{\#1}$-Ni(1A)-O(1E)$^{\#1}$ | 92.65(18) | N(1C)$^{\#3}$-Ni(3C)-O(5E)$^{\#3}$ | 88.54(17) |
| N(1A)$^{\#1}$-Ni(1A)-O(1E) | 87.35(18) | N(1C)$^{\#3}$-Ni(3C)-O(5E) | 91.46(17) |
| N(1A)-Ni(1A)-N(2A)$^{\#1}$ | 85.4(2) | N(1C)-Ni(3C)-N(2C)$^{\#3}$ | 85.8(2) |
| N(1A)-Ni(1A)-N(2A) | 94.6(2) | N(1C)-Ni(3C)-N(2C) | 94.2(2) |
| N(1A)-Ni(1A)-O(1E)$^{\#1}$ | 92.65(18) | N(1C)-Ni(3C)-O(5E)$^{\#3}$ | 91.46(17) |
| N(1A)-Ni(1A)-O(1E) | 87.35(18) | N(1C)-Ni(3C)-O(5E) | 88.54(17) |
| N(2A)$^{\#1}$-Ni(1A)-N(2A) | 180.0 | N(2C)$^{\#3}$-Ni(3C)-N(2C) | 180.0 |
| N(2A)$^{\#1}$-Ni(1A)-O(1E)$^{\#1}$ | 85.81(19) | N(2C)$^{\#3}$-Ni(3C)-O(5E)$^{\#3}$ | 92.73(17) |
| N(2A)$^{\#1}$-Ni(1A)-O(1E) | 94.19(19) | N(2C)$^{\#3}$-Ni(3C)-O(5E) | 87.27(17) |
| N(2A)-Ni(1A)-O(1E)$^{\#1}$ | 94.19(19) | N(2C)-Ni(3C)-O(5E)$^{\#3}$ | 87.27(17) |
| N(2A)-Ni(1A)-O(1E) | 85.81(19) | N(2C)-Ni(3C)-O(5E) | 92.73(17) |
| O(1E)$^{\#1}$-Ni(1A)-O(1E) | 180.0 | O(5E)$^{\#3}$-Ni(3C)-O(5E) | 180.0 |

| | | | |
|---|---|---|---|
| N(1B)$^{\#2}$-Ni(2B)-N(1B) | 180.0 | N(1D)$^{\#4}$-Ni(4D)-N(1D) | 180.0 |
| N(1B)$^{\#2}$-Ni(2B)-N(2B)$^{\#2}$ | 93.7(2) | N(1D)$^{\#4}$-Ni(4D)-N(2D)$^{\#4}$ | 93.2(2) |
| N(1B)$^{\#2}$-Ni(2B)-N(2B) | 86.3(2) | N(1D)$^{\#4}$-Ni(4D)-N(2D) | 86.8(2) |
| N(1B)$^{\#2}$-Ni(2B)-O(3E)$^{\#2}$ | 91.17(18) | N(1D)$^{\#4}$-Ni(4D)-O(7E)$^{\#4}$ | 91.90(19) |
| N(1B)$^{\#2}$-Ni(2B)-O(3E) | 88.83(18) | N(1D)$^{\#4}$-Ni(4D)-O(7E) | 88.10(19) |
| N(1B)-Ni(2B)-N(2B)$^{\#2}$ | 86.3(2) | N(1D)-Ni(4D)-N(2D)$^{\#4}$ | 86.8(2) |
| N(1B)-Ni(2B)-N(2B) | 93.7(2) | N(1D)-Ni(4D)-N(2D) | 93.2(2) |
| N(1B)-Ni(2B)-O(3E)$^{\#2}$ | 88.83(18) | N(1D)-Ni(4D)-O(7E)$^{\#4}$ | 88.10(19) |
| N(1B)-Ni(2B)-O(3E) | 91.17(18) | N(1D)-Ni(4D)-O(7E) | 91.90(19) |
| N(2B)$^{\#2}$-Ni(2B)-N(2B) | 180.0 | N(2D)$^{\#4}$-Ni(4D)-N(2D) | 180.0 |
| N(2B)$^{\#2}$-Ni(2B)-O(3E)$^{\#2}$ | 92.18(17) | N(2D)$^{\#4}$-Ni(4D)-O(7E)$^{\#4}$ | 89.05(17) |
| N(2B)$^{\#2}$-Ni(2B)-O(3E) | 87.82(17) | N(2D)$^{\#4}$-Ni(4D)-O(7E) | 90.95(17) |
| N(2B)-Ni(2B)-O(3E)$^{\#2}$ | 87.82(17) | N(2D)-Ni(4D)-O(7E)$^{\#4}$ | 90.95(17) |
| N(2B)-Ni(2B)-O(3E) | 92.18(17) | N(2D)-Ni(4D)-O(7E) | 89.05(17) |
| O(3E)$^{\#2}$-Ni(2B)-O(3E) | 180.0 | O(7E)$^{\#4}$-Ni(4D)-O(7E) | 180.0 |

Symmetry transformations used to generate equivalent atoms:
#1 -x,-y+1,-z #2 -x+1,-y+1,-z #3 -x+1,-y+2,-z+1 #4 -x,-y+1,-z+1

**Table S23**. Selected torsion angles [°] of **1' (195 K)**.

| | |
|---|---|
| C(2E) - C(7E) : C(15E) - C(10E) | 43.616(176) |
| O(1E) - C(1E) - O(2E) : C(2E) - C(7E) | 45.226(415) |
| O(3E) - C(8E) - O(4E) : C(2E) - C(7E) | 12.293(416) |
| O(5E) - C(9E) - O(6E) : C(15E) - C(10E) | 69.547(467) |
| O(7E) - C(16E) - O(8E) : C(15E) - C(10E) | 19.347(926) |

**Table S24**. Hydrogen bonds for **1' (195 K)** [Å and °].

| D-H···A | d(D-H) | d(H···A) | d(D···A) | ∠(DHA) |
|---|---|---|---|---|
| N(1A)-H(1A)...O(2E) | 1.00 | 1.92 | 2.836(6) | 150.4 |
| N(2B)-H(2B)...O(4E) | 1.00 | 2.02 | 2.944(6) | 151.7 |
| N(2C)-H(2C)...O(6E) | 1.00 | 1.96 | 2.878(6) | 151.8 |
| N(1C)-H(1C)...O(4E) | 1.00 | 2.25 | 2.998(7) | 130.1 |
| N(2D)-H(2D)...O(8E)$^{\#1}$ | 1.00 | 1.96 | 2.888(6) | 153.3 |

Symmetry transformations used to generate equivalent atoms:

#1 -x,-y+1,-z+1

**Table S25**. Gas sorption data of **1**.

| Gas | *T* (K) | Surface area ($m^2/g$)[a] | Total pore volume ($cm^3/g$)[b] | wt% gas | mmol of gas/g of host |
|---|---|---|---|---|---|
| $N_2$ | 77 | 7.47 | 3.80 | 3.08 | 1.10 |
| $H_2$ | 77 | | | $6.61 \times 10^{-2}$ | $3.28 \times 10^{-1}$ |
| $CO_2$ | 195 | | | 45.6 | 10.4 |
| | 273 | | | 3.97 | $9.02 \times 10^{-1}$ |
| | 298 | | | 1.12 | $2.54 \times 10^{-1}$ |
| | 303[c] | | | 28.5[d] | 6.48[d] |

[a]The specific surface area was calculated by Brunauer-Emmet-Teller method. [b]Total pore volume was calculated at $P/P_0 = 0.99$. [c]High pressure gas adsorption of $CO_2$ at 303 K up to 45 bar. [d]The capacity were obtained at 45 bar.

**Table S26**. Selected bond distances [Å] and angles [°] of **2-as (100 K)**.

| | | | |
|---|---|---|---|
| Ni(1)-N(1)$^{\#1}$ | 2.053(4) | Ni(2)-N(4)$^{\#2}$ | 2.058(4) |
| Ni(1)-N(1) | 2.053(4) | Ni(2)-N(4) | 2.058(4) |
| Ni(1)-N(2)$^{\#1}$ | 2.066(3) | Ni(2)-N(5)$^{\#2}$ | 2.060(4) |
| Ni(1)-N(2) | 2.066(3) | Ni(2)-N(5) | 2.060(4) |
| Ni(1)-O(1)$^{\#1}$ | 2.097(3) | Ni(2)-O(3)$^{\#2}$ | 2.113(3) |
| Ni(1)-O(1) | 2.097(3) | Ni(2)-O(3) | 2.113 (3) |
| | | | |
| N(1)$^{\#1}$-Ni(1)-N(1) | 180.0(2) | N(4)$^{\#2}$-Ni(2)-N(4) | 179.999(1) |
| N(1)$^{\#1}$-Ni(1)-N(2)$^{\#1}$ | 93.75(16) | N(4)$^{\#2}$-Ni(2)-N(5)$^{\#2}$ | 94.07(17) |
| N(1)-Ni(1)-N(2)$^{\#1}$ | 86.25(16) | N(4)-Ni(2)-N(5)$^{\#2}$ | 85.94(17) |
| N(1)$^{\#1}$-Ni(1)-N(2) | 86.25(16) | N(4)$^{\#2}$-Ni(2)-N(5) | 85.94(17) |
| N(1)-Ni(1)-N(2) | 93.75(16) | N(4)-Ni(2)-N(5) | 94.06(17) |
| N(2)$^{\#1}$-Ni(1)-N(2) | 180.0 | N(5)$^{\#2}$-Ni(2)-N(5) | 180.0 |
| N(1)$^{\#1}$-Ni(1)-O(1)$^{\#1}$ | 86.47(14) | N(4)$^{\#2}$-Ni(2)-O(3)$^{\#2}$ | 88.64(15) |
| N(1)-Ni(1)-O(1)$^{\#1}$ | 93.53(14) | | |
| N(2)$^{\#1}$-Ni(1)-O(1)$^{\#1}$ | 92.09(13) | N(4)-Ni(2)-O(3)$^{\#2}$ | 91.36(15) |
| N(2)-Ni(1)-O(1)$^{\#1}$ | 87.91(13) | N(5)$^{\#2}$-Ni(2)-O(3)$^{\#2}$ | 93.33(14) |
| N(1)$^{\#1}$-Ni(1)-O(1) | 93.53(14) | N(5)-Ni(2)-O(3)$^{\#2}$ | 86.67(14) |
| N(1)-Ni(1)-O(1) | 86.47(14) | N(4)$^{\#2}$-Ni(2)-O(3) | 91.36(15) |
| N(2)$^{\#1}$-Ni(1)-O(1) | 87.91(13) | N(4)-Ni(2)-O(3) | 88.64(15) |
| N(2)-Ni(1)-O(1) | 92.09(13) | N(5)$^{\#2}$-Ni(2)-O(3) | 86.67(14) |
| O(1)$^{\#1}$-Ni(1)-O(1) | 180.0 | N(5)-Ni(2)-O(3) | 93.33(14) |

Symmetry transformations used to generate equivalent atoms:

#1 -x,-y+2,-z #2 -x+1,-y+1/2,-z

**Table S27**. Selected bond distances [Å ] and angles [°] of **3-as (100 K)**.

| | | | |
|---|---|---|---|
| Ni(1)-N(2) | 2.052(5) | Ni(2)-N(4)$^{\#2}$ | 2.059(4) |
| Ni(1)-N(2)$^{\#1}$ | 2.052(5) | Ni(2)-N(4) | 2.059(4) |
| Ni(1)-N(1)$^{\#1}$ | 2.064(4) | Ni(2)-N(5)$^{\#2}$ | 2.067(4) |
| Ni(1)-N(1) | 2.064(4) | Ni(2)-N(5) | 2.067(4) |
| Ni(1)-O(1)$^{\#1}$ | 2.104(4) | Ni(2)-O(3)$^{\#2}$ | 2.110(3) |
| Ni(1)-O(1) | 2.104(4) | Ni(2)-O(3) | 2.110(3) |
| | | | |
| N(2)-Ni(1)-N(2)$^{\#1}$ | 180.0 | N(4)$^{\#2}$-Ni(2)-N(4) | 180.0 |
| N(2)-Ni(1)-N(1)$^{\#1}$ | 86.19(17) | N(4)$^{\#2}$-Ni(2)-N(5)$^{\#2}$ | 93.45(16) |
| N(2)$^{\#1}$-Ni(1)-N(1)$^{\#1}$ | 93.81(17) | N(4)-Ni(2)-N(5)$^{\#2}$ | 86.55(16) |
| N(2)-Ni(1)-N(1) | 93.82(17) | N(4)$^{\#2}$-Ni(2)-N(5) | 86.55(16) |
| N(2)$^{\#1}$-Ni(1)-N(1) | 86.18(17) | N(4)-Ni(2)-N(5) | 93.45(16) |
| N(1)$^{\#1}$-Ni(1)-N(1) | 180.0 | N(5)$^{\#2}$-Ni(2)-N(5) | 180.00(12) |
| N(2)-Ni(1)-O(1)$^{\#1}$ | 86.40(15) | N(4)$^{\#2}$-Ni(2)-O(3)$^{\#2}$ | 87.15(12) |
| N(2)$^{\#1}$-Ni(1)-O(1)$^{\#1}$ | 93.60(15) | N(4)-Ni(2)-O(3)$^{\#2}$ | 92.86(12) |
| N(1)$^{\#1}$-Ni(1)-O(1)$^{\#1}$ | 87.52(15) | N(5)$^{\#2}$-Ni(2)-O(3)$^{\#2}$ | 91.40(15) |
| N(1)-Ni(1)-O(1)$^{\#1}$ | 92.48(15) | N(5)-Ni(2)-O(3)$^{\#2}$ | 88.60(15) |
| N(2)-Ni(1)-O(1) | 93.60(15) | N(4)$^{\#2}$-Ni(2)-O(3) | 92.85(12) |
| N(2)$^{\#1}$-Ni(1)-O(1) | 86.40(15) | N(4)-Ni(2)-O(3) | 87.14(12) |
| N(1)$^{\#1}$-Ni(1)-O(1) | 92.48(15) | N(5)$^{\#2}$-Ni(2)-O(3) | 88.60(15) |
| N(1)-Ni(1)-O(1) | 87.52(15) | N(5)-Ni(2)-O(3) | 91.40(15) |
| O(1)$^{\#1}$-Ni(1)-O(1) | 180.0 | O(3)$^{\#2}$-Ni(2)-O(3) | 180.0 |

Symmetry transformations used to generate equivalent atoms: #1 –x+1,-y,-z #2 -x+2,-y+1,-z

**Table S28**. Gas sorption data of **2** and **3**.

| Gas | *T* (K) | Surface area ($m^2/g$)[a] | | Total pore volume ($cm^3/g$)[b] | | wt% gas | | mmol of gas/g host | |
|---|---|---|---|---|---|---|---|---|---|
| | | **1'** | **2'** | **1'** | **2'** | **1'** | **2'** | **1'** | **2'** |
| $N_2$ | 77 | 6.7 | 30 | $3.2 \times 10^{-2}$ | $8.1 \times 10^{-2}$ | 2.6 | 6.5 | 0.93 | 2.3 |
| $H_2$ | 77 | | | | | 0.02 | 0.05 | 0.10 | 0.24 |
| $CO_2$ | 195 | | | | | 2.5 | 2.7 | 0.57 | 0.62 |
| | 273 | | | | | 0.29 | 0.81 | 0.07 | 0.18 |
| | 298 | | | | | 0.17 | 0.54 | 0.04 | 0.12 |

[a]The specific surface area was calculated by Brunauer-Emmet-Teller method. [b]Total pore volume was calculated at $P/P_0 = 0.98$.

**Table S29**. Selected bond distances [Å] and angles [°] of **4-as (100 K)**.

| | | | |
|---|---|---|---|
| Ni(1)-N(1A)$^{\#1}$ | 2.055(3) | Ni(1)-N(1A) | 2.055(3) |
| Ni(1)-N(2A)$^{\#1}$ | 2.058(3) | Ni(1)-N(2A) | 2.058(3) |
| Ni(1)-O(1B)$^{\#1}$ | 2.1085(18) | Ni(1)-O(1B) | 2.1085(18) |
| | | | |
| N(1A)$^{\#1}$-Ni(1)-N(1A) | 180.00(16) | N(2A)$^{\#1}$-Ni(1)-N(2A) | 180.0 |
| N(1A)$^{\#1}$-Ni(1)-N(2A)$^{\#1}$ | 94.34(17) | N(2A)$^{\#1}$-Ni(1)-N(1A) | 85.66(17) |
| N(1A)$^{\#1}$-Ni(1)-N(2A) | 85.66(17) | N(2A)-Ni(1)-N(1A) | 94.34(17) |
| N(1A)$^{\#1}$-Ni(1)-O(1B)$^{\#1}$ | 93.72(9) | N(2A)$^{\#1}$-Ni(1)-O(1B)$^{\#1}$ | 88.35(10) |
| N(1A)$^{\#1}$-Ni(1)-O(1B) | 86.28(9) | N(2A)$^{\#1}$-Ni(1)-O(1B) | 91.65(10) |
| N(1A)-Ni(1)-O(1B)$^{\#1}$ | 86.28(9) | N(2A)-Ni(1)-O(1B)$^{\#1}$ | 91.65(10) |
| N(1A)-Ni(1)-O(1B) | 93.72(9) | N(2A)-Ni(1)-O(1B) | 88.35(10) |
| O(1B)$^{\#1}$-Ni(1)-O(1B) | 180.00(6) | | |

Symmetry transformations used to generate equivalent atoms:

#1 –x+1,-y,-z+1

**Table S30**. Selected bond distances [Å ] and angles [°] of **5-as (100 K)**.

| | | | |
|---|---|---|---|
| Ni(1)-N(1A)$^{\#1}$ | 2.066(2) | Ni(1)-N(1A) | 2.066(2) |
| Ni(1)-N(2A)$^{\#1}$ | 2.064(2) | Ni(1)-N(2A) | 2.064(2) |
| Ni(1)-O(1B)$^{\#1}$ | 2.1081(16) | Ni(1)-O(1B) | 2.1080(16) |
| | | | |
| N(1A)$^{\#1}$-Ni(1)-N(1A) | 180.00(10) | N(2A)$^{\#1}$-Ni(1)-N(2A) | 180.0 |
| N(1A)$^{\#1}$-Ni(1)-N(2A)$^{\#1}$ | 93.69(9) | N(2A)$^{\#1}$-Ni(1)-N(1A) | 86.31(9) |
| N(1A)$^{\#1}$-Ni(1)-N(2A) | 86.31(9) | N(2A)-Ni(1)-N(1A) | 93.69(9) |
| N(1A)$^{\#1}$-Ni(1)-O(1B)$^{\#1}$ | 93.44(8) | N(2A)$^{\#1}$-Ni(1)-O(1B)$^{\#1}$ | 88.08(9) |
| N(1A)$^{\#1}$-Ni(1)-O(1B) | 86.57(8) | N(2A)$^{\#1}$-Ni(1)-O(1B) | 91.92(9) |
| N(1A)-Ni(1)-O(1B)$^{\#1}$ | 86.56(8) | N(2A)-Ni(1)-O(1B)$^{\#1}$ | 91.92(9) |
| N(1A)-Ni(1)-O(1B) | 93.43(8) | N(2A)-Ni(1)-O(1B) | 88.08(9) |
| O(1B)$^{\#1}$-Ni(1)-O(1B) | 180.00(6) | | |

Symmetry transformations used to generate equivalent atoms:

#1 –x+1,-y+2,-z+2

**Table S31**. Gas sorption data of $\mathbf{4}_{\mathbf{xstal}}$.

| Gas | *T* (K) | Surface area ($m^2/g$)[a] | Total pore volume ($cm^3/g$)[b] | Adsorbed gas | |
|---|---|---|---|---|---|
| | | | | wt% | mmol/g |
| $N_2$ | 77 | 7.54 | $1.34 \times 10^{-2}$ | 1.1 | 0.39 |
| $H_2$ | 77 | | | 0.037 | 0.18 |
| $CO_2$ | 195 | | | 0.73 | 0.17 |
| | 273 | | | 1.5 | 0.35 |
| | 298 | | | 2.7 | 0.61 |

[a]The specific surface area was calculated by Brunauer-Emmet-Teller method. [b]Total pore volume was calculated at $P/P_0 = 0.990$.

**Table S31**. Gas sorption data of $\mathbf{4_{grind}}$.

| Gas | *T* (K) | Surface area ($m^2/g$)[a] | Total pore volume ($cm^3/g$)[b] | Adsorbed gas | |
|---|---|---|---|---|---|
| | | | | wt% | mmol/g |
| $N_2$ | 77 | 9.04 | $4.98 \times 10^{-2}$ | 4.1 | 1.5 |
| $H_2$ | 77 | | | 0.051 | 0.25 |
| $CO_2$ | 195 | | | 2.5 | 0.56 |
| | 273 | | | 3.9 | 0.90 |
| | 298 | | | 5.9 | 1.4 |

[a]The specific surface area was calculated by Brunauer-Emmet-Teller method. [b]Total pore volume was calculated at $P/P_0 = 0.990$.

**Table S32**. Gas sorption data of **5**.

| Gas | *T* (K) | Adsorbed gas | |
|---|---|---|---|
| | | wt% | mmol/g |
| $N_2$ | 77 | 0.50 | 0.18 |
| $H_2$ | 77 | 0.0074 | 0.037 |
| $CO_2$ | 195 | 9.3 | 2.1 |
| | 273 | 2.0 | 0.45 |
| | 298 | 1.1 | 0.24 |

## VI. References


1. Sumida, K.; Rogow, D. L.; Mason, J. A.; McDonald, T. M.; Bloch, E. D.; Herm, Z. R.; Bae, T.-H.; Long, J. R., Carbon Dioxide Capture in Metal–Organic Frameworks. *Chemical Reviews* **2011,** *112* (2), 724-781.
2. Murray, L. J.; Dinca, M.; Long, J. R., Hydrogen storage in metal-organic frameworks. *Chemical Society Reviews* **2009,** *38* (5), 1294-1314.
3. Lee, J.; Farha, O. K.; Roberts, J.; Scheidt, K. A.; Nguyen, S. T.; Hupp, J. T., Metal-organic framework materials as catalysts. *Chemical Society Reviews* **2009,** *38* (5), 1450-1459.
4. Bloch, E. D.; Queen, W. L.; Krishna, R.; Zadrozny, J. M.; Brown, C. M.; Long, J. R., Hydrocarbon separations in a metal-organic framework with open iron(II) coordination sites. *Science* **2012,** *335* (6076), 1606-10.
5. Kim, T. K.; Lee, J. H.; Moon, D.; Moon, H. R., Luminescent Li-Based Metal–Organic Framework Tailored for the Selective Detection of Explosive Nitroaromatic Compounds: Direct Observation of Interaction Sites. *Inorganic Chemistry* **2012,** *52* (2), 589-595.
6. Yanai, N.; Uemura, T.; Inoue, M.; Matsuda, R.; Fukushima, T.; Tsujimoto, M.; Isoda, S.; Kitagawa, S., Guest-to-host transmission of structural changes for stimuli-responsive adsorption property. *J Am Chem Soc* **2012,** *134* (10), 4501-4.
7. Park, J.; Yuan, D.; Pham, K. T.; Li, J.-R.; Yakovenko, A.; Zhou, H.-C., Reversible Alteration of CO2 Adsorption upon Photochemical or Thermal Treatment in a Metal–Organic Framework. *Journal of the American Chemical Society* **2011,** *134* (1), 99-102.
8. Bloch, W. M.; Babarao, R.; Hill, M. R.; Doonan, C. J.; Sumby, C. J., Post-synthetic Structural Processing in a Metal–Organic Framework Material as a Mechanism for Exceptional CO2/N2 Selectivity. *Journal of the American Chemical Society* **2013,** *135* (28), 10441-10448.
9. Choi, H.-S.; Suh, M. P., Highly Selective CO2 Capture in Flexible 3D Coordination Polymer Networks. *Angewandte Chemie International Edition* **2009,** *48* (37), 6865-6869.
10. Demessence, A.; Long, J. R., Selective gas adsorption in the flexible metal-organic frameworks Cu(BDTri)L (L=DMF, DEF). *Chemistry* **2010,** *16* (20), 5902-8.
11. Yanai, N.; Kitayama, K.; Hijikata, Y.; Sato, H.; Matsuda, R.; Kubota, Y.; Takata, M.; Mizuno, M.; Uemura, T.; Kitagawa, S., Gas detection by structural variations of fluorescent guest molecules in a flexible porous coordination polymer. *Nature materials* **2011,** *10* (10), 787-93.
12. Bureekaew, S.; Sato, H.; Matsuda, R.; Kubota, Y.; Hirose, R.; Kim, J.; Kato, K.; Takata, M.; Kitagawa, S., Control of Interpenetration for Tuning Structural Flexibility Influences Sorption Properties. *Angewandte Chemie International Edition* **2010,** *49* (42), 7660-7664.
13. Seo, J.; Matsuda, R.; Sakamoto, H.; Bonneau, C.; Kitagawa, S., A Pillared-Layer

Coordination Polymer with a Rotatable Pillar Acting as a Molecular Gate for Guest Molecules. *Journal of the American Chemical Society* **2009,** *131* (35), 12792-12800.

14. Kitagawa, S.; Uemura, K., Dynamic porous properties of coordination polymers inspired by hydrogen bonds. *Chem Soc Rev* **2005,** *34* (2), 109-19.
15. Hauptvogel, I. M.; Biedermann, R.; Klein, N.; Senkovska, I.; Cadiau, A.; Wallacher, D.; Feyerherm, R.; Kaskel, S., Flexible and Hydrophobic Zn-Based Metal–Organic Framework. *Inorganic Chemistry* **2011,** *50* (17), 8367-8374.
16. Yang, S.; Lin, X.; Lewis, W.; Suyetin, M.; Bichoutskaia, E.; Parker, J. E.; Tang, C. C.; Allan, D. R.; Rizkallah, P. J.; Hubberstey, P.; Champness, N. R.; Mark Thomas, K.; Blake, A. J.; Schröder, M., A partially interpenetrated metal–organic framework for selective hysteretic sorption of carbon dioxide. *Nature materials* **2012,** *11* (8), 710-716.
17. Kitaura, R.; Seki, K.; Akiyama, G.; Kitagawa, S., Porous coordination-polymer crystals with gated channels specific for supercritical gases. *Angew Chem Int Edit* **2003,** *42* (4), 428-431.
18. Hyun, S.-m.; Kim, T. K.; Kim, Y. K.; Moon, D.; Moon, H. R., Guest-driven structural flexibility of 2D coordination polymers: Synthesis, structural characterizations, and gas sorption properties. *Inorganic Chemistry Communications* **2013,** *33* (0), 52-56.
19. Ferey, G.; Serre, C., Large breathing effects in three-dimensional porous hybrid matter: facts, analyses, rules and consequences. *Chem Soc Rev* **2009,** *38* (5), 1380-99.
20. Tanaka, D.; Nakagawa, K.; Higuchi, M.; Horike, S.; Kubota, Y.; Kobayashi, T. C.; Takata, M.; Kitagawa, S., Kinetic gate-opening process in a flexible porous coordination polymer. *Angewandte Chemie* **2008,** *47* (21), 3914-8.
21. Serre, C.; Millange, F.; Thouvenot, C.; Noguès, M.; Marsolier, G.; Louër, D.; Férey, G., Very Large Breathing Effect in the First Nanoporous Chromium(III)-Based Solids: MIL-53 or CrIII(OH)·{O2C−C6H4−CO2}·{HO2C−C6H4−CO2H}x·H2Oy. *Journal of the American Chemical Society* **2002,** *124* (45), 13519-13526.
22. Serre, C.; Bourrelly, S.; Vimont, A.; Ramsahye, N. A.; Maurin, G.; Llewellyn, P. L.; Daturi, M.; Filinchuk, Y.; Leynaud, O.; Barnes, P.; Férey, G., An Explanation for the Very Large Breathing Effect of a Metal–Organic Framework during CO2 Adsorption. *Advanced Materials* **2007,** *19* (17), 2246-2251.
23. Henke, S.; Schneemann, A.; Wutscher, A.; Fischer, R. A., Directing the breathing behavior of pillared-layered metal-organic frameworks via a systematic library of functionalized linkers bearing flexible substituents. *J Am Chem Soc* **2012,** *134* (22), 9464-74.
24. Pera-Titus, M.; Farrusseng, D., Guest-Induced Gate Opening and Breathing Phenomena in Soft Porous Crystals: Building Thermodynamically Consistent Isotherms. *J Phys Chem C* **2012,** *116* (2), 1638-1649.

25. Li, D.; Kaneko, K., Hydrogen bond-regulated microporous nature of copper complex-assembled microcrystals. *Chem Phys Lett* **2001,** *335* (1-2), 50-56.

26. Duong, D. D., *Adsorption Analysis : Equilibria and Kinetics*. Imperial College Press: London, 1998.

27. (a) Stone, D. Globe Continues Hottest Decades Ever. http://newswatch.nationalgeographic.com/2013/01/15/globe-continues-hottest-decade-ever/ (accessed October 14); (b) 6 Ways Climate Change Will Affect You. (accessed October 14).

28. Tans, P. Earth System Research Laboratory: Global Monitoring Division. www.esrl.noaa.gov/gmd/ccgg/trends/ (accessed January 12).

29. Wang, S.; Yan, S.; Ma, X.; Gong, J., Recent advances in capture of carbon dioxide using alkali-metal-based oxides. *Energy & Environmental Science* **2011,** *4* (10), 3805-3819.

30. McDonald, T. M.; Lee, W. R.; Mason, J. A.; Wiers, B. M.; Hong, C. S.; Long, J. R., Capture of Carbon Dioxide from Air and Flue Gas in the Alkylamine-Appended Metal–Organic Framework mmen-Mg2(dobpdc). *Journal of the American Chemical Society* **2012,** *134* (16), 7056-7065.

31. Lee, W. R.; Hwang, S. Y.; Ryu, D. W.; Lim, K. S.; Han, S. S.; Moon, D.; Choi, J.; Hong, C. S., Diamine-functionalized metal–organic framework: exceptionally high CO2 capacities from ambient air and flue gas, ultrafast CO2 uptake rate, and adsorption mechanism. *Energy & Environmental Science* **2014**.

32. McDonald, T. M.; D'Alessandro, D. M.; Krishna, R.; Long, J. R., Enhanced carbon dioxide capture upon incorporation of N,N[prime or minute]-dimethylethylenediamine in the metal-organic framework CuBTTri. *Chemical Science* **2011,** *2* (10), 2022-2028.

33. Planas, N.; Dzubak, A. L.; Poloni, R.; Lin, L. C.; McManus, A.; McDonald, T. M.; Neaton, J. B.; Long, J. R.; Smit, B.; Gagliardi, L., The mechanism of carbon dioxide adsorption in an alkylamine-functionalized metal-organic framework. *J Am Chem Soc* **2013,** *135* (20), 7402-5.

34. (a) Choi, S.; Drese, J. H.; Eisenberger, P. M.; Jones, C. W., Application of Amine-Tethered Solid Sorbents for Direct CO2 Capture from the Ambient Air. *Environmental Science & Technology* **2011,** *45* (6), 2420-2427; (b) Kuwahara, Y.; Kang, D.-Y.; Copeland, J. R.; Brunelli, N. A.; Didas, S. A.; Bollini, P.; Sievers, C.; Kamegawa, T.; Yamashita, H.; Jones, C. W., Dramatic Enhancement of CO2 Uptake by Poly(ethyleneimine) Using Zirconosilicate Supports. *Journal of the American Chemical Society* **2012,** *134* (26), 10757-10760.

35. Holy, P.; Sehnal, P.; Tichy, M.; Zavada, J.; Cisarova, I., Self-assembly of chiral hydrogen-bonded grid layers from terephthalic Siamese twins. *Tetrahedron-Asymmetr* **2003,** *14* (2), 245-253.

36. Jung, S. K.; Kang, S. G.; Suh, M. P., Template Synthesis and Properties of Square-Planar Nickel(II) and Copper(II) Complexes of 14-Membered Hexaaza Macrocyclic Ligands with Various Alkyl Pendant Arms at the Uncoordinated Nitrogens. *B Kor Chem Soc* **1989,** *10* (4), 362-366.

37. Kang, S.-G.; Ryu, K.; Jung, S.-K.; Kim, J., Template synthesis, crystal structure, and solution behavior of a hexaaza macrocyclic nickel(II) complex containing two N-aminoethyl pendant arms. *Inorganica Chimica Acta* **1999,** *293* (2), 140-146.

38. (a) Kondo, A.; Noguchi, H.; Carlucci, L.; Proserpio, D. M.; Ciani, G.; Kajiro, H.; Ohba, T.; Kanoh, H.; Kaneko, K., Double−Step Gas Sorption of a Two−Dimensional Metal−Organic Framework. *Journal of the American Chemical Society* **2007,** *129* (41), 12362-12363; (b) Zhang, J.; Wu, H.; Emge, T. J.; Li, J., A flexible MMOF exhibiting high selectivity for CO2 over N2, CH4 and other small gases. *Chemical Communications* **2010,** *46* (48), 9152-9154.

39. Moon, H. R.; Kim, J. H.; Suh, M. P., Redox-Active Porous Metal–Organic Framework Producing Silver Nanoparticles from AgI Ions at Room Temperature. *Angewandte Chemie International Edition* **2005,** *44* (8), 1261-1265.

40. Arvai, A. J.; Nielsen, C. ADSC Quantum-210 ADX Program; Area Detector System Corporation: Poway, CA, USA, 1983.

41. Fit2D program:Andy Hammersley (E-mail: hammersley@esrf.fr), ESRF; 6 RUE JULES HOROWITZBP 22038043 GRENOBLE CEDEX 9FRANCE

42. Otwinowski, Z.; Minor, W.; Carter Jr, C. W.; Sweet (Eds.), R. M. Methods in Enzymology 276 Part A; Academic Press: New York, 1997; 307-326.

43. Sheldrick, G. M.; SHELXTL-PLUS: Crystal Structure Analysis Package; Bruker Analytical X-Ray: Madison, WI, USA, 1997.

44. van der Sluis, P.; Speck, *A. L. Acta Crystallogr. Sect. A: Found. Crystallogr.* **1990**, 194-201.